CENTER FOR RESEARCH IN ADVANCED MATERIALS (CIMAV)

DEPARTMENT OF POSTGRADUATE STUDIES

Synthesis of Ferroelectric and Multiferroics Thin films of $BiMnO_3$/ $SrTiO_3$ and Structural, Piezoelectric, Magnetic, Optical, and Mechanical Properties Characterization

A Dissertation

In Partial Fulfillment of the Requirements for the degree of

DOCTOR OF PHILOSOPHY IN MATERIAL SCIENCE

BY

Glory Valentine Umoh

ADVISOR:

Dr. Abel Hurtado Macías

Co-Advisor

Dr. Sión Federico Olive Méndez

CHIHUAHUA, CHIH. **DECEMBER 2022**

TABLE OF CONTENTS

LIST OF FIGURES

LIST OF TABLES

ACKNOWLEDGMENTS

To all those who with their teachings, mentoring, wisdom, companionship, understanding, affection, respect, appreciation, support, knowledge, and patience, contributed to making this work possible, I am honored and blessed to have you all.

To my Advisor, Dr. Abel Hurtado-Macías, he is an outstanding teacher, scientist, researcher, mentor, and father. He guides and inspires me to always think outside the box, this makes me become an independent researcher. His support, knowledge, wisdom, and patience helped me to accomplish this research.

To Dr. Sion F. Olive Méndez, who is my Co-Advisor. His insight, and knowledge into the subject matter steered me through this research. He gave me the confidence to work in his laboratory without even knowing me, and with the great support and help of Mr. José Trinidad Holguín Momaca this work became a success.

To Dr. Guillermo Manuel Herrera Pérez, who has always been supporting, and providing advice regarding my analysis.

To Dr. Francisco Espinosa Magaña, for his knowledge and support for the work.

To Dr. Carlos Ornelas, Dr. Cesar Cutberto Leyva Porras, Mr. Roberto Pablo Talamantes Soto, Ms. Karla Campos who with their support in the characterizations this work was accomplished.

I would also like to give special thanks to CONACYT, for the scholarship granted to me, which makes it possible to carry out my doctoral studies.

I am extremely grateful to our team, Mr. Jesús Eduardo Leal, Ms. Imelda Janette Jarquín Rodríguez, Mr. Gerardo Resendiz, and my Nigerian friends for their support in my academic endeavor.

I especially thank my father, Mr. Valentine Linus Umoh. mother, Mrs Mammy Valentine Umoh (JP) and siblings. Their teachings, encouragement, motivation, and prayers help me to get to where I am today.

Finally, with a thankful heart to God who knows the end from the beginning. I have experienced His love, care, guidance, and hand in the success of my academic pursuit. I will continue to trust Him for the greater things that the future holds.

"In research, I find clarity and learn something new" Glory Valentine Umoh.

ABSTRACT

Multiferroic characteristics of $BiMnO_3$ thin films offer great prospects to explore, either in terms of ferroelectricity, ferromagnetism, or ferroelasticity. Ferroelectric and ferromagnetic materials can be used in data storage due to their electrical and magnetic properties. Ferroelastic can find its application in microelectromechanical systems devices. This dissertation focused on the synthesis, characterization, and improvement of the multiferroic properties of polycrystalline $BiMnO_3$ thin films as well as the elaboration influence of Cu on the magnetism of $BiMnO_3$ thin films. $BiMnO_3$ films were grown on three different substrates, Si (001), Pt-buffered Si (001), Nb-doped $SrTiO_3$ (100), and also doped with different amounts of Cu. The films were characterized using techniques such as X-Ray diffraction (XRD), scanning electron microscope (SEM), HRTEM observations, by energy-dispersive X-ray spectroscopy (EDS), atomic force microscopy (AFM), X-ray photoelectron spectroscopy (XPS), Raman spectroscopy, Visible-near-IR spectroscopy (Vis-NIR), electron energy loss spectrometer (EELS), nanoindenter, superconductor quantum interference device (SQUID) magnetometer, and finally, the polarization-electric field (P-E) hysteresis loops of the $BiMnO_3$ thin films were conducted at 200 and 300 K. There are several studies on the growth of thin films, however, they are not clear and in some cases contradictory, therefore, different parameters were controlled during the deposition in terms of working pressure, RF power, substrate, deposition

temperature, and target to substrate distance. After deposition ex-situ thermal treatment was carried out in order to compensate for the volatility of bismuth and also to eliminate secondary phase.

Kramer's–Krönig analysis was used to determine bandgap, via a polynomial fit in the energy loss function (ELF) plot with an Eg = 1.63 eV, complex dielectric function, and static dielectric constant, ε* = 4.68 of the grown $BiMnO_3$ thin films. The reflection coefficient Ґl of the $BiMnO_3$ thin films was used to elucidate the reflection loss in the $BiMnO_3$ thin films. XPS analysis revealed the existence of Mn charge transition of 3+ and 4+ states. Resistivity result describes $BIMnO_3$ as a semiconductor. The nanomechanical characterization demonstrated that the region of penetration depth was below 10% of $BiMnO_3$ film thickness. Young's modulus (E), hardness (H), and Stiffness (S) were measured to be 142 ± 3 GPa, 8 ± 0.2 GPa, and 44072 ± 45 N/m respectively. Using the experimental mechanical properties, a finite element analysis was carried out to understand the relationship between the irreversible work vs. depth curve and plastic-deformation evolution of the thin film-interface-substrate system, associated with th pop-in observed. The ferroelastic range for the $BiMnO_3$ material was observed between 0 to 12 nm, and the yield strength was found to be Y=2.6 ± 0.7 GPa. Using a finite element, the Von Mises stress distribution of the $BiMnO_3$ thin film was determined. Magnetic measurements showed a ferromagnetic behavior with Curie temperature of 37 K and strong short-range magnetic interactions. The Ferroelectric properties of $BiMnO_3$

was found to improve at 200 K. Finally, understanding the effect of doping Cu on $BiMnO_3$ on the electronic and magnetic properties, demonstrates that Cu-dopant and Mn atoms couple antiferromagnetically, causing a reduced magnetic moment, in agreement with the experimental measurements of magnetic hysteresis loops. Studies in this research project reveal $BiMnO_3$ as an excellent candidate for electronic applications, such as in energy harvesting, spintronics, spin valve, sensor, microelectromechanical systems devices, and even in the recent field of spintronics and has unfold a new window for studying the optical properties of $BiMnO_3$ multiferroic materials through VEELS-TEM analysis.

1. INTRODUCTION

At present, several key technologies require materials that exhibit simultaneously or individually ferroelectricity (FE), ferromagnetism (FM), and/or ferroelasticity in the same phase. This has driven the development of multifunctional materials that meet the needs of these electronic components. These devices must have relevant characteristics that allow them to improve their performance in different conditions and applications, such as nonvolatile multistate memory (NMSM), spintronics, sensors, energy harvesters, and [1][2][3]. The electronics industry seeks to develop devices that allow the storage and movement of considerable amounts of electronic information. To achieve this they have invested money, time, and effort; Unfortunately, there are few materials that have these properties and are relatively expensive.

In view of the demand to propose new devices for nonvolatile multistate memory, as well as to replace the current ones. Investigation of multiferroic materials has been developed,

especially, with materials that have a perovskite-like structure, These materials possess the coexistence of magnetic and ferroelectric order, called multiferroics, and display magnetoelectric cross-coupling phenomena [2,4].

Ferroelectric materials have the quality of having a spontaneous polarization, which can be activated at any time by an electric field. Antiferroelectric materials, on the other hand, are those that possess ordered dipole moments that cancel each other out within the unit cell.

Ferroelectric materials are dielectric or insulating materials, possessing spontaneous polarization (P) that can be reoriented by an applied electric field (E). Ferromagnetic (FM) materials, on the other hand, have a stable spontaneous magnetization and can be activated at any time by an electric field [5][6]. At Curie point or Curie temperature, a ferromagnetic material starts behaving as a paramagnetic substance, in $BiMnO_3$ is ferromagnetic with Curie temperature (T_C) of 105 K and FE ~400 K [7,8]. Thus, it has a simultaneous spontaneous magnetization and polarization that can be switched by external magnetic and electric fields.

In materials with magnetoelectric coupling, the ferroelectric polarization can be controlled by applying a variable magnetic field and vice versa for the magnetic one. The construction of a single-phase magnetoelectric material is challenging, due to these conditions: magnetism requires d electrons, ferroelectric distortion is suppressed by d electrons. Also, the material must crystallize in a noncentrosymmetric space group.

Similarly, magnetoelectric materials are mostly synthesized and studied in bulk, but thin films are gaining more interest as their properties increase compared to bulk materials.

1.1 Overview of the Perovskite Structure

There are a great number of ceramic materials, but some are in a more developed state than others. Among these are those based on mixed oxides, like the ternary oxides: $BiMnO_3$, $SrTiO_3$, $BaTiO_3$, and $BiFeO_3$. The chemical formula for the most stable phase of perovskite is ABO_3.

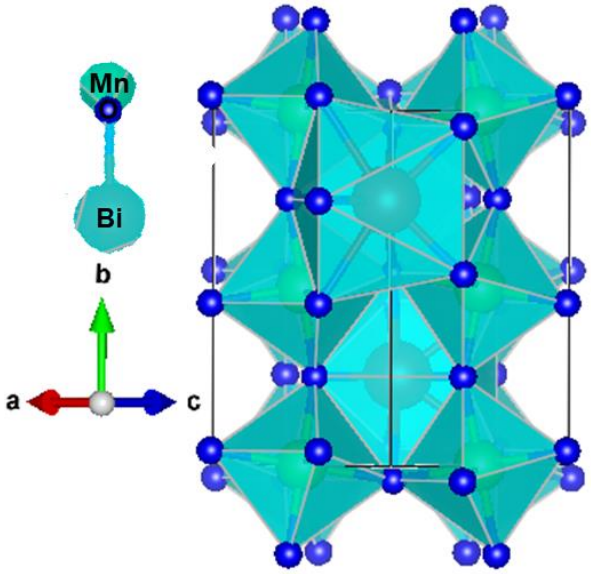

Figure. 1.1. (a) Schematic of the crystal structure of $BiMnO_3$.

The A-site cation is located at the body center of the cube, and the B cation is located at each of the eight corners, and the O anion is at each of the centers of the 12 edges.

as shown in Figure 1.1 (a); the 'A' atoms are generally larger than the 'B' atoms and occupies a 12-fold coordination site, while the B-site cation occupies a 6-fold coordination site. B cation is usually a transition metal of 4+, 3+, and 2+ valence and clusters at the center of a coordinating octahedron six (neighboring oxygens). This octahedron is connected to another octahedron formed by the cation A of the cubic structure. Where cation A has a valence of 2+ or 3+ to balance the charge of the structure, entering the cuboctahedral site, hence forming the basic structure of the perovskite structure.

The crystal structure of $BiMnO_3$ is known to depend on its oxygen stoichiometry [7,9–13], due to structural modifications arising from the peculiar $6s^2$ electrons and its four interacting mechanisms (i.e. electric polarity, octahedral tilts, magnetism, and co-operative Jahn–Teller distortion) associated with Mn^{3+} cations.[14]. Furthermore, the Bi-6*s* lone pair is predictable to result in FE. Powder diffraction has indicated that monoclinic BMO with space group *C*2 is non-centrosymmetric and possesses both FE and FM behaviors [13–16]. Belik *et al.* [17]suggested, based on detailed experimental work, that BMO has four different crystalline structures with space groups, namely: monoclinic I: *C*2/*c*, monoclinic II: *C*2, monoclinic $P2_1/c$ and orthorhombic: *Pnma* [16,18]. The structural change results from oxygen non-stoichiometry, and occurs at different transition temperatures [13,16,19]. However, the existence of FE in this system has raised doubt and questions by some reasonable analysis of electron and neutron diffraction data showing that polycrystalline BMO is relatively centrosymmetric monoclinic structure, therefore incompatible with proper FE [19,20]. The growth of a stabilized single BMO phase in bulk or in thin films suffer the high volatility of bismuth at high growth temperatures [14,21–24] Occurrence of Mn^{3+} and Mn^{4+} valence attracts attention due to their high electric permittivity and the possibility of double exchange interactions as the origin of FM. [25]. Meanwhile, the ferromagnetic ordering in well stoichiometric $BiMnO_3$ is originated by superexchange interactions of the Mn^{3+} ($3d^4$) ions [23,26,27].

1.11 Multiferroic materials and magnetoelectric coupling

Generally, Multiferroics are defined as those materials with one or more ferroic order, and magnetoelectricity refers to the mutual coupling between spins and/or magnetic field (magnetism) and electric dipoles and/or electric field (electricity). [28] Few multiferroic materials have been identified; and in those that are known, the mechanism behind their

ferroelectricity is always affected by their magnetism. Conventional, the mechanism behind the magnetoelectric effect occurs as a result of magnetization and polarization in multiferroic materials, introduced by means of an electric or magnetic field, respectively [29]. It has been shown that a magnetic order can create superconductivity, it has also been shown that a magnetic order can create (weak) ferroelectricity and vice versa. This field of research, say multiferrocity and magnetoelectricity, is shown in Figure 1.2 [30], the Figure shows the location of multiferroic materials within a small overlapping zone of magnetic materials and ferroelectric materials respectively. The hysteresis of the ferromagnet in a magnetic field is showed in blue, while that of ferroelectrics is in yellow, then the resultant of their coupling is display in green.

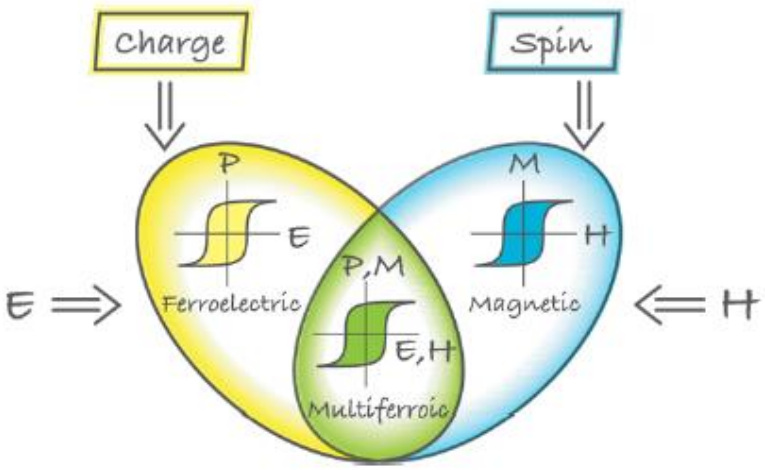

Figure 1.2. Relationship between multiferroic and magnetoelectric materials [30].

The Possible cross-couplings in that can exist in Figure 1.2 are electric polarization,

electric field, applied mechanical stress, strain, magnetic field, and magnetization.

The intersection in Figure 1.2 (green region) represents materials that are multiferroic. The coupling between parameters of corresponding order opens interesting perspectives for the design of applications in the field of microelectronics and spintronics.

1.12 Ferroelectricity in Perovskite-type materials

Ferroelectric Perovskite-type materials exhibited properties such as ferroelectric, dielectric, piezoelectric and pyroelectric effect, this makes these materials useful in a wide area of application, including nonvolatile memories, sensors, actuator and transducer. The main characteristic of perovskites is that they exhibit a wide variety of structural phase transitions. Generally, these compounds have the chemical formula ABO3, where A is a divalent or monovalent cation and B is a transition metal cation [31]. Although its structure at high temperatures shows a wide variety of structural instabilities, which can present rotation and distortions of the octahedral oxygen as well as a displacement of the ions from their defined crystallographic sites. The different types of crystal symmetries manifested in this material and the types of phase transition behaviour depend on the individual compound.

Ferroelectric material exhibits spontaneous electrical polarization that is reversible by an applied electric field. Ferroelectricity was discovered in 1920, which is also called Seignette or Rochelle electricity [32], Rochelle salt was the first material to be found with ferroelectric properties in 1921 [33]. Similarly, magnetoelectric materials were discovered more than a century ago by Pierre Curie, which have been gaining popularity since the 1960s and the effect was first postulated in 1894.

The concept of electrical polarization is vital for the understanding of ferroelectricity. Usually, Ferroelectric process is associated with an electrical hysteresis. A change in

polarization orientation is accompanied by a change in the hysteresis loop. The induced microscopic polarization can be reduced to zero by the presence of domains, which are regions of opposite polarization within the sample. The electrical polarization tends to change as a function of temperature. In this case, if the temperature increases, the polarization decreases, with a phase transition to an unpolarized state, which generally occurs at high temperatures. Additionally, the hysteresis that causes spontaneous polarization in the absence of an applied field leads to storage applications in which the direction of the electrical polarization represents the "0" or "1" of the data bit.

For a material to have spontaneous electrical polarization, it must have a non-centrosymmetric structure of the constituent ions and electrons. For a material to be classified as ferroelectric, it is necessary that the electrical polarization be interchangeable, and a non-reconstructive transition between two stable states of opposite polarization and must be accessible to known experimental fields.

Jahn-Teller (JT) effect can be define to be a symmetry-lowering of the geometrical distortion be it a nonlinear molecule or a crystal as a result of the presence of a degenerate electronic state [34]. JT distortion is nonpolar in nature, it usually results in two different types of ferroelectric distortions namely: original JT effect and pseudo-JT effect (or second-order JT effect) which is the stabilization of the bonding field of the perovskite B-site transition metal cation by surrounding anions, as occurs with Ti in the BaTiO3 structure and is responsible for the ferroelectricity in some ferroelectrics such as $BaTiO_3$ [35][34].

1.13 Ferromagnetism in Perovskite type materials

The magnetism in ferromagnetic materials is caused by a spontaneous magnetization of

certain material that is stable and can be changed by the application of a magnetic field [36]. The magnetic response of a material comes from the atoms or ions that make up its composition. The magnetic moment of an atom or ion comes from three main sources:

- A change in orbital momentum induced by an electric field
- The spin of the electrons
- The orbital angular momentum of the electron around the nucleus

The first provides a diamagnetic contribution, while the last two effect give paramagnetic contributions to the magnetization.

In a crystal, the magnetic properties depend on two factors:

- The interaction between these magnetic moments
- The magnetic response associated with each atom or ion

In the case of no unpaired electrons around each atom or ion, there will be no net magnetic moment associated with them, thus the material will exhibit diamagnetic behavior. When there are unpaired electrons, each atom or ion has a net magnetic moment. Depending on the interactions between the magnetic dipoles, the material can show ferromagnetic (FM), paramagnetic (PM), ferrimagnetic (FIM) and antiferromagnetic (AFM) behavior [37]. In a paramagnetic material, alignment of moments is not observed due to thermal fluctuations. In ferromagnetic material the adjacent dipole moments are aligned parallel. In an antiferromagnetic, the dipole moments are likewise aligned antiparallel. In a ferrimagnetic material, the moments are aligned antiparallel but with different magnitude. Ferromagnetism has a stronger magnetic response compared to paramagnetism and diamagnetism. It is characterized by a transition temperature, called the Curie temperature (Tc). In the case of bismuth manganese oxide, this is the Neel temperature (TN). Above this temperature, the material becomes paramagnetic. Below this temperature, it is

ferromagnetic and is characterized by a hysteresis-like response when an external magnetic field is applied.

In perovskite-type oxides, direct spin-spin interactions do not exist. In this case, the interactions are mediated by the so-called “superexchange” mechanism. Essentially, the spin moments of the Mn^{3+} ion on the opposite side of the O^{2-} ions interact with each other via the p-type orbital electrons of oxygen.

1.14 Optical Properties and Band Gap

Semiconductor material $BiMnO_3$ has a small band gap, of around (1.1 ~ 1.63 eV), [24,38–40] while most of the other ABO_3 perovskites, such as $BiFeO_3$, and $BaTiO_3$ has been evidence of having a large band gap [41,42]. However, $BiMnO_3$ has demonstrated a strong photovoltaic effect and larger electro-optic coefficients than any ferroelectric materials, and thus gained great interests for its potential applications photovoltaic (PV) EMI shielding, plasmonic and photonics applications. [43,44].

1.15 Methods of obtaining $BiMnO_3$

There are several methods of obtaining bismuth manganese oxide, such as rf magnetron sputtering, sol-gel

Method, solid-state reaction methods, mechanochemical synthesis and co-precipitation method etc. The results of these techniques usually presents either one or two of these problems: (a) extensive leakage of current in both bulk and in thin films, and (b) low Curie temperature and magnetic moments for bulk and in thin films.

(a) One of the main obstacles in the application of $BiMnO_3$ is the large leakage current due to the existence of secondary phases and oxygen content of Bi_2O_3 [2]. Attempts have

been made to obtain $BiMnO_3$ at the bulk level in the pure phase, for which various synthesis techniques have been used. Currently rf magnetron sputtering methods have received special attention. The variety of methods for obtaining $BiMnO_3$ films is quite versatile, as there are methods that include the dissolution of the reagents and subsequently the application of this solution on the substrate. There are methods that include making a target, pulsed laser deposition (PLD), chemical vapour deposition (CVD), plasma enhanced chemical vapor deposition (PECVD) and Radio frequency (RF) and then eroding it to form the thin film. There are a wide variety of methodologies used in the synthesis of bismuth manganese, among which are chemical methods and physical methods. Both have been used in almost equal numbers, however the method chosen will depend on the initial reagents. The advantage of chemical methods is that they manage to obtain nanometric particle sizes and have better control over the morphology of the particle, as well as the use of low crystallization temperatures. In the part of thin films there are several techniques that are available, however the radio frequency deposition technique is a technique that is accessible to a certain degree and with optimal results in the growth of thin films of $BiMnO_3$.

(b) Low Curie temperature is also common for bulk and thin films $BiMnO_3$. Ferromagnetism has a very strong magnetic response compared with paramagnetic and diamagnetic behavior as shown in Figure 1.3. Curie temperature, (Tc) is characterized by a transition temperature, which above this temperature, the material is paramagnetic and below this temperature, it is ferromagnetic. $BiMnO_3$ has a TC = (50 ~ 105 K) [45][46], which is likely to prevent it from working properly when used in some devices.

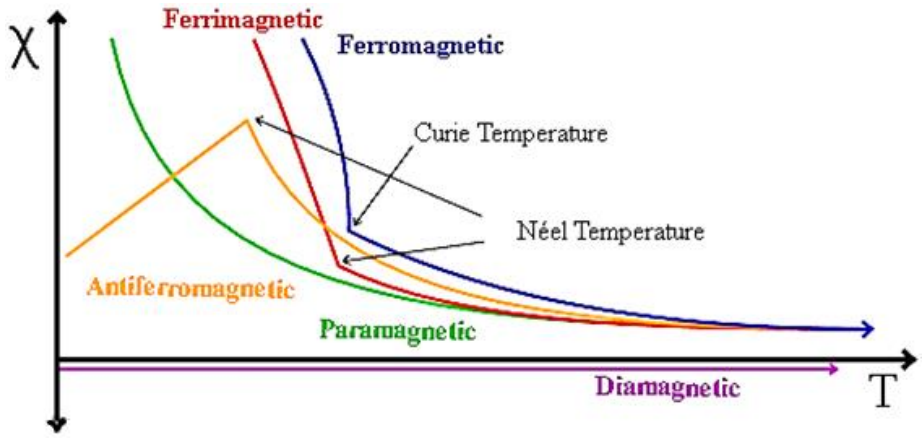

Figure 1.3. Graph of magnetic susceptibility versus temperature for different types of Magnets

1.2 Justification

The interest in bismuth manganese arises due to the successful growth of $BiMnO_3$ films. Ferroelectricity and magnetism require completely different criteria to obtained from a material, this brings about the scarcity of multiferroics. $BiMnO_3$ is one of the few materials that exhibits coexist coupling of ferroelectric and magnetic orders at the same time at room temperature as demonstrated by C.Q. Jin *at. al* at Beijing national lab for condensed matter physics China [47]. The growth of single-phase $BiMnO_3$ films is not entirely easy. Bismuth manganese films generally present secondary phases, such as bismuth oxide (Bi_2O_3), trimanganese tetraoxide (Mn_3O_4), and bismuth oxycarbonate ($Bi_{12}MnO_{20}$) [2,21] and/or non-stoichiometric phases, such as $BiMnO_{2.94}$, $Bi_3Mn_2O_7$[48]. The synthesis conditions affect the formation of these phases, forming heterogeneous films and as such different phases may contribute to either or both ferroelectric and ferromagnetic signals and may dramatically decrease or increase the ferroelectric and ferromagnetic properties obtained.

In the research work, development of thin films of both pure and Cu-doped $BiMnO_3$ in this work had its starting point from the information found in the literature about $BiMnO_3$.

In the growth of thin films of $BiMnO_3$, after the deposition process using RF Magnetron sputtering, A selected number of the thin films was subjected to an *ex-situ* thermal treatment due to the volatility nature of Bi, this was done with the purpose of studying the morphology and trying to optimize the quality of the thin films. it was found that the Monoclinic structure of the $BiMnO_3$ has ferroelectric and ferromagnetic properties at room temperature. While the Cu doped-$BiMnO_3$ resulted in Cu coupling antiferromagnetically with Mn, and at a certain concentration effectively decreases the net magnetic moment.

1.3 HYPOTHESES

The *ex-situ* thermal treatment for $BiMnO_3$ thin film given in our results eliminated Bi_2O_3 secondary phase, found on the as-grown $BiMnO_3$ film. Phase change was observed which resulted in an improved physical property of the film.

1.4 OBJECTIVES

1.41 General Objective

- Synthesize thin films of $BiMnO_3$/ $SrTiO_3$, using radio frequency magnetron sputtering technique, as well as the elaboration of its structural characterization, chemical composition, nanomechanical, magnetoelectric, optical and piezoelectric behaviour.

1.42 Specific objectives

- Deposition of thin film of $BiMnO_3/SrTiO_3$ multiferroics material by radio frequency magnetron sputtering to observe the feasibility of obtaining a pure phase of bismuth manganese.

- Structural characterization and chemical composition of the $BiMnO_3/SrTiO_3$ by means of Grazing or Glancing Incidence XRD (GIXD)

- Study the morphology, thickness, and mapping EDS composition in the thin film of $BiMnO_3$/ $SrTiO_3$ by scanning electron microscopy (SEM).

- Characterization of the interface of $BiMnO_3/SrTiO_3$ thin film by High-resolution transmission electron microscopy (HRTEM) and nanobeam diffraction patterns in TEM

- Determine the physical properties of ferroelectric and magnetic measurements.

- Perform Optical measurements by means of Valence Electron Energy Loss Spectrometry (VEELS) analysis.

- Evaluate the mechanical properties, such as: elastic modulus, stiffness, hardness and fracture toughness of the thin film of $BiMnO_3$/ $SrTiO_3$ using continuous stiffness measurement (CSM) method by nanoindentation.

2. RESEARCH METHODOLOGY

2.1 Radio frequency magnetron sputter deposition

Radio frequency (RF)-magnetron sputtering refers to a high-rate vacuum coating of thin film deposition methods that involve Argon ions accelerated by a RF electric field to hit a target made of the material to sputter onto a wide range of materials with thicknesses up to millimeter. The target is sputtered in all directions, sputtered atoms will reach the substrate placed in front of the target, but outside of the plasma, to prevent etching by the plasma.

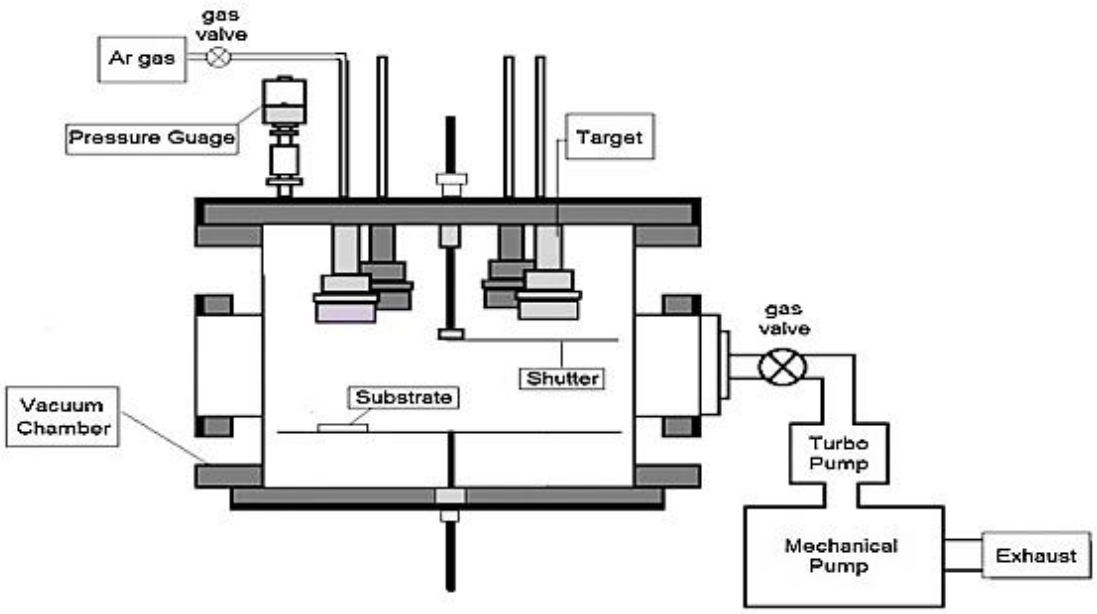

Figure 2.1. Schematic of RF magnetron sputtering [49].

RF sputtering is commonly used for electrically non-conductive target materials deposition. It runs an energetic wave through an inert gas in the vacuum chamber which becomes ionized. The cathode or the target material which is to become the thin film is bombarded by these high energy ions sputtering off atoms as a fine spray covering the substrate. The recommended frequency normally used in this method is 13.56 MHz with a bandwidth of 14 kHz to avoid expense of electromagnetic shielding. [50]. RF magnetron sputtering has been reported to be other efficient methods to synthesize uniform, stable, stoichiometric, and highly crystalline films. It also favours high-deposition rates; ease of sputtering any metal, alloy or compound and formation of high-purity films. [49,51,52]. RF magnetron sputtering has advantages, not only for deposition of insulators but also conducting materials, ionic, covalent compounds, and polymer. The drawback for RF magnetron sputtering equipment, could be the low deposition rate and is also very complex and more expensive [53]. Figure. 2.1 shows the schematic of RF sputtering system.

It consists of a cylindrical magnetron sputtering plasma reactor operated at a frequency of 13.56 MHz. The vacuum chamber must be high to create a low-pressure environment for sputtering. The gas that comprises the plasma, are typically of argon gas, which enters the chamber first. The distance between substrate holder and the target is adjustable between 3 and 15 mm. The dense plasma which interacts strongly with the substrate causes an intense ion bombardment of the growing layer. During the RF discharge, the positive ions are accelerated and bombard the substrate with high energies, which are dependent on the discharge excitation frequency. The following parameters can be used to control the film quality such as: such as the argon pressure, substrate temperature, RF sputtering power, and oxygen partial

Some RF magnetron sputtering systems are equipped with Reflection High Energy Electron Diffraction (RHEED) for monitoring of the growth process and the film quality. It makes use of an electron gun to send high-energy electrons at a grazing incidence to the substrate. A very high vacuum is needed for its operation and can gather the real time lattice information, which is a useful apparatus for the in-depth studies of the film growth structures.

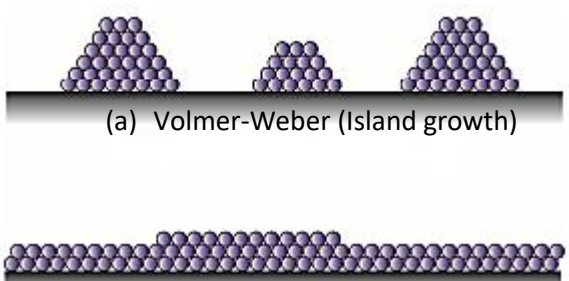

(a) Volmer-Weber (Island growth)

Figure 2.2. Basic growth modes of thin films [54].

The modes of film growth and nucleation of thin films on substrate surface can be summarised into three primary modes including (a) Volmer-Weber (island growth), (b) Frank-van der Merwe (layer-by-layer growth), and (c) Stranski-Krastanov (combination of Island and layer growth). Each mode is illustrated in Figure. 2.2. In island growth, the interaction of the adsorbed atoms is much stronger among them than with the substrate surface, which leads to the formation of three-dimensional islands or clusters. The layer-by-layer growth which is also referred to as bi-dimensional growth, the atoms adsorbed on the surface have a stronger interaction with the surface, leading to the formation of a complete monolayer (ML) before another begins to grow. The mixed growth is characterized by the island and layer growth. In this mode, the adsorbed atoms grow layer-by-layer till the critical layer thickness is reached, which depends on the properties of thin films and substrates. Each mode of growth is important because it has a particular application.

2.2 Structural characterization

2.2.1 X-Ray diffraction

X-ray diffraction (XRD) is a non-destructive technique which provides insights to investigate the crystalline structures of materials. X-rays was discovered by William Conrad Röntgen in 1895, this paved a way for important innovations in all scientific disciplines. X-ray diffraction (XRD) by crystals was initiated by Laue, Friedrich, and Knipping in 1912, this allowed new possibilities in the study of crystalline materials (Friedrich et al., 1913) [55,56]. It provides information on the identification of the preferred crystal orientation (texture), crystallite size, phases, and other structural parameters in thin film materials. X-ray diffraction peaks are produced by constructive interference of a monochromatic beam of X-rays scattered at specific angles from each set of lattice planes in a sample. The diffraction, or Bragg diffraction, occurs due to the constructive interference between the reflected X-rays from adjacent crystal planes. The main idea of X-ray diffraction is Bragg's Law as

$$n\lambda = 2d\sin\theta \quad (1)$$

where n is an integer, λ is the wavelength of coherent incident X-rays, the variable d is the distance between atomic layers in a crystal and θ is the incident angle. Figure. 2.3 is a schematic description of Bragg's Law

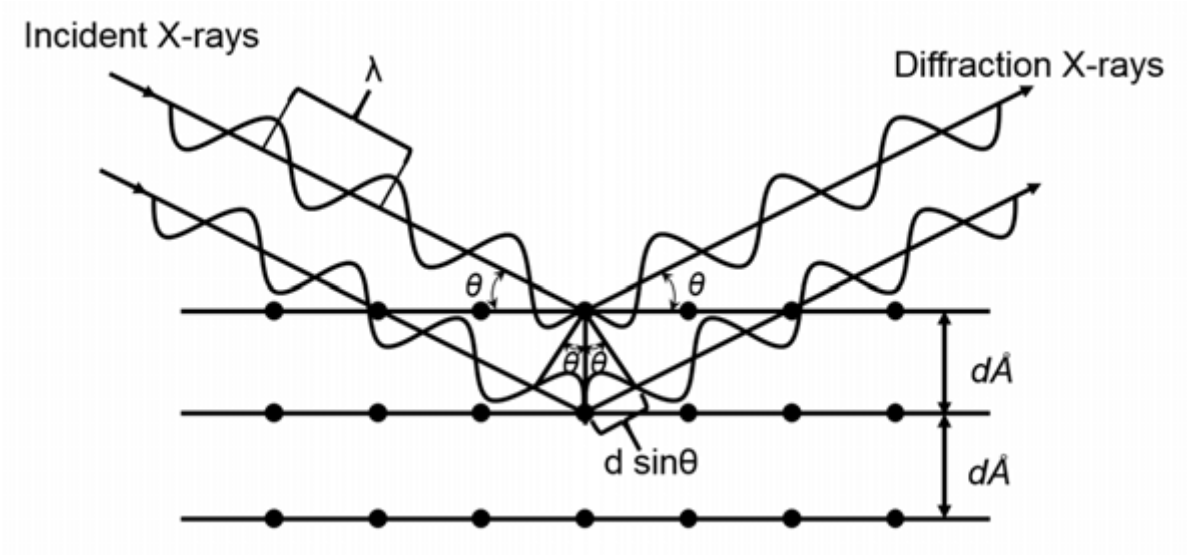

Figure 2.3. Schematic description of Bragg's Law [57].

2.2.2. High-resolution transmission electron microscopy

High-resolution TEM (HRTEM) is an excellent mode of imaging in TEM that uses both transmitted and diffracted electron beams to create an interference image. In 1970s (Smith, 1997) [58], first recorded the phase contrast of modulated electron waves passing through the sample down to the angstrom level. It is a powerful tool for characterization of real-space images of the local structure of thin specimens, which provide structural information at better than 0.2 nm spatial resolution. It was developed to overcome the limited resolution of optical microscopy. HRTEM characterization on thin films offers information on distribution and atomic structure, defects, interfaces and grain boundaries, thermodynamic decomposition, lattice spacing, crystal symmetry, dislocations, diffusion, and phase transformations, nano-crystalline features in amorphous films, sub-micron morphology, device features, and small particle analysis in heterogeneous catalysts. This mode requires sample to be <10nm thick. Shown in Figure. 2.4 is a schematic view of HRTEM.

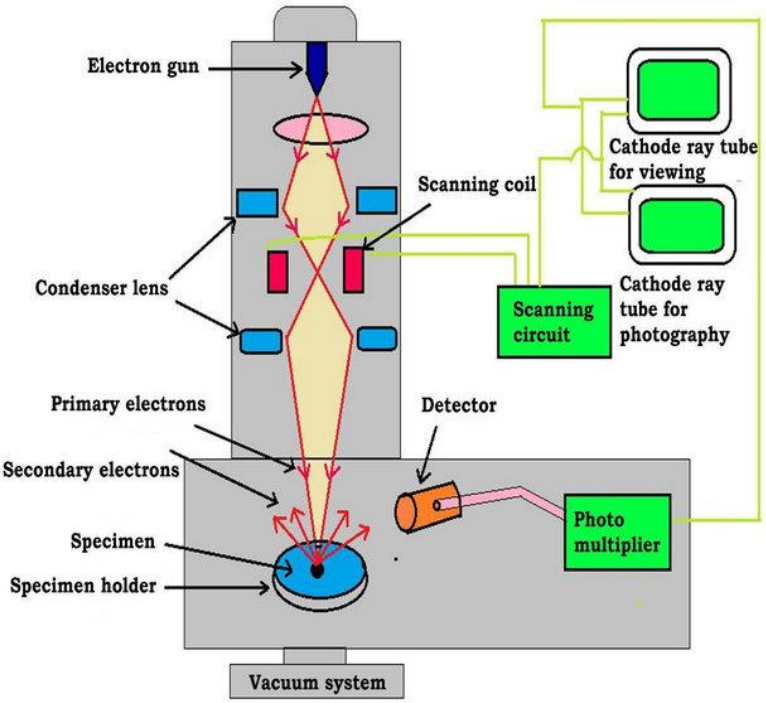

Figure 2.4. Schematic ray diagram of HRTEM [59].

The spatial resolution or resolving power limit of the microscope is theoretically based on the Rayleigh criterion, which states that, two images are just resolvable when the centre of the diffraction pattern of one is directly over the first minimum of the diffraction pattern of the other.

The Rayleigh criterion defines the resolution of light microscope as:

$$R = \frac{0.612\lambda}{\mu \sin\alpha} \qquad (2)$$

where λ is the wavelength of light, μ is the refractive index of the view medium (n =1 for vacuum), and α is the semi-angle of collection of the magnifying lens. The variable of refractive index and semi-angle is small, thus the resolution of light microscope is mainly decided by the wavelength of the radiation source. Taking green light as an example, its 550nm wavelength gives 300nm resolution, which is not high enough to separate two

nearby atoms in solid-state materials. The distance between two atoms in solid is around 0.2nm.

The HRTEM can operate in Bright-Field, Dark-Field, High resolution, SAED and CBED modes, the diffraction mode and the imaging mode is shown in Figure. 2.5 diagrams. Each mode can be controlled by changing the focal length of the intermediate lens. In the diffraction mode, the beam is refocused on the back focal plane of objective lens. The diffraction pattern is projected on the view screen with the selected area diffraction (SAD) aperture inserted. While in the imaging mode, the image plane coincides with the image plane of objective lens.

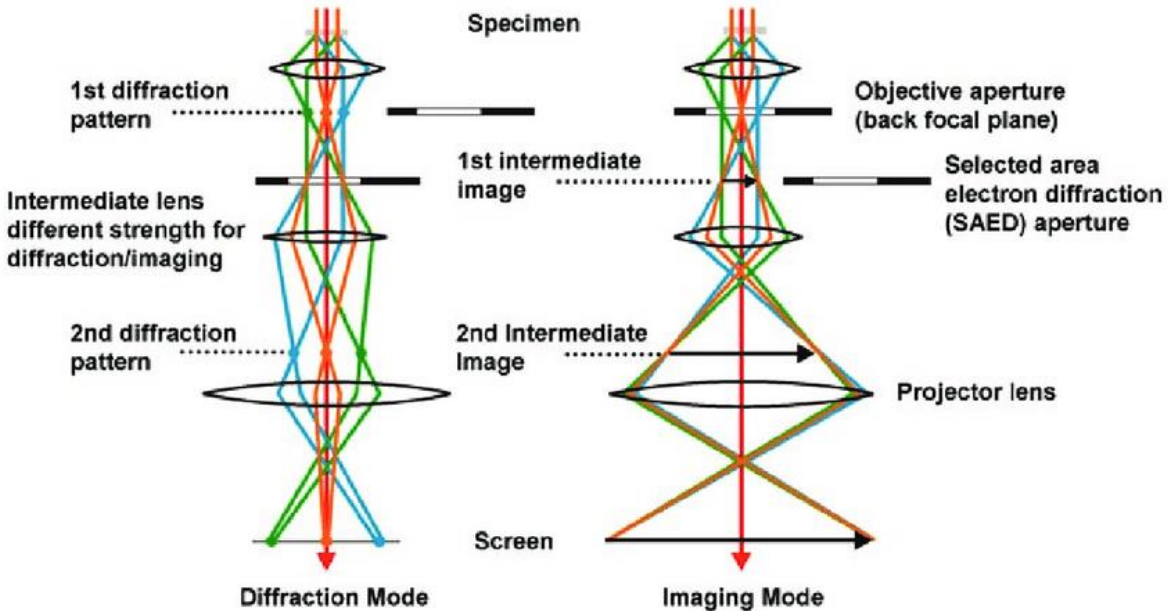

Figure 2.5. Image and Diffraction pattern formation in HRTEM a) Diffraction mode b) Image mode [60].

Another valuable imaging mode is transmission electron microscopy (TEM), it has the ability to investigate the internal structure below the surface as the electron beam

transmits an ultra-thin sample (~ 100nm). TEM provides projection of microstructure in atomic level. It utilizes energetic electrons to provide morphologic, compositional, and crystallographic information on samples. Scanning transmission electron microscopy (STEM), where a focused beam is scanned over the sample in a raster illumination system. It makes other analytical techniques possible, such as annular dark-field imaging and Z-contrast (Z, atomic number), energy dispersive X-ray spectroscopy (EDS), and electron energy loss spectroscopy (EELS). These signals allow direct correlation of images and spectroscopic data.

2.2.3. Scanning electron microscopy

Scanning electron microscopy (SEM) consists in an electron source, electromagnetic lens, and an electron detector. It uses a focused beam of high energy electrons as the illumination source. The components and layout of SEM is likely to that of TEM; however, it has a different working principle. Rather than utilizing the transmitted electrons, SEM detects scattered electrons emitted from the surface of the sample formed by the interaction between electron beam and sample surface. Therefore, SEM could provide the information of the morphology, topography, composition, orientation of grains, crystallographic information of the sample. In addition, the accelerated voltage for SEM ranges from 10 to 40 kV while for TEM is >100 kV. The resolution of SEM can reach 0.4 nm, which is lower than that of TEM. Thickness of the specimen is not important in SEM, while specimen thickness is very important in TEM. SEM requires a very easy preparation technique, while TEM needs skill to prepare a very thin sample. Figure. 2.5 shows the schematic of the components in a SEM. Unlike the TEM, the objective lens and associated apertures are situated before the sample.

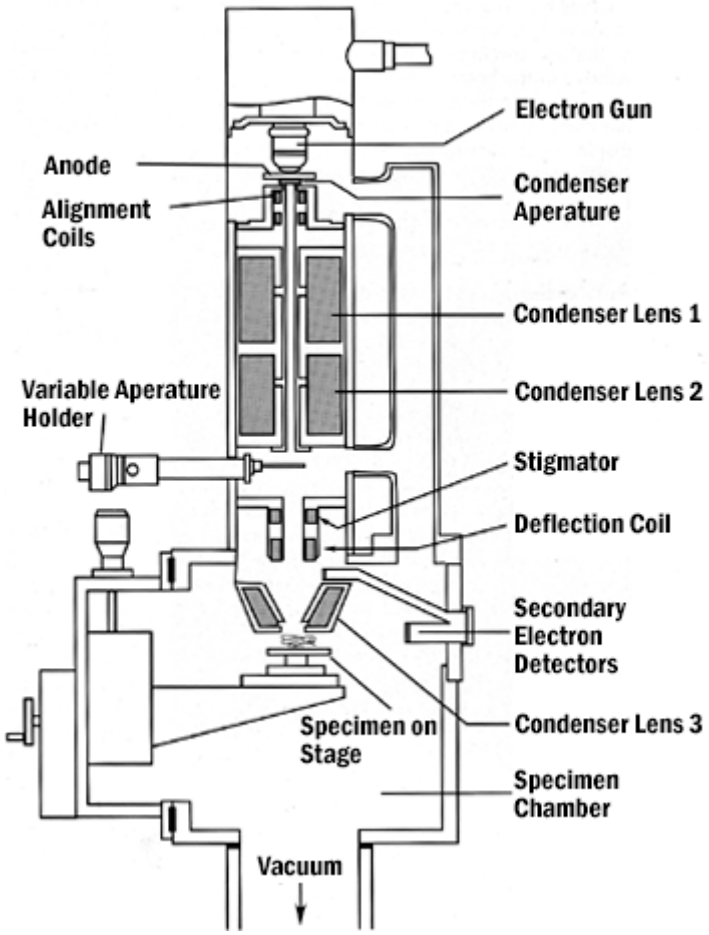

Figure 2.6. Schematic showing the major components of scanning electron microscope [61].

Scanning Electron Microscope use a focused beam of electrons to image the specimen and gain information as to its structure and composition. The electron beam is focused to a fine probe and scan across the sample in a raster scan pattern. The position of the beam is combined with the detected intensity of the secondary species of electrons to produce an image. When the incident electrons impinge in the solid sample, several interactions occur due to different electron interaction volumes, which produces a variety of signals as shown in Figure. 2.6. There are three primary types of signals in SEM: backscattered electron (BSE), secondary electron (SE), and X-rays. The energy of BSEs is higher than 50 eV. They are closely related with the atoms with high atomic number Z, so the BSE images are valuable for illustrating composition information, especially for the analysis

of the composite. SEs are inelastic electrons with energy of less than 50 eV, which are commonly used for the topographical information of the sample. The X-rays are produced when incident electrons hit the electrons on discrete shells in the sample inelastically. As the excited electrons return to the lower energy shell, they yield X-ray photons with a fixed wavelength. They are related to the different energy levels of electrons on different shells. Thus, X-rays are produced for each element and used for characterization. The working principle is same with the characteristic X-rays in TEM. SEM analysis is a non-destructive technology; in other words, X-rays generated by electron interactions do not lead to volume loss of the sample, so it allows for the repeated analysis of the same sample.

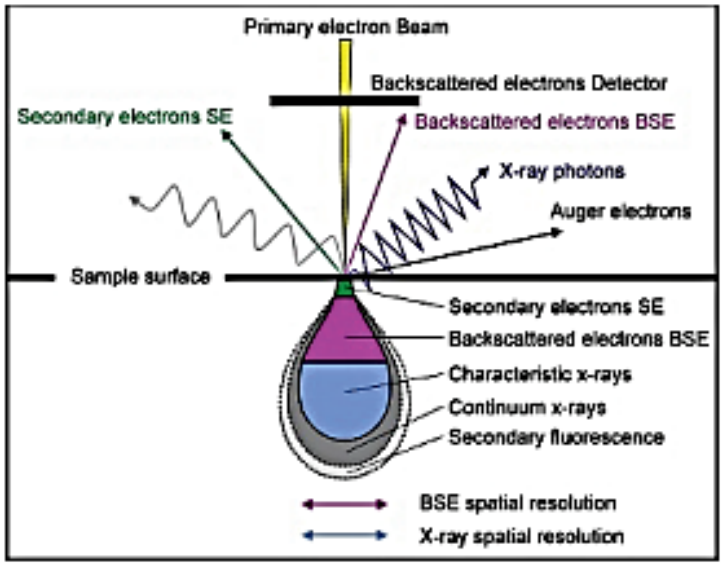

Figure 2.7. Different types of signals generated during the interaction of beam-specimen in SEM [62].

2.3. Materials properties

2.3.1. Polarization-electric field measurement

Polarization as function of electric field are critical parameters for discovery of ferroelectric properties of materials. They are usually measured using sophisticated commercially available testers. In addition to the P-E measurement, several other measurements can be performed, like capacitance-voltage, retention, imprint, fatigue, and leakage current measurements on ferroelectrics, as well as resistive and dielectric materials. The commonly use method is the Sawyer and Tower measurements as shown in Figure 2.8.

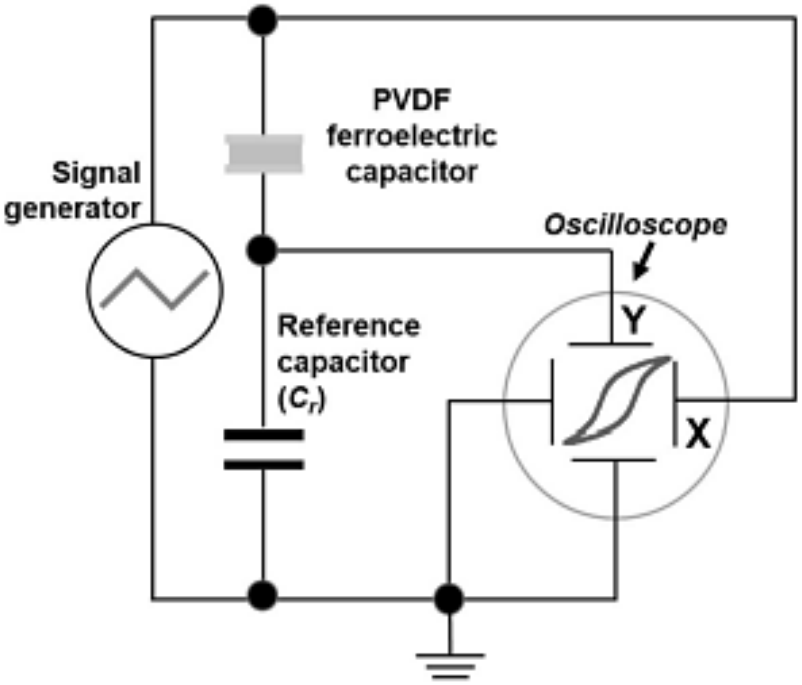

Figure 2.8. Circuit diagram of the Sawyer –Tower measurement [63].

From the Schematic illustration of Sawyer–Tower circuit for ferroelectric hysteresis measurement Figure. 2.8 a voltage source is connected to the ferroelectric capacitor C_F which is connected in series to a sense capacitor C_r of known capacitance such that

$C_r >> C_F$.

The charge Q across a parallel plate capacitor is given by

$$Q = CV \tag{3}$$

where C is the capacitance and V is the applied voltage. The charge can also be written as

$$Q = 2\mathrm{E}rA \tag{4}$$

where A is the cross-sectional area.

From Eqns. 3 and 4, the relationship between the capacitance and polarization can be deduce to

$$C \propto \frac{\mathrm{d}E_r}{\mathrm{dV}} \tag{5}$$

Thus, the polarization is measured by observing the change in the voltage across the reference capacitor.

2.3.2. Magnetic properties measurement

The magnetization measurements are performed by Magnetization dependence on the temperature M-T curves was obtained with a superconductor quantum interference device (SQUID), it is conFigured as a very sensitive magnetometer or gradiometer.

SQUID consists of two Josephson junctions connected in parallel on a closed superconducting loop as shown in Figure. 2.8 (a) [64]. The two Josephson junctions forms a superconducting ring, which in turn is the DC SQUID or double junction SQUIDs. The highest flux variation SQUIDs can measure is in the order of $\sim 10^{-5}\Phi 0$ where $\Phi 0 = 2.07 \times 10^{-15}$ weber [65]. SQUIDs also function as magnetic flux-to-voltage transducers where the sensitivity is set by the magnetic flux quantum. The flux applied to the SQUID and flux contained within a closed superconducting ring operate distinguishably, the first can

assume any value, while the other must be an integral number. Experimentally, the voltage across the SQUID is measured and not the current. As shown in. 2.8 (b). This quantum interference effect provides us with a digital magnetometer. Each "digit" denotes one flux quantum.

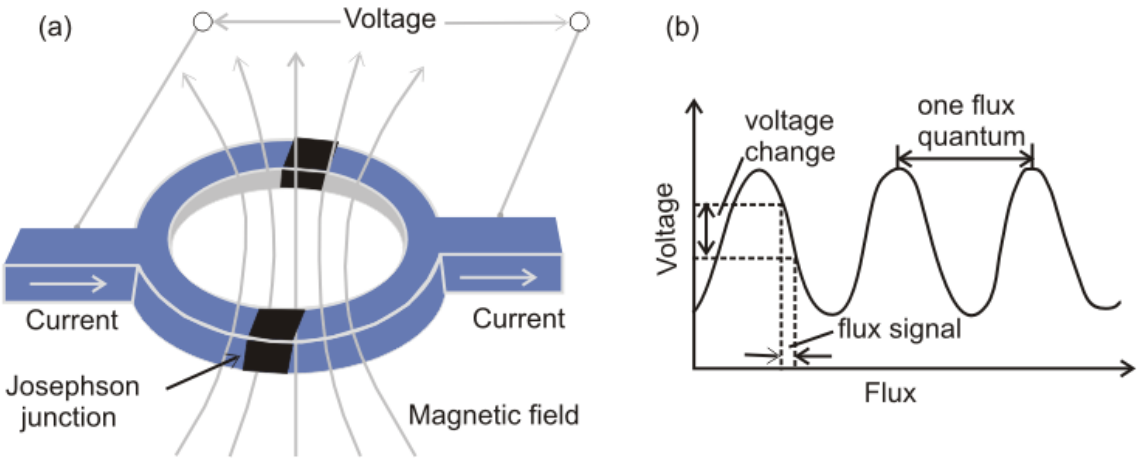

Figure 2.9. a) basis DC SQUID Magnetometer b) The output voltage as a function of applied flux [61].

2.3.3. Mechanical measurement

A standard procedure to analyse the nanoindentation data was proposed by Oliver and Pharr in 1992 [66], which have been widely applied to characterize the mechanical behavior such as elastic modulus of different materials. Although, this method was originally developed for single-phase materials. To prevent substrate influence on thin film, the indentation depth must be small equated to the film thickness [67]. A widely cited guideline is 10–15% of the film thickness. This method measures indent using a calibrated diamond tip on the surface of a sample, and determine its local mechanical response, penetration depths usually 100s nm to several micrometer, comprising Young's moduli (E) and nanohardness (H) [68].

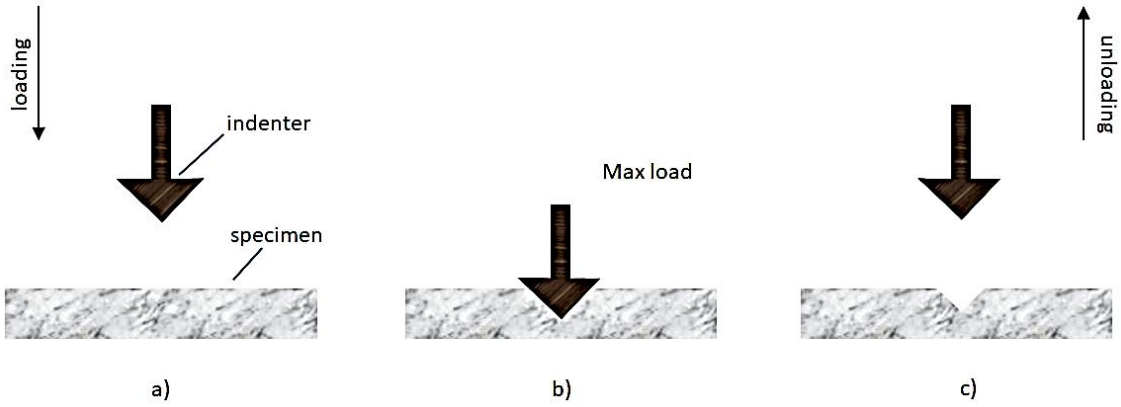

Figure 2.10. Schematic illustration of nanoindentation. a) Loading: b) Load c) Unloading [69].

In Figure 2.10 a) indenter is pressed into the specimen, b) the load (or depth) reaches maximum value, and c) indenter in retracted from the sample.

The processes are as follows: The tip and the sample are modelled as two contacting bodies. From Hertz' theory [70], elastic contact is incorporated, which states that the stiffness

$$S = \frac{dp}{dh} \tag{6}$$

of the contact between two elastic spheres (P = contact force, h = relative movement of the centres of the spheres) is given by

$$E_r = \left(\frac{\sqrt{\pi}}{2}\right) \left(\frac{S}{\sqrt{A_p}}\right) \tag{7}$$

Direct measurement of S and A_p allows E_r to be evaluated, where A_p is the projected area of contact. Figure 2.10 shows a schematic load–displacement curve during loading–unloading nanoindentation experiment. The unloading curve does not follow the loading curve because of the occurrence of plasticity.

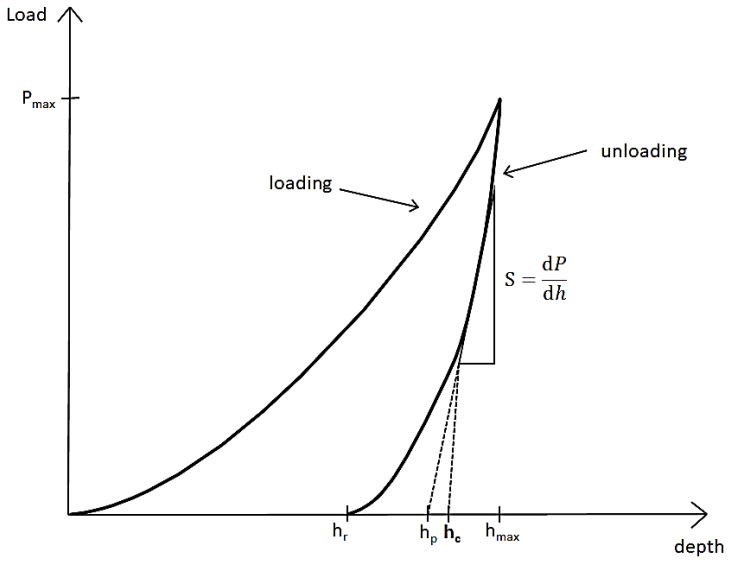

Figure 2.11 schematic load–displacement curve during a typical loading–unloading nanoindentation experiment.

Here, the contact stiffness *S* is measured as the slope of the unloading part of a nanoindentation curve at the maximum load P_{max}. Oliver and Pharr also suggested that if the tip-shape function is known A_p can be obtained by measuring the contact depth *hc* at full load. There are some errors which can be encountered using the Oliver–Pharr method to evaluate nanoindentation data. (i) thermal and electronic drifts (ii) pile-up and sink-in effects, and (iii) creep effects. (i) and (iii) can be corrected, but (ii) may be difficult to correct [71].

3. EXPERIMENTAL METHOD

This chapter give the details of the synthesis of polycrystalline $BiMnO_3$ thin films. It involves the pure and Cu-doped $BiMnO_3$. In addition, a brief explanation of the techniques used for the characterization of these films will be given.

3.1. Thin film growth

Polycrystalline $BiMnO_3$ were grown on three different substrates, firstly on Si (001), secondly Pt-buffered Si (001) and lastly Nb-doped $SrTiO_3$ (100), using RF Magnetron sputtering. The Si (001) has a 5 nm surface layer of amorphous SiO_2, which is known as the native oxide and is present in all silicon substrates. The target was 1-inch diameter of $BiMnO_3$ with 99% purity obtained commercially.

The procedure of cleaning the three substrates were as follows: 1×1 cm^2 single crystal section of each substrate was sonicated in acetone and ethanol for 10 minutes each and rinsed with deionized water. Substrates were then dried in a flux of air. The substrates were loaded into the growth chamber.

The optimal parameters used for the deposition on different substrates is as follows:

Table 1. Parameters for $BiMnO_3$ deposited on Si (001)

Operating Parameters	Values
Pre-sputtering	1hr, 70W
Immersion in Dil HF	12 hrs
Heat treatment,	600 ^oC ,1hrs 30mins
Target to substrate distance	15 cm
Sputtering gas	100 vol.% Ar
Base pressure	$5x10^{-2}$ Torr
Working pressure	$3x10^{-3}$Torr
Substrate	Si (001)
Substrate temperature	700^oC
Deposition temperature	600^oC
RF power	60W
Deposition time	1hrs 5mins
Thickness	100nm
ex-situ thermal treament	600 ^oC for 4 hrs.

Table 2. $BiMnO_3$ deposited on Pt-buffered Si (001) and Nb-doped $SrTiO_3$ (100).

Operating Parameters	Values
Pre-sputtering	1hr, 70W
Target to substrate distance	15 cm
Sputtering gas	100 vol.% Ar
Base pressure	$5x10^{-2}$ Torr
Working pressure	$3x10^{-3}$Torr
Substrate	Si (001) / Nb-doped $SrTiO_3$ (100)
Substrate temperature	600 ± 5 °C
Deposition temperature	600 ± 5 °C
RF power	60W
Deposition time	1hr 8 mins
Thickness	150nm
ex-situ thermal treatment	700 ^oC for 7 hrs.

Parameters for Cu-doped $BiMnO_3$ on Pt-buffered Si (001) was the same as table 2 above, except that different deposition time and different RF power for Cu and $BiMnO_3$ was used in order to acquire different thicknesses of the thin films, with the aim of knowing the influence of Cu on the magnetism of $BiMnO_3$ multiferroic thin films.

All the parameters were kept constant throughout the sputtering process.

Figure 3.1 Cathodic spraying system (sputtering) Brand AJA Model Orion-5.

Ex-situ thermal treatment was performed in air, in a tubular furnace as shown in Figure 3.2, at temperature displayed in table 1 and 2, with heating and cooling rates of 3°C/min. This was done to compensate the volatility nature of Bismuth. Bi powder was added in a crucible within 2 mm of separation with the thin film to compensate for Bi loss.

Figure 3.2 1200°C Split Tube Furnace.

3.2. Thin film characterization

The crystal structure of the films was characterized by X-ray diffraction (XRD) in Bragg-Brentano geometry with Cu-Kα (λ = 1.5405 Å) radiation at room temperature. With patterns collected in the 2θ range (18° < 2θ < 80°) with a scan step size of 0.01° and time count of 20 s for each point. Microstructural characterization was performed by cross-section high-resolution transmission electron microscopy (HR-TEM), with a JEOL TEM-2200FS+Cs microscope operated at 200 kV. Elemental analyses of the thin films were performed, during HR-TEM observations, by energy-dispersive X-ray spectroscopy (EDS). Cross-sectional samples of the films were prepared with a JEOL JEM-9320 focused ion beam (FIB). Observation of surface morphology was conducted by calibrated Asylum Research atomic force microscopy (AFM) model Infinity 3D equipment, in tapping mode. Additionally, Raman spectroscopy was performed using Micro Raman Labram HR VIS-633 Horiba with an Olympus microscope. The spectra were acquired between 180 and 1050 cm^{-1} using an He–Ne laser with 632.8 nm wavelength. The power and spot diameter were 14mW and 15 μm, respectively.

X-ray photoelectron spectroscopy (XPS) analyses were performed in a Thermo Scientific Escalab 250 Xi spectrometer, using the AlKα radiation (1486.7 eV) as an excitation source and a hemispherical analyzer. The surface of the BMO thin films was cleaned by 10 s of Ar Ion bombardment at 2 keV beam energy on an area of 2 x 2 mm^2, to remove all adventitious species of carbon. The energy resolution was 0.1 eV, in ultrahigh vacuum conditions, for an area of 0.625 mm in diameter. The XPS spectra were processed using AAnalyzer® software [72]. For each fitted intensity, the Voigt and Lorentzian function were used, and the Shirley method was employed for extracting the background needed for the curve fittings. To perform the calibration of $BiMnO_{3-\delta}$ data, the binding energy

analysis window in the XPS spectra was set to 83.98 eV which is the standard line energy for Au $4f_{7/2}$, to identify the chemical states related to BMO. The XPS apparatus energy scale was calibrated using the binding energies of Au $4f_{7/2}$ at 83.98 eV, Ag $3d_{5/2}$ at 368.27 eV, and Cu $2p_{3/2}$ at 932.67 eV, to correct the work function of the electron analyzer and to check the scale linearity. Surface atomic ratios of Mn/Bi were calculated from the peak area ratios, and the oxidation ratio between the Mn cations in oxidation states: Mn^{3+}/Mn^{4+} were determined. The value of δ was evaluated, following the procedure of C.D. Wagner *et al*. [73]. Visible-near-IR Spectroscopy (Vis-NIR) was performed in transmission mode, under ambient conditions, using an Evolution 220 visible ultraviolet spectrophotometer Thermo Scientific, to evaluate the optical properties, estimate the energy gap, and determine the charge transfer of the BMO thin films. The background was collected by using a standard blank made of Polytetrafluoroethylene. The electrical transport studies were conducted by measuring the electrical resistivity as a function of temperature, using the two prop method. Magnetization dependence on the temperature *M-T* curves was obtained with a superconductor quantum interference device (SQUID) magnetometer (MPMS XL Ever cool model, M/s Quantum Design Inc., USA), with an applied magnetic field of 7.96×10^4 A/m in the temperature range from 10 to 200 K. Finally, the polarization-electric field (*P-E*) hysteresis loops of the BMO thin films were conducted at 200 and 300 K. The *P-E* loops were set at an AC voltage of 5 V and drive frequency of 0.1 Hz with an LC analyzer with the VISION 5.6.0 software and an RT66 test system from Radiant Technologies Inc.

HRTEM samples of $BiMnO_3$ films, used for the VEELS-TEM analysis, were prepared in a focused ion beam system (FIB) (model JEM-9320FIB) to obtain the appropriate dimensions to do the analysis using the VEELS-TEM technique. VEELS-TEM spectra were acquired using an electron energy loss spectrometer (EELS) (EELS GAT–777

STEM Pack) coupled to a JEM-2200FS (200 kV) system. The measurements were performed at room temperature, using a semi-angle of collection $\beta = 10.7\ mrad$ and a semi-angle of convergence $\alpha = 0$ (parallel beam) with an energy resolution of 1.4 eV. The electron probe beam size was < 1 nm diameter, with a 0.04 eV / channel chosen, for the energy dispersion, to maintain the energy resolution. The zero-loss peak (ZLP) removal was carried out taking the procedures and recommendations of Stöger-Pollach et al. [74,75]. In consideration to eliminate the plural scattering from the VEELS, energy-loss to be separated more effectively, to optimize the analysis of the $BiMnO_3$ films [76]. The EELS information can be provided using the formula[77].

$$\frac{d^2\sigma}{dEd\Omega} = \frac{1}{\pi^2 a_o m_o v^2 n_a}\left[\frac{1}{\theta^2+\theta_E^2}\right] Im\left[\frac{-1}{\varepsilon(q,E)}\right] \quad (8)$$

Where, v is the speed of the incident electron, n_a is the number of atoms per unit volume, $\varepsilon(q, E)$ is the complex dielectric function at energy loss E, and momentum transfer q. a_0 is the Bohr radius, m_0 is the electron rest mass, and θ_E is the characteristic scattering angle for a particular energy loss ($\theta_E = E/\gamma m_0 v^2$).

Additionally, the Fourier-log method to remove plural scattering and the KKA on the single-scattering distribution (SSD) were obtained using the Digital Micrograph™ Gatan Microscopy Suite (GMS 3) software [77] according to the equation:

$$\text{SSD(E)} = \frac{I_o t}{\pi a_o m_o v^2} Im\left(\frac{-1}{\varepsilon(q,E)}\right)\left[1+\sqrt{\left(\frac{\beta}{\theta_E}\right)}\right] \propto \frac{d^2\sigma}{dEd\Omega} \quad (9)$$

Where; $\frac{d^2\sigma}{dEd\Omega}$ is described in equation (1), I_0 is the zero-loss intensity, t is the sample thickness, ε(q, E) is the dielectric function, E is the loss energy by inelastic scattering; β is the collection semi-angle; for small q, $\varepsilon(q, E)$ varies very slowly with q and thus it can be replaced by $\varepsilon(E)$ [77].

Taking into consideration that dielectric constant of a ceramic in the classical dispersion theory, the formula used as:

$$\varepsilon^* = \varepsilon' + \varepsilon'' \quad (10)$$

In which, ε' and ε'' are real and imaginary parts of the dielectric constant.

The dielectric function $\varepsilon^* = \varepsilon'(\mathrm{E}) + \varepsilon''(\mathrm{E})$ can be calculated systematically from the following equations[77,78]:

$$\varepsilon' = \frac{Re\left(\frac{1}{\varepsilon}\right)}{\sqrt{Re(1/\varepsilon)+Im(1/\varepsilon)}} \quad (11)$$

$$\varepsilon'' = \frac{Im\left(-\frac{1}{\varepsilon}\right)}{\sqrt{Re(1/\varepsilon)+Im(1/\varepsilon)}} \quad (12)$$

Where $Re = \left(\frac{1}{\varepsilon(E)}\right)$ is the dielectric response function and can be calculated using the obtained experimental full frequency distribution of $\left[Im\left(-\frac{1}{\varepsilon}\right)\right]$.

Fresnel's law was used to calculate the loss in optical wave intensity observed in the $BiMnO_3$ films due to the reflection of the optical wave [79]. The formula used is reproduced below:

Snell's Law: [80] $n_1 \sin\theta_1 = n_2 \sin\theta_2$ (13)

For any angle of optical wave incidence on the surface of the $BiMnO_3$ films, the reflection loss is calculated using formula (7):

$$\mathrm{RL} = \frac{1}{2}(R_1 + R_2) \quad R_1 = \left[\frac{\sin(\theta_1-\theta_2)}{\sin(\theta_1+\theta_2)}\right]^2 \quad R_2 = \left[\frac{\tan(\theta_1-\theta_2)}{\tan(\theta_1+\theta_2)}\right]^2 \quad (14)$$

For normal 0^o incidence, the reflection loss is given by:

$$\mathrm{R} = \left(\frac{\varepsilon'-\varepsilon''}{\varepsilon'+\varepsilon''}\right)^2 \quad (15)$$

Where $\sqrt{\varepsilon'}$ = n_1 = and $\sqrt{\varepsilon''}$ =n_2

Also, the electric modulus, which is the reciprocal of the complex dielectric constant (ε^*) [81,82], the real and imaginary components of complex dielectric (ε^*) can be transformed into the complex electric modulus (M^*) using formula (9) below;

$$M^* = \frac{1}{\varepsilon^*} = (\varepsilon' - \varepsilon'')^{-1} = M' + M'' \quad (16)$$

Furthermore, another way to determine the complex dielectric constant of $BiMnO_3$ is using the CC plots (electronic relaxation time), as given by equation (10) developed by K. S. Cole and R. H. Cole [83]:

$$(\omega) = \varepsilon\infty + \frac{\varepsilon_s - \varepsilon_\infty}{1+(i\omega\tau)^{1-\alpha}} \quad (17)$$

Where ε^* is the complex dielectric constant, ε_s and ε_∞ are the dielectric constants, ω is the angular frequency of the optical wave, τ is a time constant, and α is the exponent parameter.

To measure the nanomechanical properties of the $BiMnO_3$, a diamond Berkovich indenter was used for all measurements. The hardness, elastic modulus, and stiffness were evaluated using standard procedures of the Oliver and Pharr method with controlled cycles [84–86]. The stiffness was calculated by the Sneddon equation's as follows [85]:

$$S = 2\beta\sqrt{\frac{A}{\pi}}E_r \quad (18)$$

where β is a constant that depends on the geometry of the indenter (β = 1.034 for a Berkovich indenter), E_r is the reduced elastic modulus, which accounts for the fact that elastic deformation occurs in both the sample and the indenter, and A is the contact area

that is a function of the penetration depth or displacement (h) [24]. The elastic modulus, *E* was calculated by considering the compliance of the specimen and the indenter tip combined in series, by the following equation:

$$E = \frac{1-\nu^2}{\left(\frac{1}{Er} - \frac{1-\nu_i^2}{E_i}\right)} \quad (19)$$

Where E_i, E and υ_i, υ are elastic modulus and Poisson's ratio of diamond indenter and specimen respectively. For the diamond indenter E_i = 1140 GPa and υ_i =0.07 are used (G200 Agilent manual, Agilent technology USA). The hardness (H) was calculated using Equation:

$$H = \frac{P_{max}}{A(h)} \quad (20)$$

Furthermore, the analysis depth was set between the 5 to 10% of the total thickness of the film with the purpose of avoiding the substrate hardness influence.

The maximum load used was of 5 mN, with time during the nanoindentation of 10 s to load and 10 s to unload. Peak hold time 1 s was used before to unloading. The Poisson's coefficient of ν = 0.20 was employed. Before evaluation, the coatings of the nanoindenter was calibrated using standard fused silica sample. Tests parameters of area function were: C_0 =24.07, C_1 = -182.16, C_2 = 6831.20, C_3= -25411.22 and C_5 = 18732.10.

4. Results and Discussion

4.1. Polycrystalline thin films of $BiMnO_3$/ Si (001).

$BiMnO_3$/ Si (001) polycrystalline thin films were grown by rf magnetron sputtering. Material can be thoroughly described when the texture and morphology concept is included, this two-aspect play a major role of controlling physical properties such as magnetic, and electrical optical. The analysis between Bragg-Brentano and grazing-incidence diffraction experiments from the perspective of texture characterization is investigated.

4.1.1. Grazing Program

In Grazing, the modeling is systematized to obtain 1D-XRD patterns for Bragg-Brentano and grazing incidence methods. In this software diffractograms are based on the intensities obtained from equation (1) shown above. Required input data are the crystal structure (space group, lattice parameters, atomic positions), experimental parameters (e.g. wavelength) and proposed texture characteristics. Texture data are preferred orientation indexes (*hkl*) and IPF width [87]. Based on these data, Grazing obtains intensities without textures and applies the correct modulations for each method. For Bragg-Brentano method, the inverse pole Figure, eq. (3), modulates the intensities of peaks. In grazing incidence, the intensities' modulation is produced by the direct pole Figures, calculated by eq. (4).

The software has been developed with Python language [88]. It utilizes modules such as Matplotlib [89], NumPy [90] and SciPy [91]. Grazing offers a representation of 1D-XRD patterns of materials such as thin films and surfaces under the effect of texture measured with the Bragg-Brentano and grazing incidence methods. Given the preferential

orientation Grazing determines the 1-D XRD pattern for both methods, this to demonstrate the quantitative difference of crystallites orientation at the same distribution width.

4.1.2. 1D-XRD: Bragg Brentano vs Grazing incidence

The integrated intensities of x-rays diffraction peaks are affected by crystallographic texture, differently, depending on the measurement geometry.

$$I = [I_0 \; K |F|^2 \; p \; (LP) \; A \; D / v^2] \cdot T \tag{21}$$

$$T = \begin{Bmatrix} P_h[\varphi(\theta_{Bragg})] & Bragg - Brentano \\ R(h,k,l) & Grazing\ incidence \end{Bmatrix} \tag{22}$$

I = Incident beam intensity, K = Instrumental constant, $|F|$ = Structure factor, p = Multiplicity factor, (LP) = Lorentz-polarization factor, A = Absorption, D = Debye-Waller factor, v = Cell volume and T = texture factor. In Bragg-Brentano configureuration, the intensities are modulated by the inverse pole Figure of the normal to the sample surface direction. In grazing incidence experiments, the modulating factors are the corresponding direct pole Figures, evaluated at the Bragg angles.

The model applied in the present work consists in proposing a Gaussian-shaped inverse pole Figure and proceeding with further calculations on dependence of the considered case.

Model texture:

$$R(h) = R_0 e^{-0.5(\varphi/\sigma)^2} \tag{22}$$

φ denotes the polar angle, measured from the location of the IPF maximum, σ is the standard deviation of the orientation distribution and R_o is a normalization constant, such that the integral of R(h) over the whole unitary sphere has a value of 4π.

Calculation of direct pole Figures from the symmetry axis inverse pole Figure proceeds by application of the Fundamental Equation of Fiber Textures [92], eq. (4):

$$P_h(\varphi) = \frac{1}{2\pi}\int_0^{2\pi} R(\varphi, \psi)\, d\psi \qquad (23)$$

In order to analyze the two different diffraction geometries, Gaussian-shaped inverse pole Figure was proposed, with two modulating factors, namely: inverse pole Figure and direct pole Figure to analyze in detail the texture orientation of the film. Bragg-Brentano induces significantly intense (-1 l 2) peaks. In the grazing incidence experiment, the (-1 l 2) peaks were invisible, and peaks were less intense. Bragg prove to satisfy the condition. $BiMnO_3$/Si (001) were observed to undergo a dramatic change in crystal texture Figure 4.1.

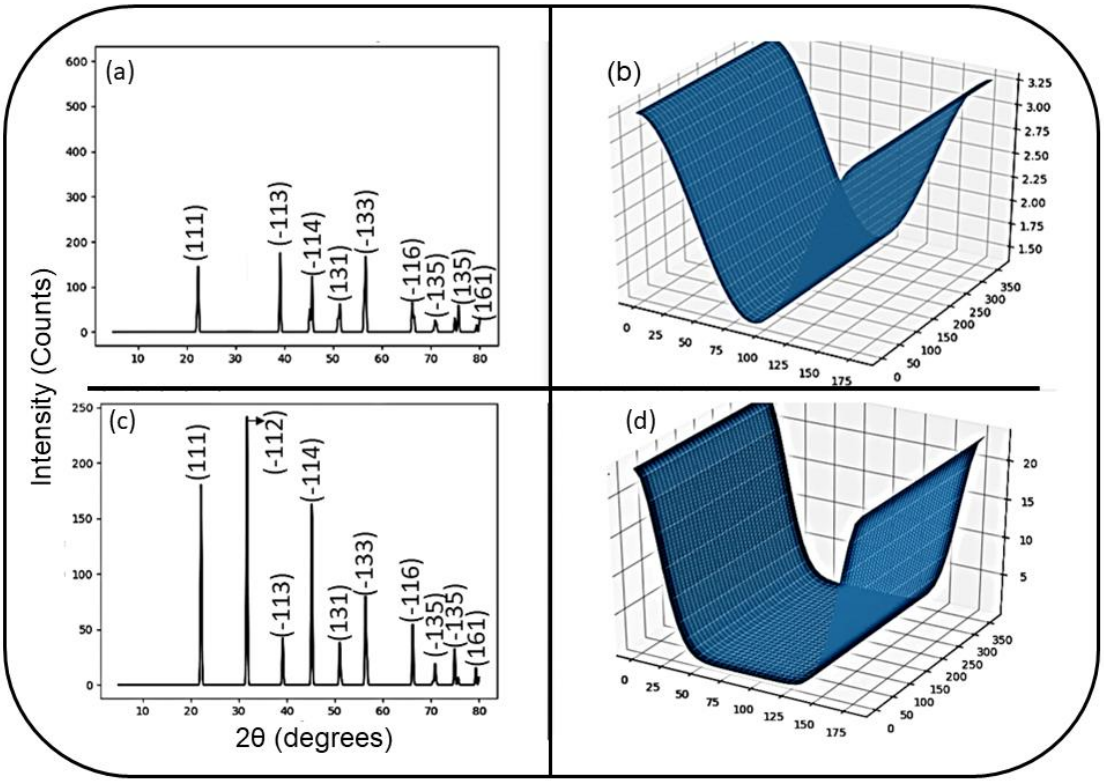

Figure 4.1. a) Grazing-incidence diffractogram of $BiMnO_3$/Si (001), b) Inverse pole Figure of a) c) Bragg-Brentano diffractogram of $BiMnO_3$/Si (001), d) Inverse pole Figure of c).

Hypothetically, Cu-Kα diffraction experiment with a $BiMnO_3$ thin film exhibit an extremely sharp (-1,1,2) texture. The difference in results obtained by the two considered experimental methods is striking. Bragg-Brentano produce significantly intense (-1,1,2) peaks. On the other hand, in the grazing incidence experiment, the (-1,1,2) peaks practically disappear.

4.1.3 X-Ray Diffraction (XRD) of $BiMnO_3$ on Pt-buffered Si (001)

X-ray diffraction (XRD) was performed on two optimized thin films, one as-grown henceforth, named AG-BMO, and the other one, subjected to an *ex-situ* thermal treatment,

named TT-BMO. The XRD patterns of the AG-BMO and TT-BMO thin films are shown in Figures, 4.2 (a) and (b). Both thin films confirmed the formation of monoclinic-type crystal structures. The plots are of a logarithmic scale to be able to visualize all the peaks. Figure. 4.2 (a) is indexed with $P2_1/c$ space group No. 4 reference code: 01-076-7062 while Figure. 4.2 (b) conform to $C2$ space group No. 5, PDF: 1-089-4544. There is no appreciable texture in both film structures, these make it a difficult task to completely ascertain the growth orientation. Under each XRD pattern, the standard diffraction patterns are shown. The intense peaks at $2\theta = 39.87°$ and $69.87°$ correspond to the reflections of Pt (111), and Si (400), of the epitaxial Pt (111)-buffered Si (001) substrate. The pattern in Figure. 1(a) shows the evidence of Bi_2O_3 as an impurity with a secondary phase, located at $2\theta = 26.41°$, and the reference PDF card end at $2\theta = 71.037$. Similar results have been reported by other groups for thin films deposited under similar conditions over a temperature range of 500 – 600 °C [39]. In Figure. 1(b) no secondary phases are detected by XRD, demonstrating that the addition of Bi and O during TT leads to the formation of $BiMnO_3$. These results show a remarkable structural phase transition from $P2_1/c$ to $C2$, which is a polymorph succession in the high-temperature evolution of perovskite-type oxides, due to the *ex-situ* TT. There exists a slight shift to the right in Pt (111) peak of the TT-BMO film, to a smaller angle due to the tensile stress, as the result of the temperature in the furnace during the ex-situ thermal treatment. The addition of Bi during TT leads to the formation of $BiMnO_{3-\delta}$ in accordance with the XPS result in Figure 4.11.

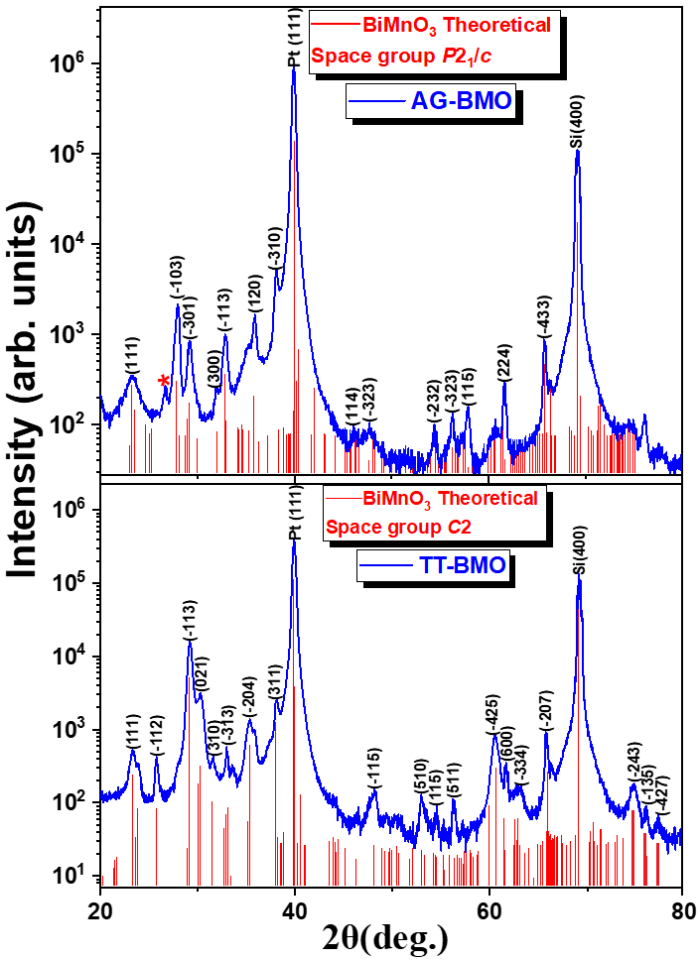

Figure 4.2. X-ray diffraction patterns of a) AG-BMO and b) TT-BMO on Pt (111) template layers.

Additionally, the diameter *D* of crystallites in the AG-BMO and TT-BMO thin films were calculated, from the full width at half maximum (FWHM) of the highest intense peak $(\bar{1}03)$ in AG-BMO and $(\bar{1}13)$ in TT-BMO using the Scherrer equation:

$$D = \frac{k\lambda}{\beta cos\theta} \tag{24}$$

Where k is the shape factor = 0.9, λ is the wavelength of the target = 1.54060 Å, θ is Bragg's angle and β represent FWHM of the diffraction peak. The crystallites *D* sizes were 42 nm and 46 nm for the AG-BMO and TT-BMO films, respectively. In this sense, the larger crystallites observed in the TT-BMO films correlate well with the grain's

distribution and height profile of the BMO films revealed later in this dissertation by the AFM analysis.

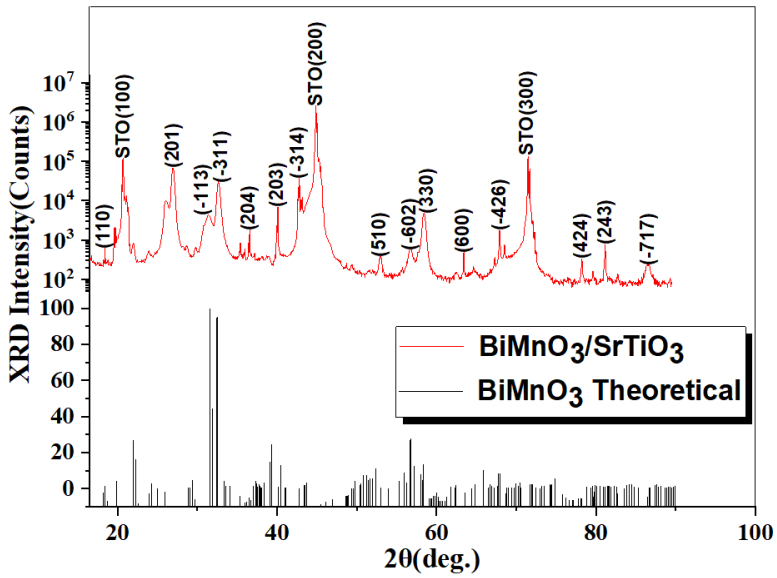

Figure 4.3. XRD diffraction pattern of $BiMnO_3$ films grown on (100) Nb-doped $SrTiO_3$.

XRD diffractions analysis of $BiMnO_3$ film at 293 K, and below the XRD patterns are the standard diffraction patterns, shown in figure. 4.3. The diffraction peaks were indexed based on monoclinic-type C_2, space group number 5 with reference code: (PDF: 1-089-4544). All the peaks are associated with pure $BiMnO_3$. The growth of the film was heteroepitaxial with a small lattice-mismatch, approximately 0.14% with a_{BMO} and -10.66% with b_{BMO}. The lattice constant of the films was calculated to be 5.52 Å, comparable to that measured by T. Atou *et al* [93], indicating a fully relaxed strain state and in the films. A logarithmic scale was used to visualize all the peaks. The most intense peak in the XRD pattern corresponds to the substrate. The appearance of multiple peaks emerges, because of the polycrystalline nature of the film. Having stoichiometry with fully crystallized grains, as indicated by the several planes. In addition, the XRD spectra shows no traces of impure phases such as MnO_2/ Bi_2O_3.

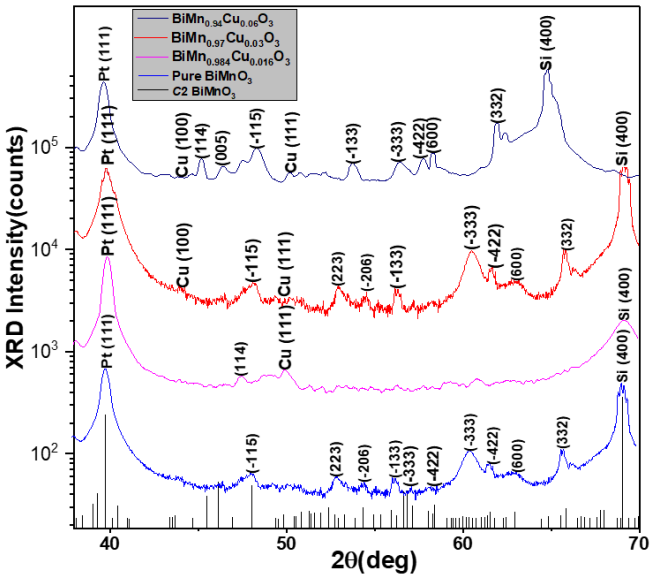

Figure 4.4. X-ray diffraction patterns of pure $BiMnO_3$; $BiMn_{0.984}Cu_{0.016}O_3$; $BiMn_{0.97}Cu_{0.03}O_3$; and $BiMn_{0.94}Cu_{0.06}O_3$ thin films.

The XRD patterns of pure $BiMnO_3$ and three Cu-doped thin films grown on Pt-buffered Si (001) substrate are displayed in figure. 4.4. The XRD diffraction peaks of all samples are matched with those of the monoclinic-type *C*2, space group number 5 with Reference code: 1-089-4544 [40,93] were Cu is consistent with the standard data [94]. All films are of polycrystalline species. The two intense diffraction peaks are from the substrate (111), and (400). The peaks seem to increase and become more intense with the increase of dopant. There also exist an obvious shift in the peaks of the sample with the highest amount of Cu, and it is toward the lower angle side, this indicates the manifestation of the Cu. Variation in the intensity of the XRD peaks of the doped samples implies that the doping has occurred effectively. Some peaks tend to merge with each other indicating that the doping caused a structural change, but no phase transition occurred. From the $BiMnO_3$ patterns, there is a predominant growth of $BiMn_{0.94}Cu_{0.06}O_3$ and $BiMn_{0.97}Cu_{0.03}O_3$ microcrystal with the c-axis tilted around 54 degree towards the plane of substrate at higher doping, while for slightly doped sample *c*-axis is perpendicular to

the plane of the substrate. The average crystallite sizes of the film were calculated to be 46.2, 37.4, 28.5, and 25.9 nm, following the sequence in Figure. 1 from the pure $BiMnO_3$ to $BiMn_{0.94}Cu_{0.06}O_3$, using the Debye–Scherrer formula [95]. The crystallinity results show a decreasing trend with the increase in doped samples thereby conforming to a decrease in the net magnetic moment as shown in Figure 5.3. This behavior is common when doping with transition metals [95–97]. In others recent research doped element increase the magnetic properties of a multiferroic [98,99].

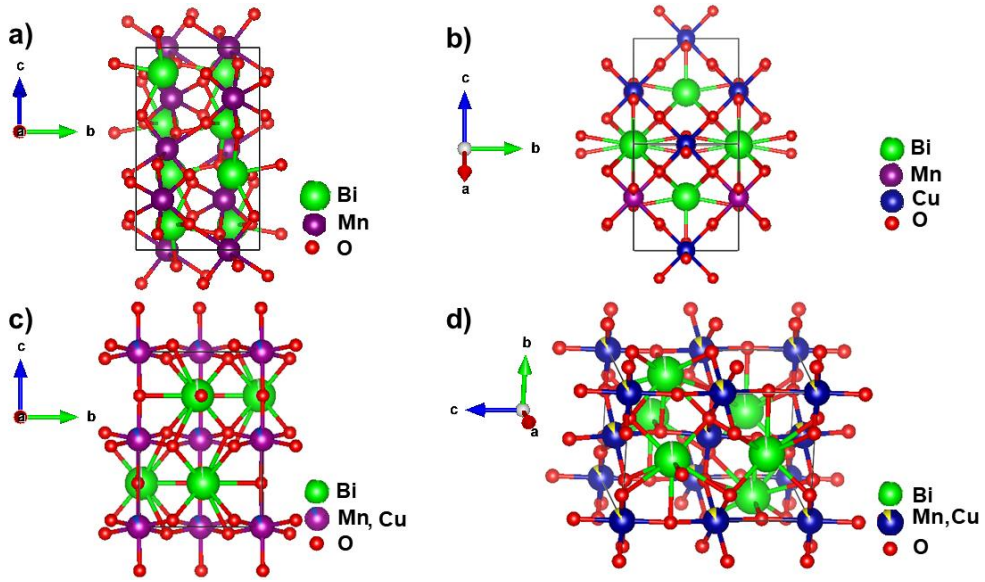

Figure 4.5. Schematic 3D representations of the crystal structure for pure $BiMnO_3$ and the three Cu-doped samples: a) $BiMnO_3$; b) $BiMn_{0.984}Cu_{0.016}O_3$ c) $BiMn_{0.97}Cu_{0.03}O_3$; and d) $BiMn_{0.94}Cu_{0.06}O_3$.

Figures 4.5 a) – 1 d) schematically shows crystal structure of the perovskite phases found in the samples under study. They illustrate the ideal perovskite structure having ABO_3

stoichiometry, which consists of a three-dimensional framework of corner linked Mn^{3+}. Mn^{3+} is bonded to six O^{2-} atoms to form corner-sharing MnO_6 octahedra. Bi^{3+} is bonded in a 6-coordinate geometry to six O^{2-} atoms. The Cu according to it respective ions in (b), (c) and (d) are bonded in a square co-planar geometry to four equivalent O^{2-}. In total, twelve coordinated A-cations fill the cavities formed by the framework. This arrangement of ions generates a crystal structure described by the monoclinic *C*2 space group.

4.2. Microstructure characterization

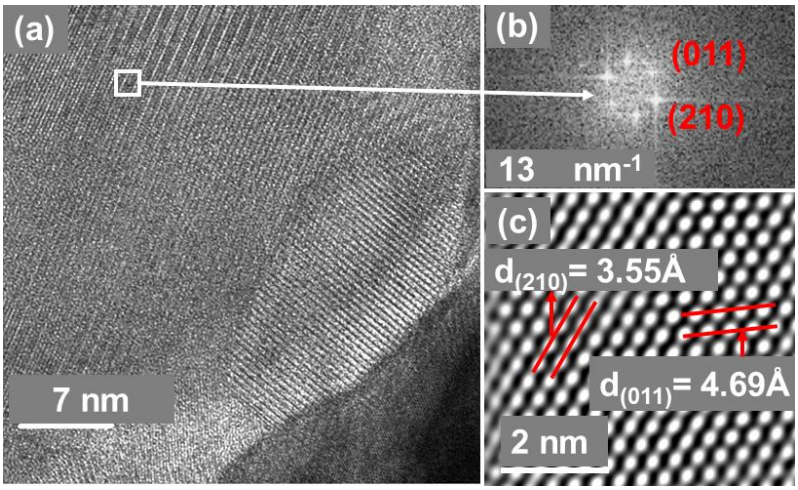

Figure 4.6. a) Representative HR-TEM micrograph of a polycrystalline AG-BMO thin film b) Fast Fourier transform of the square region in a), c) Inverse fast Fourier filtered image from the pattern in b).

HR-TEM micrograph shows crystallites composed of the AG-BMO film, randomly oriented in Figure. 4.6. a), Figure. 4.6. b) shows the fast Fourier transform emerging from the square in figure. 4.6. a). Figure. 4.6. c) is the inverse fast Fourier filtered image corresponding to the same region, in the white square that enabled the measurement of two interplanar distances: 3.55 and 4.69 Å corresponding to the $d_{(210)}$ and $d_{(011)}$ planes of the $P2_1/c$-BMO crystal, similar to the findings of Montanari *et al*. [21].

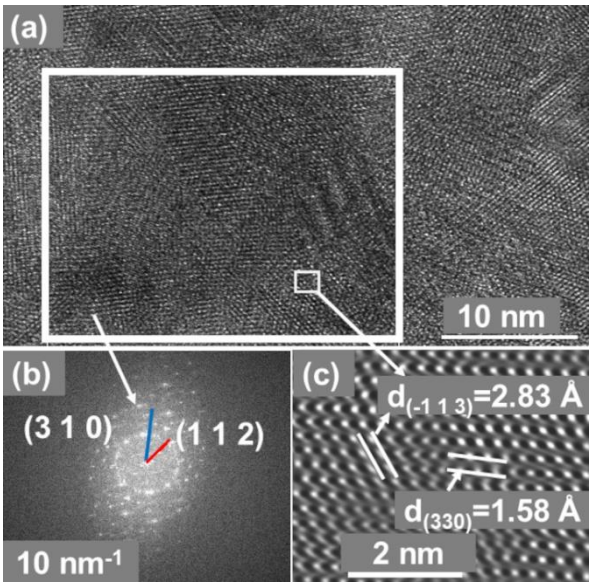

Figure 4.7 a) HR-TEM image of a polycrystalline TT-BMO film, b) Fast Fourier transform pattern of the region in a), c) Atomic periodicity obtained from the inverse fast Fourier transform of b).

On the other hand, Figure. 4.7 a) displays HR-TEM micrograph of a TT-BMO polycrystalline thin film. Figure. 4.7 b) shows the fast Fourier transform of various crystals from the area inside the large white square in Figure. 4.3 a). Several crystallites were involved; it is possible to notice the presence of a Debye ring pattern that clearly shows the (310) and (112) crystalline planes. The inverse fast Fourier filtered image of a small region of the film is shown in Figure. 3 c) indicating two interatomic distances that match well with the ($\bar{1}$13) and (330) planes of the *C*2 phase of BMO.

4.3. Raman spectroscopic studies of $BiMnO_3$

To further analyse the structure, $BiMnO_3$ was investigated by using Raman spectroscopy, which is known as a sensitive technique for detecting phase or more subtle structural rearrangements due to coupling phenomena in ABO_3 perovskites [19,20]. Figure 2 presents Raman spectra measured at room-temperature spectra.

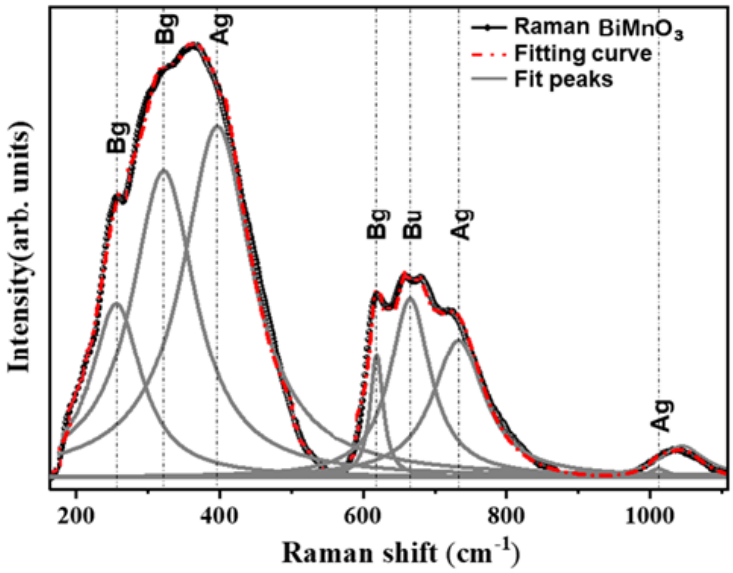

Figure 4.8. Measured Raman scattering spectra of the $BiMnO_3$ thin film (red dotted line), fitting spectra (black doodling circles) and the decomposed active modes (gray solid line) performed in the Raman spectral shape to identify the vibration modes of $BiMnO_3$ using OriginPro software.

The Raman spectrum (black dotted line) acquired in a range of 180–1050 cm^{-1} is shown in Figure 4.8. Three prominent Raman bands emerged at 398.1, 620.8, and 1009.2 cm^{-1} on this polycrytalline $BiMnO_3$ sample. According to the Lorentz equation in OriginPro software [100] the decoconvolution peaks of $BiMnO_3$ sum up to 52 close to the of the calculated 57 phonons [101,102], for the monoclinic phase reported elsewhere with the *C*2 space group (C_2^3 No. 5) [40]. The factor group analysis of all phonons with Γ point in Brillouin-zone center predicts the following: $\Gamma_{C2} = 29A(z, x^2, y^2, z^2, xy) + 31B(x, y, yz, xz)$[101,103] where A and B denote acoustic vibrations. in the bracket shows the Raman, and IR activity respectively. At the Γ point, long-range electrostatic forces split the active modes into transverse (TO) and longitudinal (LO) oscillation modes represented in table 3. The Raman modes were obtained by fitting the experimental spectra (black doodling circles), peak fitting curve (red solid line), and fit peak (gray

solid line) with Gaussian-Lorentzian shape components according to the Raman active modes [104,105] The strong bands are located at 234.5, 374.1, 398.1, 620.8, 665.8, 729.3, and 1009.2 cm^{-1}, their respective oscillation modes (TO) and longitudinal (LO) are illustrated in table 3.

Tabel 3. Raman frequencies of IR, and Raman active modes in the $BiMnO_3$ thin film.

Type	cm^{-1}	IR
TO	234.5	Bg
TO	374.1	Ag
TO	398.1	Ag
LO	620.8	Bg
TO	665.8	Ag
TO	729.3	Bg
LO	1009.2	Ag

The most instense band at 398.1 cm^{-1} belongs Ag symmetry of transverse optical (TO) phonon mode [Ag, (TO)]. The second intense and broad band is located near 374.1 cm^{-1}; this feature is associated with Bg (TO) phonon [39,106]. The sharp low intensity band near 620.8 cm^{-1} is associated with Bu symmetry of longitudinal optical (LO) phonon mode [Bu, (LO)], and high frequency band near 1009.2 cm^{-1} is related with Ag, (LO) phonons. These bands are characteristic for $BiMnO_3$ ferroelectric phase with monoclinic symmetry [101,107]. The peaks at 260 and 1009.2 cm^{-1} can be attributed to the lattice and stretching vibrations of the Mn-O bond. It is important to note that, the observed bands corresponds to several phonons because frequencies of the modes are relatively close. Raman activity can arise due to several reasons, such as: grain boundaries, intergrain stresses and phonon anomalies which are common for multiferroics if not all. $BiMnO_3$, $HoMnO_3$, $LuMnO_3$, and $YMnO_3$ [108]. To our knowledge there is no report on *C*2 space group of $BiMnO_3$ to compare the modes and frequencies to our experimental result.

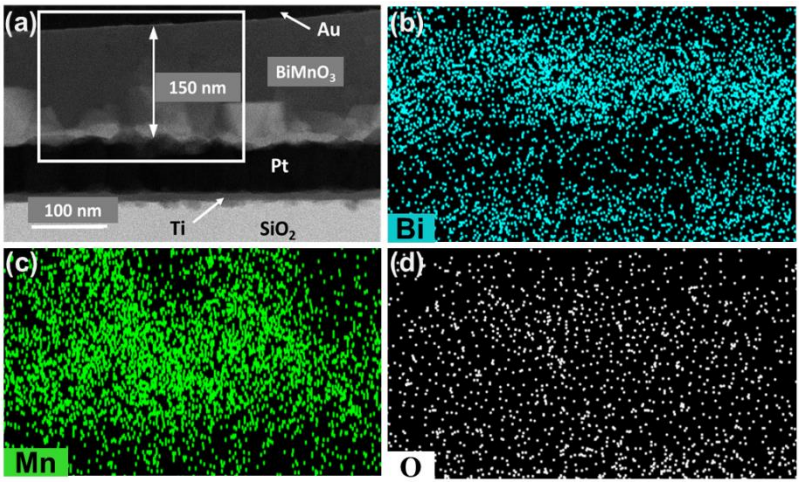

Figure 4.9 a) TT-BMO film shown in cross-section by TEM. EDS elemental mappings of b) Bi, c) Mn, and d).

A low magnification TEM micrograph of the TT-BMO thin film is shown in Figure. 4.8 a). Au capping layer was used for the FIB cross-section preparation. Several regions were observed in order to measure an average thickness of 150 nm. Figures. 4.8 b) – d) are the EDS mappings of Bi, Mn, and O, respectively, showing a homogeneous distribution along with the thickness of the film.

4.4. Atomic force microscopy (AFM)

To assess the surface morphology of the samples, a 1x1 μm^2 AFM scan was performed. The micrographs obtained from the 100 and 150 nm thickness of $BiMnO_3$ films are shown in Figures 4.9 a) and b).

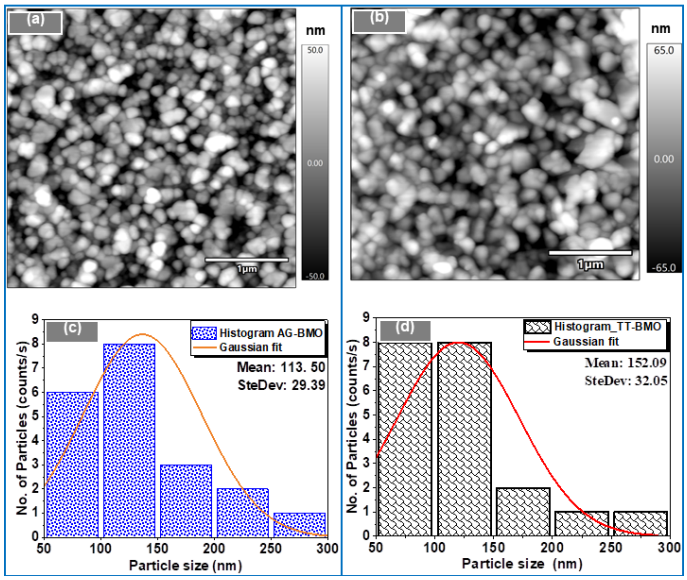

Figure 4.10. AFM micrograph of the surface of BMO thin films grown on Pt (111): a) AG and b) TT thin film c), and d) are the histogram plots for the particle size distribution corresponding to the AFM images in a) and b).

Figures 4.10 a) and b) shows AFM micrographs of the AG-BMO and TT-BMO samples respectively. The high root mean squared (rms) roughness of 25 nm and 32 nm, agrees well with the *z* scale of 100 and 130 nm, respectively. These morphological changes were induced by the *ex-situ* TT by the increased annealing temperature of $\Delta T = 100$ °C. In agreement with grain growth theory, the higher the temperature the higher the grain size, as well as the crystallite size. This was expected to improve the stoichiometry of the thin film. Figures. 4.10 c) and 5 d) represent a regular histogram plot for the grain size distribution of the AG-BMO and TT-BMO samples. After obtaining the grain size distribution curves through a Gaussian fitting, the calculated mean grain size was 110 nm, and 150 nm (with a standard deviation of about 30 nm in both cases).

4.5. X-ray photoelectron spectroscopy (XPS)

In view of the composition of TT-BMO sample, XPS analyses were performed to identify the chemical states of Bi, Mn, and O. Figure. 4.11 a) shows the survey scan performed over a binding energy range from 0 to 1400 eV. The XPS lines in the survey spectra are associated with Bi, Mn and O ions. Figures. 4.11 b) - d) shows the survey scan of the Bi, Mn, and O. The black line with doted circles represents the experimental data, red solid line corresponds to the fitting curve, green and blue solid lines are associated with chemical species, while the dotted lines correspond to the background. A Shirley-type background was considered in all regions of the spectrum. The Bi survey scan in Figure. 4.11 b) clearly shows the spin-orbit coupling doublets of Bi $4f_{7/2}$ and $4f_{5/2}$ near 158.5 and 164 eV, respectively [14,20,109] confirming the trivalent oxidation state of bismuth atoms in BMO [110]. The spectrum showing a doublet peak arises as a consequence of the energy splitting due to spin-orbit coupling.

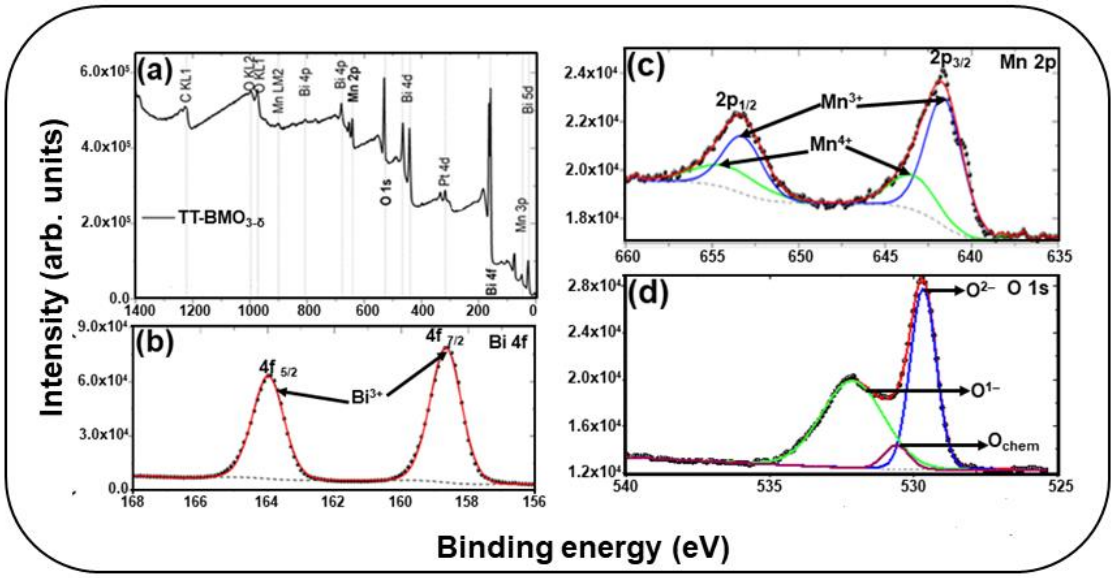

Figure 4.11 a) XPS survey spectra showing the main photoelectric and Auger peaks associated with the elemental analysis of the TT-BMO thin film. XPS spectra scans of b) Bi 4*f*, c) Mn 2*p*, and d) O 1*s* regions.

Figure. 4.11 c) displays the XPS spectra for the peaks related to Mn atoms. As expected, broadening of peaks for Mn 2*p* doublet is observed due to the formation of the oxide. The presence of its signal is shifted toward higher binding energies. Four components were considered to reproduce the broadening in the Mn 2*p* line, which is related to structural defects [20]. The difference between the two peaks in each Mn $2p_{3/2}$ and Mn $2p_{1/2}$ orbitals indicates that the oxidation state is not precisely Mn^{3+} or Mn^{4+}, it is concurrently 3+ and 4+. This can be understood through the percentage contributions of Mn in $BiMnO_{3-\delta}$, which are Mn^{3+} (72.98 %) and Mn^{4+} (27.32 %). Moreover, the deconvoluted core-level XPS spectrum of surface oxygen is surveyed to study the status of surface oxygen, as shown in Figure. 4.11 d). The O 1*s* spectra was fitted with three peaks at 529.7, 530.6, and 532.1 eV. The O^{2-}, which is the main energy peak located at 529.7 eV is assigned to bonding state in the BMO perovskite, while the O^{1-} peak observed at 530.6 eV corresponds to oxygen atoms participating in Mn- and Bi-oxides with 4+ and 3+ metal-oxidation states, respectively [111–113]. The O 1s peak at 532.1 eV corresponds to oxygen in chemisorbed species at the surface [14,114]. The fitted peak intensity was used to estimate the oxygen content in its particular state, its content was found to be 43.2% oxygen in perovskite lattice and 56.6% was chemisorbed. Surface charging was compensated using a charge neutralizer, which is a combination of two charges neutralizing an external and an inlens (the later is inside the electrostatic lenses of the analyzer). The charge neutralization ensures that the peaks are not heavily shifted, a confirmation of that is the peak position of O 1*s* in 529.7 eV approximately. As evaluated, the oxygen non-stoichiometry in $BiMnO_{3-\delta}$ contributes a considerable fraction of partially

occupied 3d orbitals of Mn states (Mn^{3+} and Mn^{4+}) as observed in Figure. 6(c). Mn/Bi atomic ratio was evaluated from the Bi $4f_{7/2}$ (158.5 eV), and Mn $2p_{3/2}$ (642.2 and 642.6 eV) for Mn^{3+} and Mn^{4+}. Their respective ratios are: Mn/Bi (0.89), Mn^{3+}/Mn^{4+} (0.13), and δ, was estimated to be 0.07, inducing the composition to $BiMnO_{2.93}$.

4.6 Optical measurements

This section comprises of a non-destructive and wear-free measurements of the optical properties of $BiMnO_3$ using different technology: Ultraviolet-visible (UV-Vis) spectrophotometry and Valence Electron Energy Loss Spectrometry (VEELS).

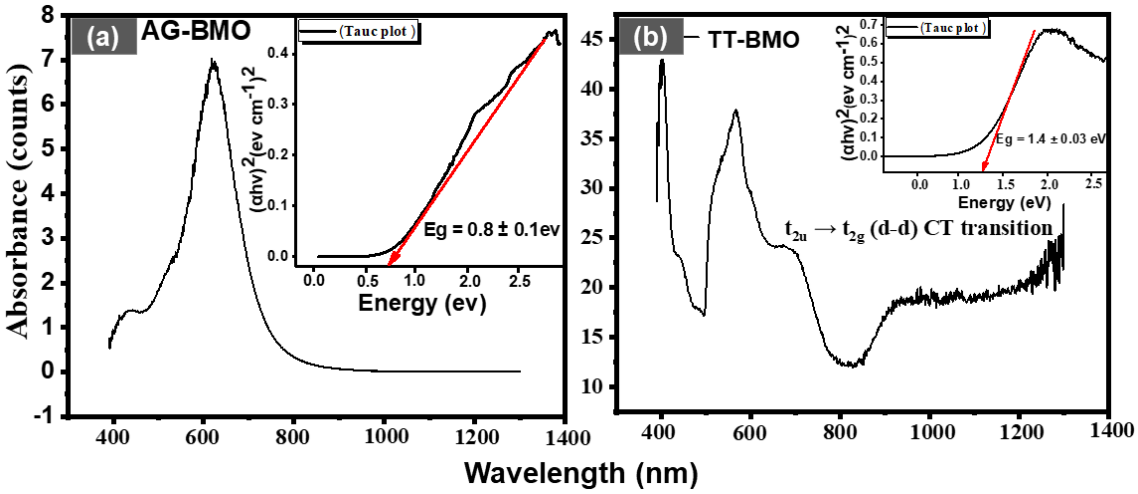

Figure 4.12. Room temperature absorbance type UV-Vis-IR spectrum of a) AG-BMO and b) TTBMO thin films.

UV-Vis-IR absorbance spectrum of AG- and TT-BMO thin films are shown in Figures 4.12 a) and 4.12 b), with a recorded wavelength region from 400–1400 nm. The optical band gap of the samples has been calculated by the Tauc plot method [39,115–117] The insets are the Tauc plots for both samples. Figure. 4.12 a) shows the spectrum of the AG-BMO thin film and the estimation of the energy band gap of 0.9 ± 0.07 eV as shown by

the red line in the inset. The inception of the absorption, located at about 406 nm, indicates that the AG-BMO thin film has good white-light absorption properties in the visible light regions (400 - 609 nm) [117,118]. Figure 4.12 b) shows an intense absorption band for TT-BMO film at about 706 nm, which agrees well to a strong dipole-allowed $t_{2u} \rightarrow t_{2g}$ (*d-d*) charge transfer transition, which is a distinguishing attribute reported in the literature [119]. The other two intense peaks at 406 and 663 nm arise from the various valence states of Mn. The broad range of absorbance spectra shows a greater absorption in the wavelength region of 400 nm, which is extended up to 706 nm. The energy band gap is 1.4 ± 0.03 eV, which is slightly larger than 1.25 eV of typical BMO nanoparticles prepared by sol-gel [38] and bulk BMO with a band gap of 1.1 eV) [24,39]. The increase of the values of the band-gap in nanometric materials is usually associated with crystallite size reduction, which in this case, the present samples seem to be out of the trend, probably indicating that the grain boundaries play a significant role in the diminution of the band-gap of the AG-BMO thin film.

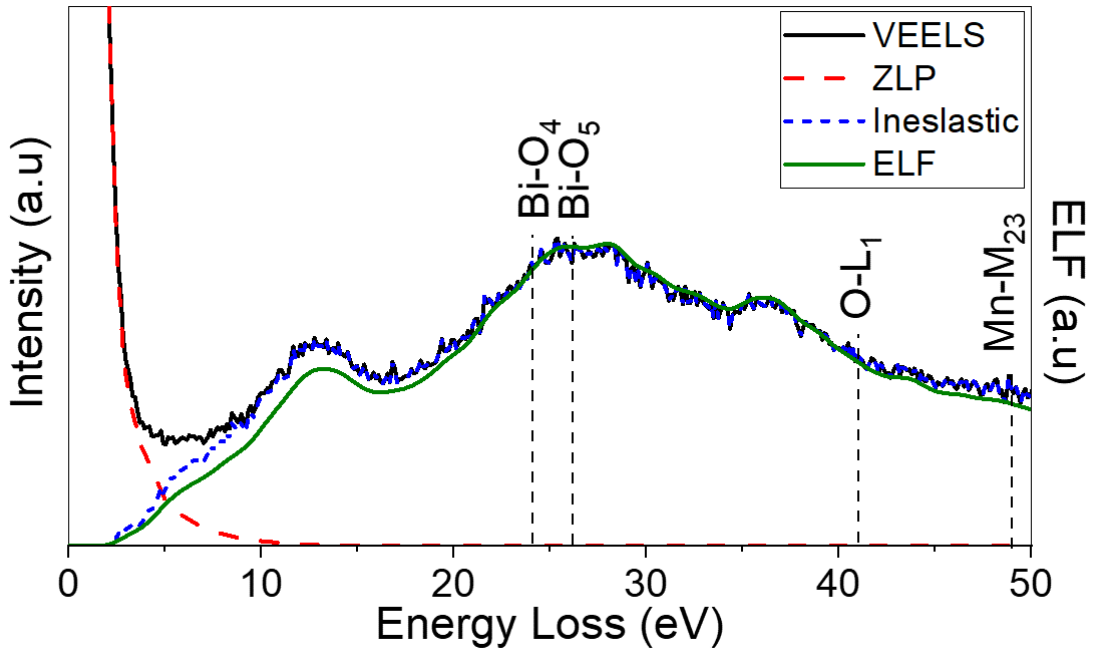

Figure 4.13. Typical VEELS-TEM spectra from analysis of a BiMnO3 film: full VEELS (black), ZLP (red), inelastic contribution (Green) and, ELF (dotted blue).

Figure 4.13. displays a VEELS–TEM spectrum in black line with energy-loss range (0–50 eV) of $BiMnO_3$, a red dotted line corresponding to the ZLP spectrum, a blue dotted line correlated with the inelastic contribution, and the green line representing the ELF. To deconvolute the ZLP spectrum, inelastic scattering was extracted using the reflected tail model, then using the Fourier-log method. The SSD spectrum was obtained using equation (1) and applied specific Gatan Microscopy Suite software routines. The SSD spectrum was developed using the KKA function to obtained ELF and complex dielectric function (ε' and ε''), The fits described above are based on using the $BiMnO_3$ refraction index 2.16 [24,120]. Moreover, elemental analysis was performed in the range 0-50 eV, where elements of $BiMnO_3$ were obtained from references [24,121].

It is pertinent to note that the investigation of $BiMnO_3$ films using the VEELS technique has not been reported in the literature.

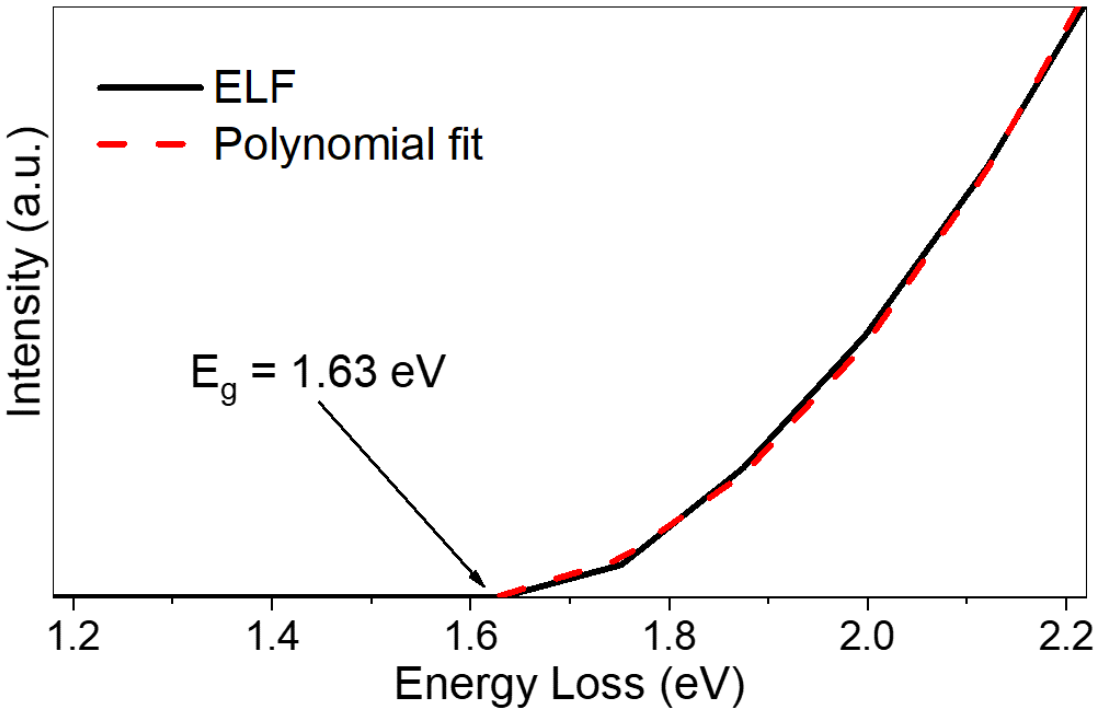

Figure 4.14. Experimental and polynomial fitting curve related to the ELF plot from analysis of a $BiMnO_3$ film (intensity versus energy loss).

The analysis of ELF in Figure 4.14 is to obtain the bandgap of a $BiMnO_3$ film, using a polynomial fit in the ELF (red dash line) in the energy loss range of 1.2–2.2 eV. The onset energy of the spectrum in ELF was evaluated and the bandgap energy was calculated using the Rafferty and Brown methodology [122], by using a polynomial fit as $A + C(E - E_g)^2$, where A and C are constants and E is the energy loss [123,124], for which the fitting value obtained was $E_g = 1.63\, eV$. The extinction coefficient k and the refractive index n = 2.16 were obtained using the dielectric function equation ε^* (E) = $\varepsilon'(E) + \varepsilon''(E)$. These were taken into consideration during the application of K–K sum rule to normalize the ELF curve. Different studies show a relatively small bandgap for $BiMnO_3$ around 1.1 eV to 1.7 eV [16,121,125]. Other oxide-based photovoltaic and multiferroic materials, exhibit large bandgap (3.1 eV) [83], which limits their conversion efficiency in absorber-based photovoltaic devices [125,126]. $BiMnO_3$ exhibits a narrow bandgap, which may contribute to the development of a new strategy for designing high symmetry $BiMnO_3$ films for efficient optoelectronic applications with a strong photovoltaic effect.

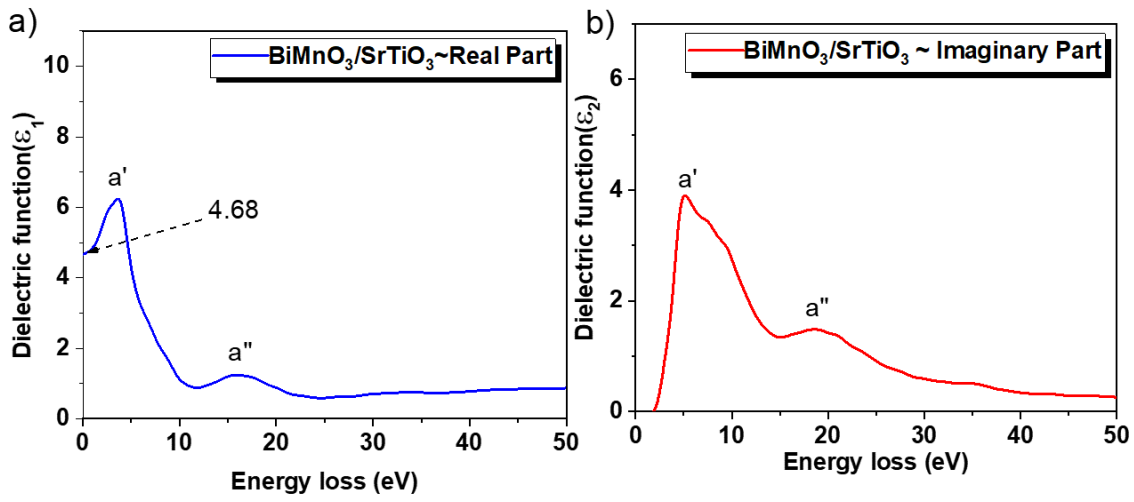

Figure 4.15. Plot of the constants of the complex dielectric function. a) real part and b) imaginary part.

Figure 4.15. a) shows a plot of the real part and b) imaginary part of the complex dielectric function ε^* (E) = ε'(E) + ε''(E) of $BiMnO_3$, from calculations using the KKA function [127]. As it can be seen in a), for E=0 eV, $\varepsilon^* = 4.68$, the static dielectric [128], identified by the real part of the dielectric constant. Moreover, a high peak at a′ = 6.24 eV and a lower peak at a′′= 18.43 though, the value of the dielectric constant at the zero energy is approximately a square of the index (n_{BiMnO_3}= 2.18). It is noteworthy that there is no report on the complex dielectric function and static dielectric constant for $BiMnO_3$. Figure b) shows two peaks, one peak at a′ = 5.31 eV and a second peak at a′′ = 18.35 eV, with onset at 1.63 eV, which is directly associated with its bandgap [129]. These two signals show typical semiconductor material behavior.

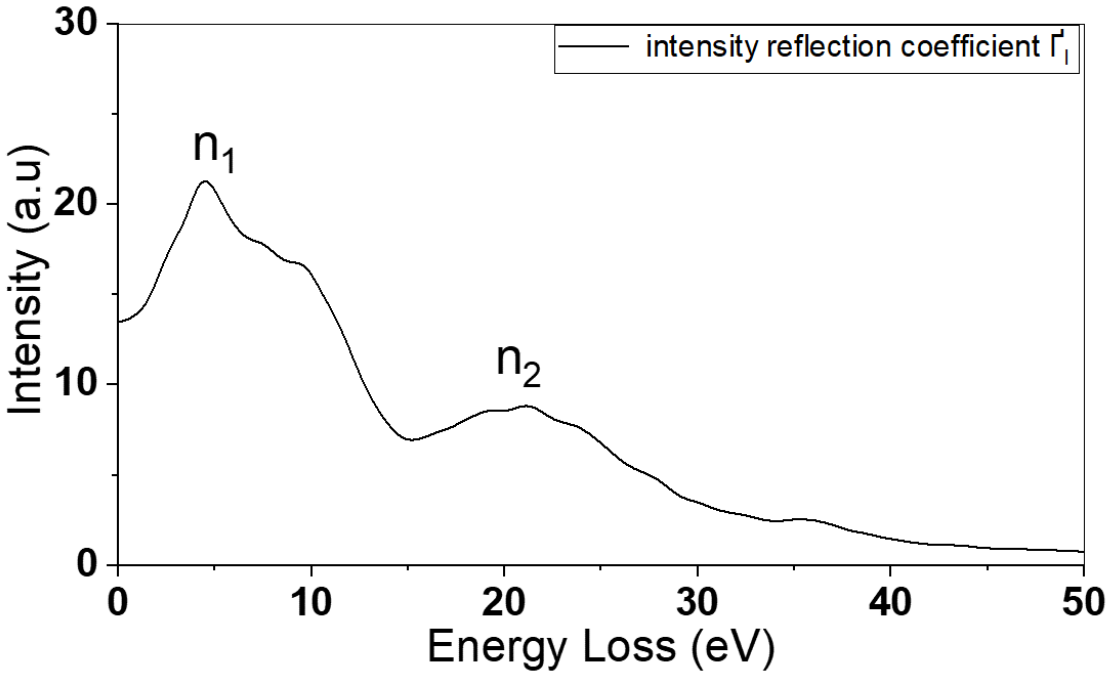

Figure 4.16. Intensity reflection coefficient of $BiMnO_3$.

Figure 4.16 shows the intensity optical reflection coefficient Γ_l of pure phase $BiMnO_3$. The optical reflection coefficient is defined as the ratio of the reflected wave to the incident optical wave. Similarly, Γ_l of dielectric material is related to the reflection of light. Reflection of light usually occurs whenever light travels from one medium of a given refractive index to another [130]. The intensity of reflected light from $BiMnO_3$ vs the energy loss by the wave is such that the light reflection can be (calculated from equation 9). It is related to the outcome of the two media marked as n_1 *and* n_2. for $BiMnO_3$ interchange with normal incidence, the reflection loss is 0.41%. This method used to obtain the optical properties of $BiMnO_3$, is recommended for a polycrystalline thin film.

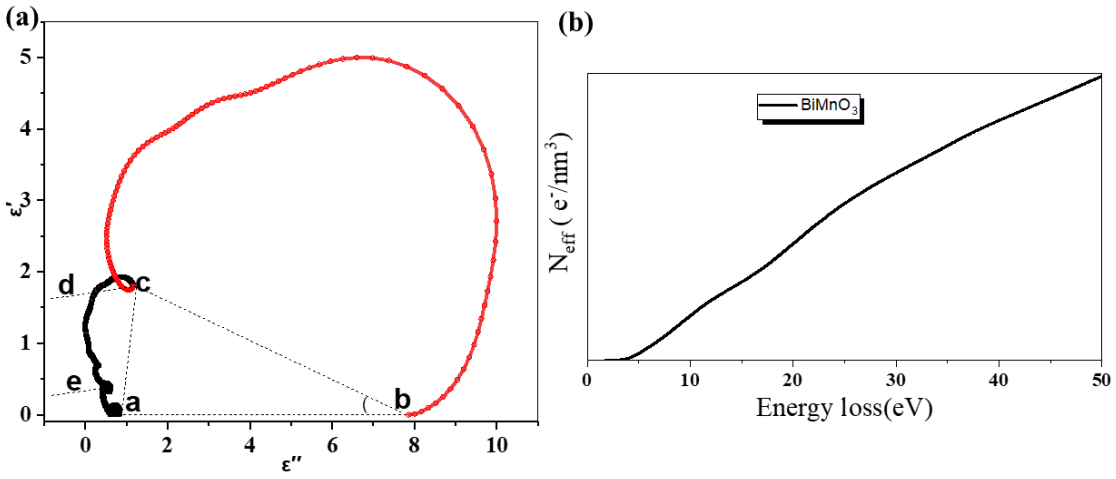

Figure 4.17 a) Cole-Cole plot with an intertwined semi-circle lying directly to the real part of the dielectric constant. b) Calculated total effective number, *Neff (E)* of electrons contribution in the inter-band transitions of $BiMnO_3$.

A plot related to the complex dielectric function of $BiMnO_3$ which was calculated using the CC model. In this sense, is displayed in figure. 4.17 a). It illustrates the relationship

between the real ε′ and imaginary part ε″ component of the dielectric function with positive values. The plot exhibits an intertwined semi-circle lying directly to the real part of the complex dielectric function, which allows for the identification of two principal electronic components. The black bold line joining ∢ a to ∢ c could be attributed to the plasmon region and the second with red dotted chain joining ∢ b and ∢ <c component could be attributed to the bandgap [131]. The semi curve corresponding to the bandgap appears to have two noticeably intertwined patterns, this explicitly differentiates the highest occupied energy state of the valence band and the lowest vacant state of the conduction band in polycrystalline monoclinic-type C_2 $BiMnO_3$, which is the bandgap. The ∢ a, ∢b, *and* ∢c form a right-angled triangle, which can be utilized in the possibility of calculating the area, height, and perimeter of the triangle, thus allowing the description of the spectral shape of the CC model.

("d" and "e" are the intertwined layer). In the optical domain (10^{14}–10^{17} Hz), the CC plot is used to monitor the electronic contributions (inter-band transitions and plasmons) [131]. It is worth noting that limited data are available on polycrystalline monoclinic-type C_2 $BiMnO_3$. Hence, this work is of high importance in terms of the method applied here to determine the optical properties, such as the complex dielectric function, static dielectric function, and reflection coefficient in $BiMnO_3$. The advantage of this method is that no information on the morphology of the sample is needed and is a stand-alone technique. This means that it is possible to obtain the optical properties of any surface polycrystalline thin film by using the VEELS-TEM analysis technique together with the KKA and the CC model.

Figure 4.17 (b) illustrates the calculated total effective number, *Neff (E)* of electrons contribution in the inter-band transitions. The obtained calculated image was obtained by using the Gatan Microscopy Suite software. From physical observation, the *Neff (E)*

increases with an increase in energy. As the *Neff (E)* increased gradually, starting from the bandgap region and slops at 18 eV and a high step is found at 30ev the *Neff (E)*, then increases in energy to the peak at 50 eV. This confirms that no saturation value was observed in the plot [131].

4.7. Electrical resistivity measurement

Electrical resistivity (ρ in Ohm-m), measures how much a $BiMnO_3$ film resists the flow of electricity. It is related to electrical conductivity (σ in Siemens/m) by a simple inverse relationship: $\sigma = 1/\rho$.

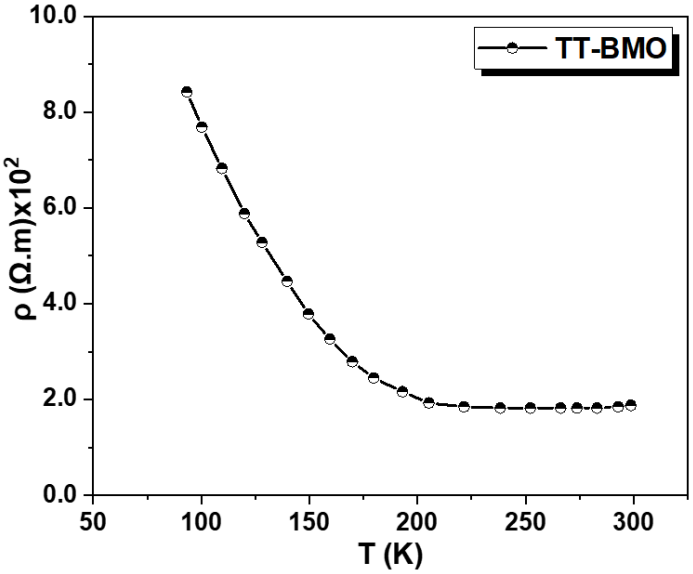

Figure 4.18. Temperature dependent resistivity curve for TT-BMO thin film (ρ–T curve).

The electrical resistivity Figure 4.18 displays, TT-BMO as a function of temperature, within a range of 83–300 K at room temperature. Noticeably, the resistivity (ρ) decreases drastically with the increase in temperature (T), showing a typical semiconductor behavior. ρ (T = 300 K) ~ 1.85×10^2 Ω·m and ρ (T = 100 K) ~ 7.71×10^2 Ω·m, similar

to the value reported for an electrical resistivity for a polycrystalline ceramic at room temperature, 2×10^4 Ω·cm [10,36] Hence, TT-BMO sample has ample and profound physical properties that influence the behavior of electrical transport sample.

4.8 Electrical and magnetic characterization

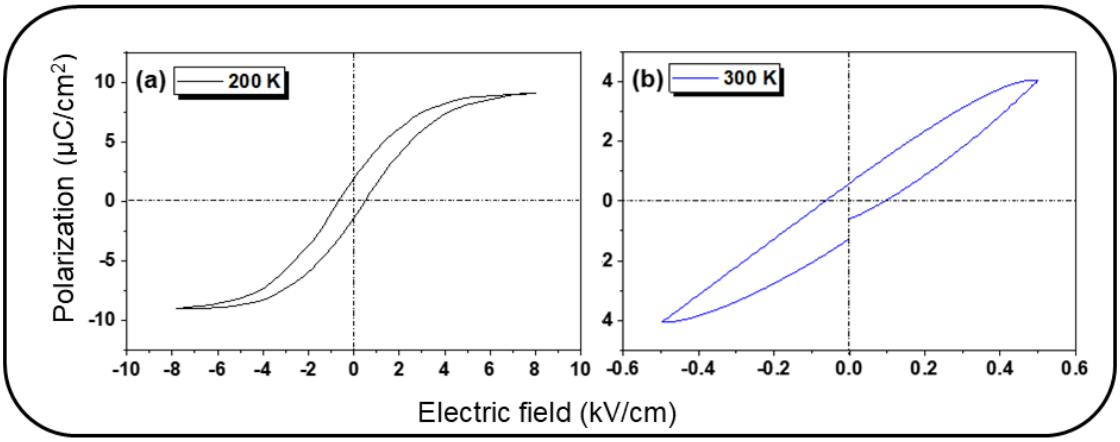

Figure 4.19. The *P–E* hysteresis loops of $BiMnO_3$ samples at a) 200 K, b) 300 K, c) *M-T* curve of the $BiMnO_3$ thin film. The inset shows d*M*/d*T* plot for accurate measurement of *T*C.

Ferroelectric hysteresis loops of the $BiMnO_3$ at 200 K and 300 K are shown in Figure 4.19 a) and b). The Figures establish the ferroelectric behaviour of the $BiMnO_3$ displaying saturated and unsaturated hysteresis loops respectively. Both samples show distinct hysteresis characteristics due to the different temperature of measurment for the samples. The room temperature $BiMnO_3$ shows a leakage current while at 200 K it indicates typical ferroelectric hysteresis loop as shown in table 4 a), under an applied electric field of 15 kV/cm. A saturated loop was obtained at 300 K, likewise the report of M. Grizalez *at al.* [8]. It is difficult to have good measurements of ferroelectric in perovskite materials at a

temperatures higher than 300 K and below 100 K [132,133]. We suggest that this behavior may be due to change in the structural orientation of the film. The temperature dependence of the magnetization of the TT-BMO thin film study in Figure 4.19 c), exist a progressive increase of magnetization with reducing temperature from ~50 to 10 K. This is a clear signature of FM ordering in the sample. The FM is related to superexchange interactions of the Mn^{3+} ions and in a smaller amount to double exchange interactions between Mn^{3+} and Mn^{4+} ions. The linear trend in the range 200 to ~50 K represents short-range magnetic interactions above the inflection point. This region usually appears with a zero net magnetic moment; hence the non-vanishing magnetization is a signature of strong short-range magnetic interactions in the $BiMnO_3$ thin films. The inset in Figure. 9 shows the derivative of the *M-T* plot to accurately measure T_C. The obtained value of T_C is ~ 37 K, lower than the bulk form, which is around 105 K [10,47,134]. This can be attributed to the grain size of the film and the existence of oxygen non-stoichiometry [135–138]. Samples with small grain sizes are expected to have low curie temperature Tc [136]. This may be the case for the $BiMnO_3$ sample.

4.9. Mechanical characterization

The mechanical properties of $BiMnO_3$ thin film are characterized with

nanoindentation measurements. This has led to a deep understanding of the microscopic processes responsible for the mechanical behavior of this materials.

Figure 4.20 displays a characteristic load-depth penetration curve of an single crystal $BiMnO_3$ Thin film with the maximum penetration load of 0.7 mN and the loading/unloading rate of 0.58 mN/s. A frist single sudden discontinuity (Frist, pop-in) in

the load–displacement curve was observed at a specific depth (14–40 nm) of the $BiMnO_3$ thin film.

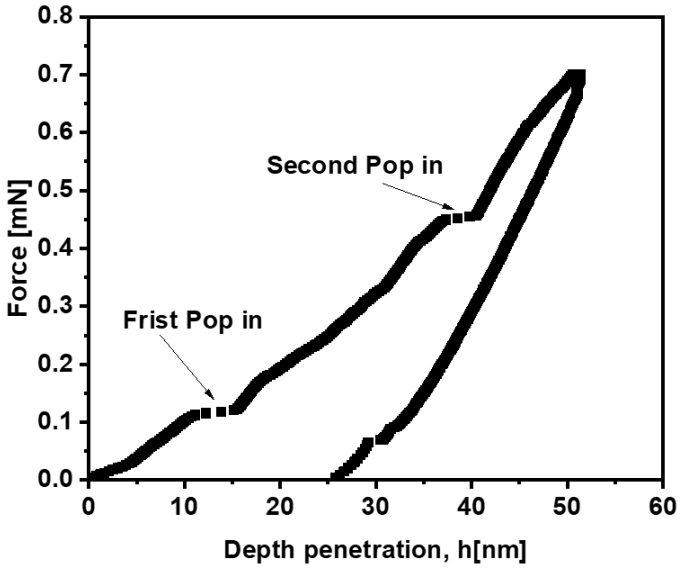

Figure 4.20. *P–h* curves of the first and second pop-in events for $BiMnO_3$ single crystal in the thin film, at nanometer scales.

The physical mechanism responsible for the 'pop-in' event in this thin film may be due to the interaction behavior of the threading dislocations during the mechanical deformation. On the other hand, the second pop-in is normally attributed to failure of the material due to fractures [139,140], or in the case of coatings on a substrate it could be the failure due to adhesion between the substrate and the film, this is clarified later in the simulation part. In other word, the elasto-plastic transition is clearly observed by a sudden penetration effect called pop-in. This sliding effect is related to the onset of permanent or plastic deformation due to the origin of the dislocations. This pop-in is characteristic of each material where it is directly related to the yield point [141,142]. Static indentation hardness tests usually imply the application of load to a spherical or pyramidal indenter. Experiments show that hardness between the indenter and the sample is directly proportional to the material's yield, and can be expressed as; $H \approx CY$, where Y is the yield,

or flow stress, of the material and *C* is called the "constraint factor," the value of which depends upon the type of sample and indenter geometry. Invoking the Tresca shear stress criterion, gives: $H = Y(1 + \alpha)$, (taken $\alpha = 70°$ to Berkovich indenter), therefore $C = (1 + \alpha)$ and with the von Mises criterion gives $C \approx 3$ [142,143]. Therefore, the yield point value for the monoclinic $BiMnO_3$ films is $Y = 2.6 \pm 0.7$ GPa. According to the Oliver-Pharr method [144], stiffness, hardness, and elastic modulus measured for the $BiMnO_3$ Thin films were, S = 44072 ± 45 N/m, H= 8 ± 0.2GPa and E= 142 ± 3GPa respectively. The mechanical properties is presented in the table 4 b). The thin film was subjected to an elastoplastic deformation.

Table 4. a) Ferroelectrics and b) nano-mechanical properties of $BiMnO_3$ Thin film.

(a) Ferroelectrics properties				(b) Nano-mechanical properties				
Temp. (K)	Ps (μC/cm^2)	Pr (μC/cm^2)	Hc (kV/cm)	h_{max} (nm)	Stiffness, S[N/m]	Young modulus, E [GPa]	Hardness, H [GPa]	Yield Strength, Y
200	9.14	2.23	0.77	48 ±0.2	44072 ± 45	142 ± 3	8 ± 0.2	2.6 ± 0.7
300	4.06	0.62	0.10					

Thus, part of the total energy involved in the nanoindentation test is recovered as elastic energy, while the other part associated with the plastic deformation of the material during the indentation is dissipated as plastic energy. The area below each of the loading curves (total energy applied) and unloading curves (elastic energy) it is possible to determine the percentage of plastic energy dissipated for the sample [145–147]. Moreover, another way to visualize the interval of the ferroelastic behavior is through the load penetration curve

of Figure 4.20. In this curve the first elastic behavior delimited by the first penetration values and the yield limit Y, which is the ferroelastic behavior where the redirection of domains, either by the direct or indirect effect as some other authors have visualized [148,149]. So, it is important to visualize this ferroelastic behavior to see the performance of the piezoelectricity in a indirect way. In this case, the ferroelastic range for the $BiMnO_3$ material in thin film form is between 0 to 12 nm, of the curve depth penetration delimited by the yield strength, Y=2.6 ± 0.7 GPa.

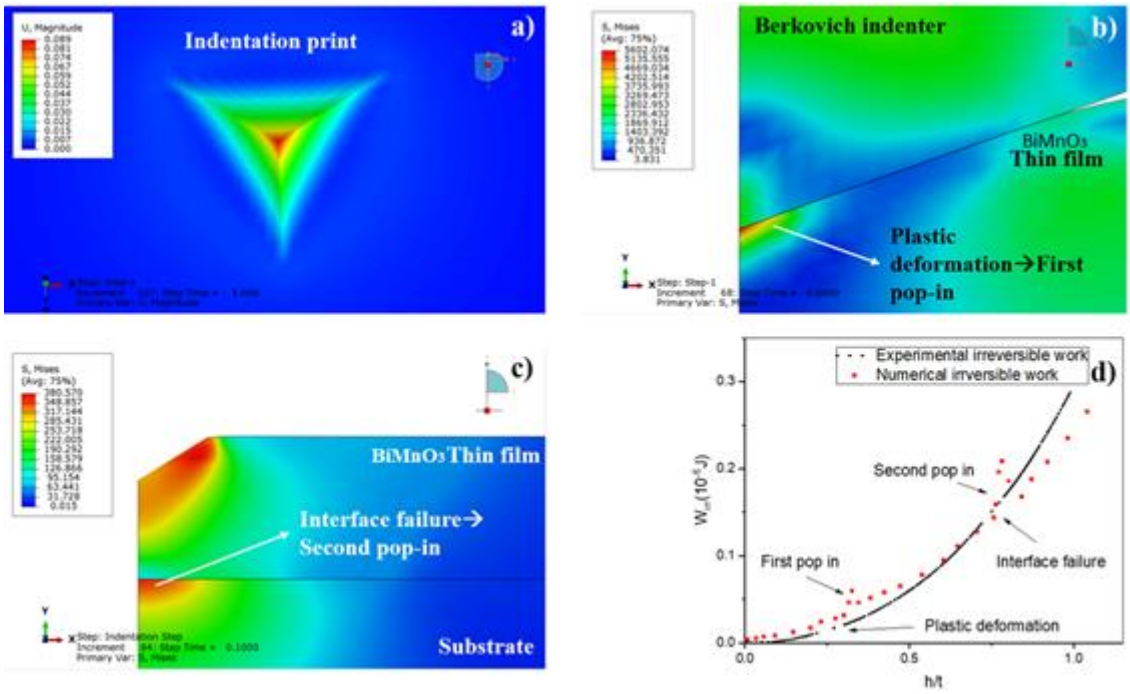

Figure 4.21. Modeling nanomechanical properties in $BiMnO_3$ thin film; a) residual Bercovich area, b) and c) von-Mises stress distribution of $BiMnO_3$ thin film at first and second pop-ins respectively and c) Total energy versus displacement.

Regarding the simulation of the mechanical properties by finite element, as shown in Figure 5, where the different behaviors of von Mises stress distribution at different depths of penetration in the $BiMnO_3$ film are clearly observed. Figure 5a) demonstrates the

Berkovich-type residual area image, which was modeled by finite element, using the experimental load-displacement curve. This Figure shows that there is no crack around this residual area as in other report in similar material [139,140]. So we can say that the second pop-in of the mechanical load-pretraction behavior of Figure 4.20, does not correspond to facture in the $BiMnO_3$ thin film, but to the failure of the interaction between the $BiMnO_3$ film and the $SrTiO_3$ single crystal substrate or abrupt change from passing to the substrate, called an interfere filere. In the Figure b) is display the von Mises beneath of the first pop-in where propagation to the deformation plate has already started by means of the dislocations or twins in the $BiMnO_3$ thin film. On the other hand, Figure 5 c) illustrates the von Misess stress maps of the second pop-in, which corresponds to the failure mentioned above due to the delamination between the $BiMnO_3$ film and the $SrTiO_3$ substrate. Figure 5d) shows the curve of irreversible energy involved (W_{irre}) versus displacement or depth of penetration normalized with the thickness of the thin film (h/t).

5. Cu-doped $BiMnO_3$ on Pt-buffered Si (001)

This section shows the magnetic results obtained from the study of Cu-doped $BiMnO_3$ thin films. First-principles calculations of the electronic structure were carried out using density functional theory (DFT), with the Vienna Ab Initio Simulation Package (VASP). We observed that Cu-dopant and Mn atoms couple antiferromagnetically, causing a reduced magnetic moment, in agreement with the experimental measurements of magnetic hysteresis loops.

5.1. Computational methods

First principles calculations of the electronic structure were carried out using Density Functional Theory (DFT), using the Vienna Ab Initio Simulation Package (VASP) [150–152]. The electronic structure has been calculated using the projector-augmented-wave

(PAW) method [153,154], within the GGA exchange–correlation energy in the Perdew–Burke–Ernzerh of (PBE) approach [155], and a local Hubbard-U (GGA + U) was also added to the transition metal atom (Mn) to give accurate results for strongly correlated systems. In this work, we used U = 3.5 eV and J = 0 [156]. The starting point was the monoclinic structure of $BiMnO_3$, symmetry space group *C*2 with the experimental lattice constants *a* = 9.5262 Å, *b* = 5.6029 Å, and *c* = 9.8453 Å; α = 90°, β = 110.634° and γ = 90°, reported elsewhere [40]. We used the primitive cell with 40 nonequivalent atoms, 8 Bi, 8 Mn, and 24 O. Next, we created three supercells of 1×2×1, 2×2×1, and 2×2×2, to generate the Mn-doped structures: $BiMn_{0.94}Cu_{0.06}O_3$, $BiMn_{0.97}Cu_{0.03}O_3$, and $BiMn_{0.984}Cu_{0.016}O_3$, with 80, 160 and 320 non-equivalent atoms, respectively. These structures are close enough to the experimental doped structures studied, without the need to generate supercells with a large number of atoms and with considerable computer time-savings. Next, one Mn atom was substituted by a Cu atom in each one of the supercells, generating doped structures with the formula $BiMn_{1-\delta}Cu_{\delta}O_3$, with values δ = 0.06, 0.03 and 0.016 for 1×2×1, 2×2×1, and 2×2×2 supercells, respectively. The structures were fully optimized until the Hellmann−Feynman forces became negligible. Finally, a self-consistent field calculation was carried out for the pure and three doped structures, and it was considered to be achieved when the total energy variation from iteration to iteration did not exceed 10^{-8} eV, on a mesh containing 366, 108, 16 and 5 k-points in the irreducible Brillouin zone (IBZ).

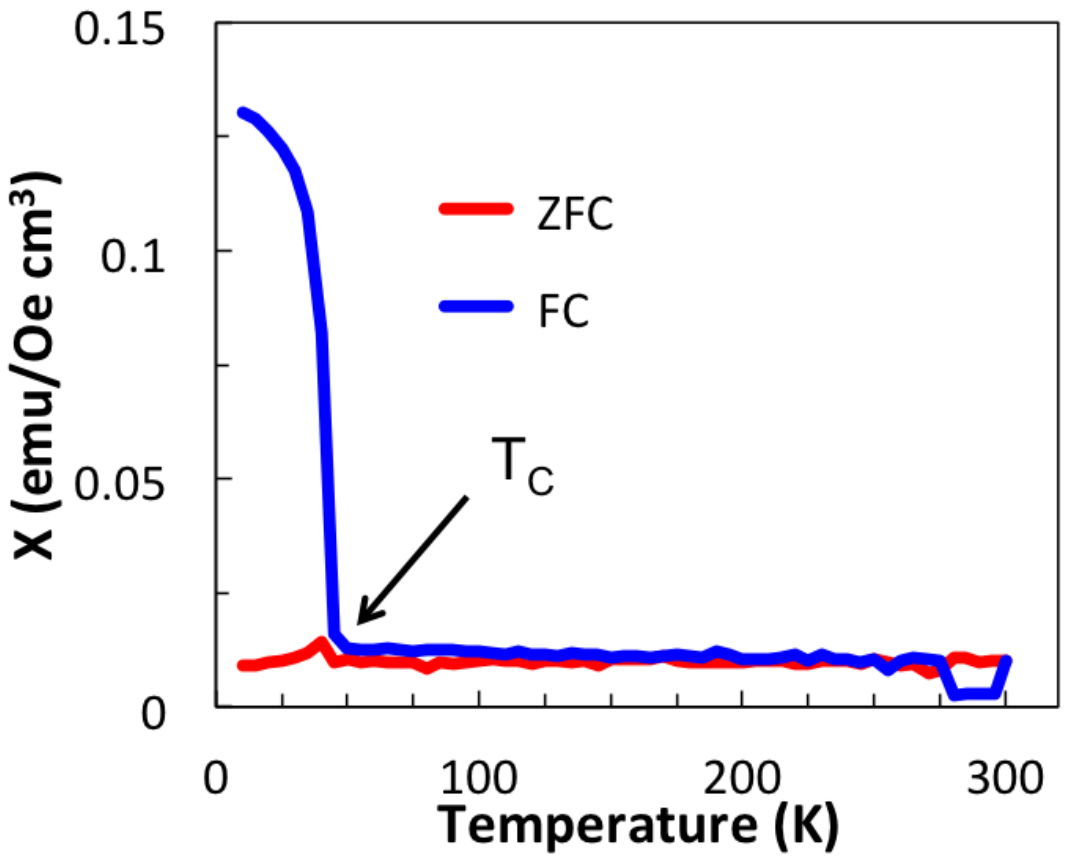

Figure 5.1. Behavior of χ(T) in the range of 2-300 K using a magnetic field of 100 Oe for pure $MnBiO_3$ thin film. The ZFC curve shows a clear ferromagnetic transition temperature at 45 K. While the FC curve shows an antiferromagnetic transition at 40 K.

The first step was the magnetic characterization of the $BiMnO_3$ thin film. Magnetic susceptibility, χ-T, was measured following the ZFC and FC protocols with an applied magnetic field of 100 Oe from 2 to 300 K, see Figure 5.1. The FC curve shows a FM transition around 45 K, which is attributed to the T_C, higher than 10 K as reported in [157]. Below this temperature, the magnetization increases rapidly. Moreover, the ZFC curve shows a maximum value at 40 K, the highest value is a characteristic of the blocking temperature associated with the crystallite size. This behavior was reported in $BiMnO_3$ nanoparticles [14]. To confirm the presence of the two magnetic orders. Similarly, Figure

5.2 a) displays the magnetization measurements of the pure thin film of $BiMnO_3$ as a function of the magnetic field at different temperatures. At the lowest temperature (10 K, in black curve), hysteresis loop is seen as deployed in Figure 5.2 b), the magnetization of the sample saturates at 3000 Oe, M_r = 14.17 emu/cm^3.

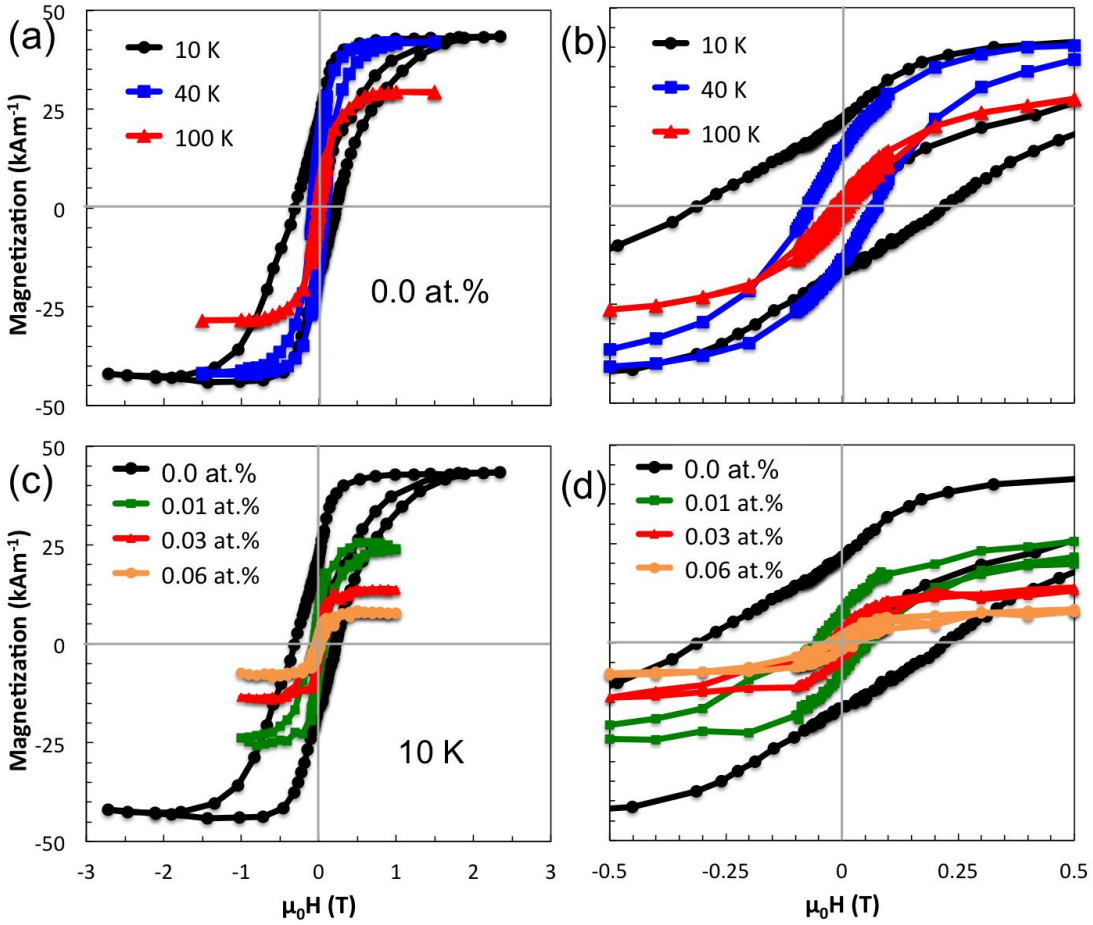

Figure 5.2 a) Magnetic behavior of pure $MnBiO_3$ thin film at 10K, 40K and 100K. At 100 K. b) Zoom image of Figure 5.2 a), c) Comparative of hysteresis loops of pure and Cu-doped $BiMnO_3$ thin films at 10 K. d) Zoom image of Figure 5. c) showing the behavior at low applied magnetic fields.

Figure 5.2 c) displays the M-H curves for $BiMnO_3$ and Cu-doped $BiMnO_3$ thin films at 10 K. The presence of copper atoms does not contribute to the ferromagnetism observed

in the $BiMnO_3$ sample, but decreases the magnetic properties of the material. At low applied magnetic fields, the raise in magnetization values is negligible, but hysteresis is observed. Figure 5.2 d) is the zoom of Figure 5.2 c). The curves for Cu-doped $BiMnO_3$ did not intercept on the Y-axis, making it impossible to determine coercivity (H_C), but (M_r) values were obtained to be 8.13 emu/cm^3, 3.60 emu/cm^3, and 1.76 emu/cm^3 for $BiMn_{0.984}Cu_{0.016}O_3$, $BiMn_{0.97}Cu_{0.03}O_3$ and $BiMn_{0.94}Cu_{0.06}O_3$ respectively. At high applied magnetic field, the diamagnetic contribution appears at low temperature and decreases as the amount of copper increases.

5.2. Theoretical analysis

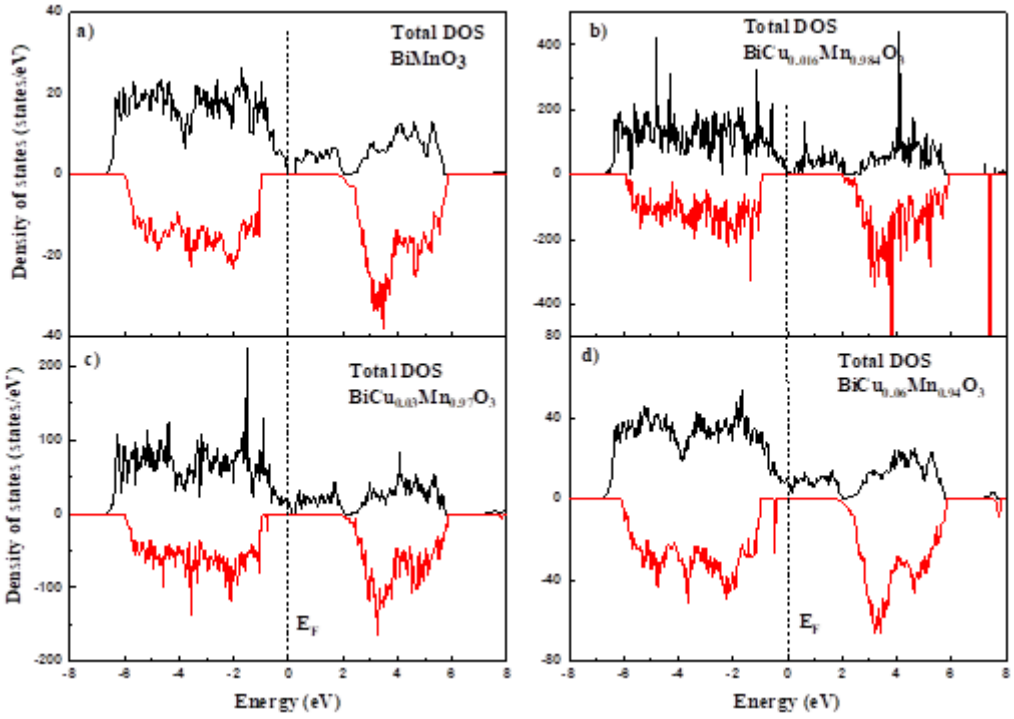

Figure 5.3 Total density of states for pure $BiMnO_3$, $BiMn_{0.984}Cu_{0.016}O_3$, $BiMn_{0.97}Cu_{0.03}O_3$ and $BiMn_{0.94}Cu_{0.06}O_3$.

Figure 5.3. shows the total density of states of the four structures, showing the spin-up and spin-down contributions. The electron distribution with spin-up and spin-down, exhibits an asymmetry, giving rise to a ferromagnetic order in four structures. However,

doping with Cu atoms causes a decrease in the net magnetic moment, given that Cu couples antiferromagnetically with Mn, in agreement with our experimental results. The magnetic moment is due almost entirely by Mn and Cu atoms, as Bi and O do not produce an appreciable contribution. The magnetic moments arise, mainly, from Mn- and Cu-*d* orbitals, as can be seen in Figure 5.4.

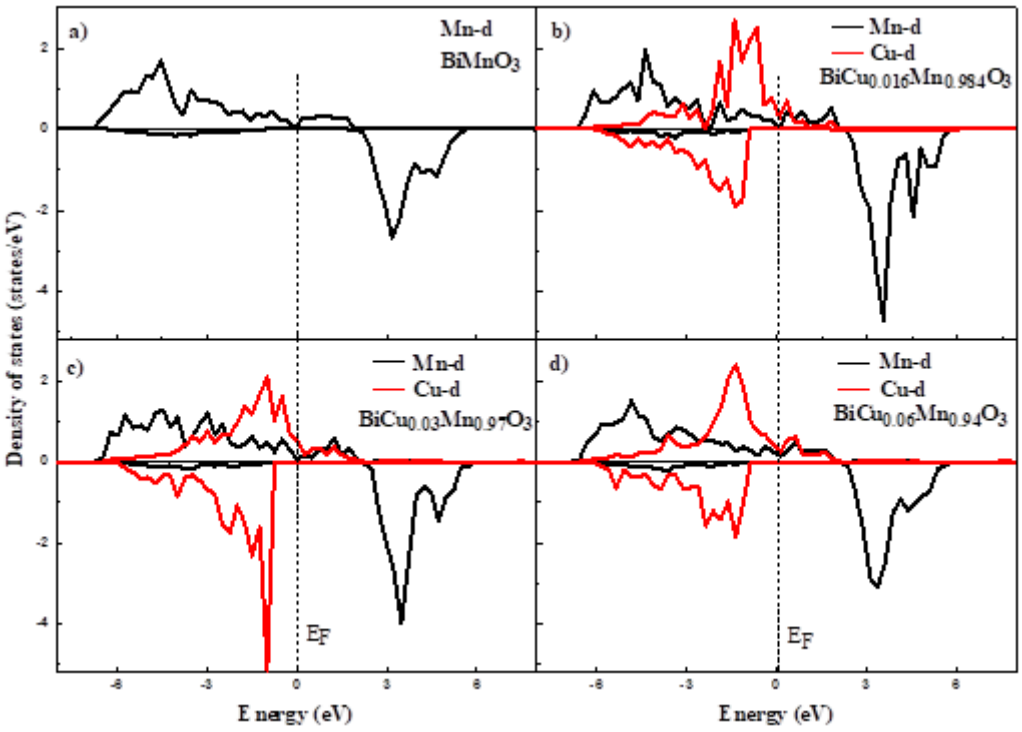

Figure. 5.4. Partial density of states for $BiMnO_3$, $BiMn_{0.984}Cu_{0.016}O_3$, $BiMn_{0.97}Cu_{0.03}O_3$ and $BiMn_{0.94}Cu_{0.06}O_3$ for Mn and Cu d-states.

Table 5. Summary of the magnetic properties for $BiMnO_3$, $BiMn_{0.984}Cu_{0.016}O_3$, $BiMn_{0.97}Cu_{0.03}O_3$ and $BiMn_{0.94}Cu_{0.06}O_3$

	Magnetic moment/atom (μ_B)	Magnetic moment/cell (μ_B)	Magnetization (emu/g)
$BiMnO_3$	Mn: 3.9	31.0	69.4
$BiMn_{0.984}Cu_{0.016}O_3$	Mn: 3.9 Cu: -0.6	242.3	67.2
$BiMn_{0.97}Cu_{0.03}O_3$	Mn: 3.9 Cu: -0.6	118.3	66.2
$BiMn_{0.94}Cu_{0.06}O_3$	Mn: 3.9 Cu: -0.6	56.3	62.9

Furthermore, from the total density of states, we can see an interesting result concerning the electrical properties. The $BiMnO_3$ is a semiconductor of narrow band gap, E_g = 1.22 eV and this gap decreases as Cu concentration increases in $BiMn_{0.984}Cu_{0.016}O_3$ and $BiMn_{0.97}Cu_{0.03}O_3$, until it becomes a conductor for $BiMn_{0.94}Cu_{0.06}O_3$.

6. CONCLUSIONS

$BiMnO_3$ thin films were successfully grown via RF magnetron sputtering technique on three different substrates, namely Si (001), Pt-buffered Si (001), Nb-doped $SrTiO_3$ (100), and also doped with different amounts of Cu, with an optimum condition of base pressure 6.7×10^{-6} Pa, RF power source (13.56 MHz) at 60 W growth temperature of 600 ± 5 °C. A rotating speed of 3 RPM, an Ar flow rate of 13 SCCM, a target distance of 16 cm from the substrate holder to the 1" magnetron, and a working pressure of 4.0×10^{-1} Pa. Powder X-ray diffraction is a powerful tool in the identification and characterization of $BiMnO_3$ thin film structure, in collaboration with Raman analysis, a monoclinic phase with the *C*2 space group was confirmed. EDS revealed the homogeneous distribution of each element of Bi, Mn, and O in $BiMnO_3$ thin films, proven by the XPS analysis and the existence of Mn charge transition of 3+ and 4+ states. A clear interface between the thin film and substrate was observed in the HRTEM results. The existence of strong ferroelectricity in the $BiMnO_3$ thin film showed saturation polarization of 9.14 $\mu C/cm^2$ at 200 K. Resistivity result describes $BiMnO_3$ to possess a semiconductor behavior. Magnetic measurements for $BiMnO_3$ thin film showed a ferromagnetic behavior with Curie temperature of 37 K and strong short-range magnetic interactions. The optical property of $BiMnO_3$ have not been extensively investigated, this work has opened a new window for studying the optical properties of $BiMnO_3$ multiferroic materials through VEELS-TEM analysis, indicating that $BiMnO_3$ could be relevant to the application of ferroelectric films to in photovoltaic and optical devices. The pop-in characteristics and mechanical properties of $BiMnO_3$ were systematically studied by Oliver and Pharr method in nanoindentation. The nanomechanical properties evaluated, such as: elastic modulus, hardness, and stiffness, with obtained values of S =44072 ± 45 N/m, E=142 ± 3GPa, and H=8 ± 0.2GPa respectively. Values deduced from the mechanical and ferroelectric measurement of

$BiMnO_3$ thin film revealed that $BiMnO_3$ thin films are attractive materials for energy harvesting, spintronics, spin valve, sensor applications, and microelectromechanical systems devices. The investigation on the effects of Cu on the structure and magnetic properties of pure $BiMnO_3$, and three Cu-doped samples: $BiMn_{0.984}Cu_{0.016}O_3$, $BiMn_{0.97}Cu_{0.03}O_3$, and $BiMn_{0.94}Cu_{0.06}O_3$, obtained via RF magnetron sputtering, resulted that $BiMnO_3$ with an appropriate amount of doped Cu will have good application prospects in spintronic photo-sensing devices.

❖

7. REFERENCES

[1] B. Sun, C.M. Li, Light-controlled resistive switching memory of multiferroic BiMnO3 nanowire arrays, Phys. Chem. Chem. Phys. 17 (2015) 6718–6721. https://doi.org/10.1039/C4CP04901B.

[2] D. Karoblis, A. Zarkov, K. Mazeika, D. Baltrunas, G. Niaura, A. Beganskiene, A. Kareiva, Sol-gel synthesis, structural, morphological and magnetic properties of $BaTiO_3$–$BiMnO_3$ solid solutions, Ceram. Int. 46 (2020) 16459–16464. https://doi.org/10.1016/j.ceramint.2020.03.209.

[3] W. Ren, J. Li, G. Liu, J. Chen, S. Chen, Z. Gu, J. Li, J. Li, Y. Gao, Design and Optimization of a BAW Magnetic Sensor Based on Magnetoelectric Coupling, Micromachines. 13 (2022) 206. https://doi.org/10.3390/mi13020206.

[4] S. Malley, S. Newacheck, G. Youssef, Additively manufactured multifunctional materials with magnetoelectric properties, Addit. Manuf. 47 (2021) 102239. https://doi.org/10.1016/j.addma.2021.102239.

[5] S.I. Shkuratov, C.S. Lynch, A review of ferroelectric materials for high power devices, J. Mater. (2022). https://doi.org/10.1016/j.jmat.2022.04.002.

[6] T. Chady, R.D. Łukaszuk, K. Gorący, M.J. Żwir, Magnetic Recording Method (MRM) for Nondestructive Evaluation of Ferromagnetic Materials, Materials (Basel). 15 (2022) 630. https://doi.org/10.3390/ma15020630.

[7] J.Y. Son, Y.S. Shin, Y.H. Shin, Multiferroic properties of self-aligned BiMnO 3 nanosquares, in: J. Am. Ceram. Soc., 2012: pp. 2474–2477.

https://doi.org/10.1111/j.1551-2916.2012.05308.x.

[8] M. Grizalez, G.A. Mendoza, P. Prieto, Analysis of multiferroic properties in $BiMnO_3$ thin films, in: J. Phys. Conf. Ser., Institute of Physics Publishing, 2009. https://doi.org/10.1088/1742-6596/167/1/012035.

[9] E.M. Choi, A. Kursumovic, O.J. Lee, J.E. Kleibeuker, A. Chen, W. Zhang, H. Wang, J.L. Macmanus-Driscoll, Ferroelectric Sm-doped $BiMnO_3$ thin films with ferromagnetic transition temperature enhanced to 140 K, ACS Appl. Mater. Interfaces. 6 (2014) 14836–14843. https://doi.org/10.1021/am501351c.

[10] B.W. Lee, P.S. Yoo, V.B. Nam, K.R.N. Toreh, C.U. Jung, Magnetic and electric properties of stoichiometric $BiMnO_3$ thin films, Nanoscale Res. Lett. 10 (2015). https://doi.org/10.1186/S11671-015-0759-9.

[11] N.A. Hill, Why are there so few magnetic ferroelectrics?, J. Phys. Chem. B. 104 (2000) 6694–6709. https://doi.org/10.1021/jp000114x.

[12] Z. Branković, Z.M. Stanojević, L. Mančić, V. Vukotić, S. Bernik, G. Branković, Multiferroic bismuth manganite prepared by mechanochemical synthesis, J. Eur. Ceram. Soc. 30 (2010) 277–281. https://doi.org/10.1016/j.jeurceramsoc.2009.06.030.

[13] A.A. Belik, S. Iikubo, T. Yokosawa, K. Kodama, N. Igawa, S. Shamoto, M. Azuma, M. Takano, K. Kimoto, Y. Matsui, E. Takayama-Muromachi, Origin of the monoclinic-to-monoclinic phase transition and evidence for the centrosymmetric crystal structure of $BiMnO_3$, J. Am. Chem. Soc. 129 (2007) 971–977. https://doi.org/10.1021/ja0664032.

[14] S.A. Acharya, V.M. Gaikwad, S.K. Kulkarni, U.P. Despande, Low pressure synthesis of $BiMnO_3$ nanoparticles: anomalous structural and magnetic features, J. Mater. Sci. 52 (2017) 458–466. https://doi.org/10.1007/s10853-016-0345-2.

[15] C.C. Chou, C.L. Huang, S. Mukherjee, Q.Y. Chen, H. Sakurai, A.A. Belik, E. Takayama-Muromachi, H.D. Yang, Multiple magnetic transitions in multiferroic $BiMnO_3$, Phys. Rev. B - Condens. Matter Mater. Phys. 80 (2009). https://doi.org/10.1103/PhysRevB.80.184426.

[16] H.W. Shin, J.Y. Son, Enhanced multiferroic properties of tetragonally strained epitaxial $BiMnO_3$ thin films grown on single crystal Rh substrates, Solid State Sci. 91 (2019) 7–9. https://doi.org/10.1016/j.solidstatesciences.2019.03.003.

[17] A.A. Belik, Y. Matsushita, M. Tanaka, E. Takayama-Muromachi, Low-temperature vacuum reduction of $BiMnO_3$, Inorg. Chem. 50 (2011) 7685–7689. https://doi.org/10.1021/IC2007233.

[18] A.A. Belik, H. Yusa, N. Hirao, Y. Ohishi, E. Takayama-Muromachi, Peculiar high-pressure behavior of $BiMnO_3$, Inorg. Chem. 48 (2009) 1000–1004. https://doi.org/10.1021/ic8015996.

[19] E. Montanari, G. Calestani, L. Righi, E. Gilioli, F. Bolzoni, K.S. Knight, P.G. Radaelli, Structural anomalies at the magnetic transition in centrosymmetric $BiMnO_3$, Phys. Rev. B - Condens. Matter Mater. Phys. 75 (2007). https://doi.org/10.1103/PhysRevB.75.220101.

[20] A. Molak, Z. Ujma, M. Pilch, I. Gruszka, M. Pawelczyk, Resistance switching induced in $BiMnO_3$ ceramics, Ferroelectrics. 464 (2014) 59–71. https://doi.org/10.1080/00150193.2014.892815.

[21] E. Montanari, G. Calestani, A. Migliori, M. Dapiaggi, F. Bolzoni, R. Cabassi, E. Gilioli, High-temperature polymorphism in metastable $BiMnO_3$, Chem. Mater. 17 (2005) 6457–6467. https://doi.org/10.1021/CM051576W.

[22] J.Y. Son, C.S. Park, H. Kim, Room temperature ferroelectric property of $BiMnO_3$ thin film with double $SrTiO_3$ buffer layers on Pt/Ti/SiO2/Si substrate, Met.

Mater. Int. 16 (2010) 289–292. https://doi.org/10.1007/s12540-010-0419-7.

[23] K.S. Pugazhvadivu, L. Balakrishnan, K. Tamilarasan, Structural, magnetic and electrical properties of calcium modified bismuth manganite thin films, Mater. Chem. Phys. 155 (2015) 147–154. https://doi.org/10.1016/j.matchemphys.2015.02.012.

[24] J.H. Lee, X. Ke, R. Misra, J.F. Ihlefeld, X.S. Xu, Z.G. Mei, T. Heeg, M. Roeckerath, J. Schubert, Z.K. Liu, J.L. Musfeldt, P. Schiffer, D.G. Schlom, Adsorption-controlled growth of $BiMnO_3$ films by molecular-beam epitaxy, Appl. Phys. Lett. 96 (2010) 262905. https://doi.org/10.1063/1.3457786.

[25] P. Baettig, R. Seshadri, N.A. Spaldin, Anti-polarity in ideal $BiMnO_3$, J. Am. Chem. Soc. 129 (2007) 9854–9855. https://doi.org/10.1021/ja073415u.

[26] U. Dash, N. V. Raveendra, C.U. Jung, A rigorous investigation of $BiMnO_3$ ferroelectricity through a development of a novel way to stabilize twin free and monoclinic thin film, J. Alloys Compd. 684 (2016) 310–314. https://doi.org/10.1016/j.jallcom.2016.05.150.

[27] J.P. Chakrabartty, R. Nechache, C. Harnagea, F. Rosei, Photovoltaic effect in multiphase Bi-Mn-O thin films, Opt. Express. 22 (2014) A80. https://doi.org/10.1364/oe.22.000a80.

[28] Q. Song, C.A. Occhialini, E. Ergeçen, B. Ilyas, D. Amoroso, P. Barone, J. Kapeghian, K. Watanabe, T. Taniguchi, A.S. Botana, S. Picozzi, N. Gedik, R. Comin, Evidence for a single-layer van der Waals multiferroic, Nat. 2022 6027898. 602 (2022) 601–605. https://doi.org/10.1038/s41586-021-04337-x.

[29] P. Li, X.S. Zhou, Z.X. Guo, Intriguing magnetoelectric effect in two-dimensional ferromagnetic/perovskite oxide ferroelectric heterostructure, Npj Comput. Mater. 8 (2022) 1–7. https://doi.org/10.1038/s41524-022-00706-w.

[30] D. Khomskii, Classifying multiferroics: Mechanisms and effects, Physics (College. Park. Md). 2 (2009) 20. https://doi.org/10.1103/physics.2.20.

[31] M.M. Gomaa, M.H. Sayed, A.M. Abo El-Soud, M. Boshta, The influence of K substitution on the structural, optical and magnetic properties of $LaFeO_3$ perovskites, Solid State Commun. 342 (2022) 114615. https://doi.org/10.1016/j.ssc.2021.114615.

[32] S. Horiuchi, S. Ishibashi, K. Kobayashi, R. Kumai, Coexistence of normal and inverse deuterium isotope effects in a phase-transition sequence of organic ferroelectrics, RSC Adv. 9 (2019) 39662–39673. https://doi.org/10.1039/C9RA06489C.

[33] E.K. Jang, J.W. Woo, I. Yu, Rochelle salt nanocrystals embedded in porous glass, in: IEEE Int. Symp. Appl. Ferroelectr., IEEE, 1994: pp. 210–213. https://doi.org/10.1109/isaf.1994.522340.

[34] K. Xu, H.J. Xiang, Unusual ferroelectricity induced by the Jahn-Teller effect: A case study on lacunar spinel compounds, Phys. Rev. B - Condens. Matter Mater. Phys. 92 (2015) 121112. https://doi.org/10.1103/PHYSREVB.92.121112/FIGURES/4/MEDIUM.

[35] E.M. Choi, J.E. Kleibeuker, J.L. MacManus-Driscoll, Strain-tuned enhancement of ferromagnetic TC to 176 K in Sm-doped $BiMnO_3$ thin films and determination of magnetic phase diagram, Sci. Rep. 7 (2017). https://doi.org/10.1038/srep43799.

[36] S. Hanif, M. Hassan, S. Riaz, S. Atiq, S.S. Hussain, S. Naseem, G. Murtaza, Structural, magnetic, dielectric and bonding properties of $BiMnO_3$ grown by co-precipitation technique, Results Phys. 7 (2017) 3190–3195. https://doi.org/10.1016/j.rinp.2017.08.061.

[37] N. Kumar, A. Sundaresan, On the observation of negative magnetization under zero-field-cooled process, Solid State Commun. 150 (2010) 1162–1164. https://doi.org/10.1016/J.SSC.2010.03.016.

[38] Y. Sun, F. Guo, J. Chen, S. Zhao, Improved ferroelectric and photovoltaic properties of $BiMnO_3$ modified lead-free $K_{0.5}Na_{0.5}NbO_3$ solid-solution films, Appl. Phys. Lett. 111 (2017). https://doi.org/10.1063/1.5006643.

[39] H.W. Shin, J.Y. Son, Enhanced multiferroic properties of tetragonally strained epitaxial $BiMnO_3$ thin films grown on single crystal Rh substrates, Solid State Sci. 91 (2019) 7–9. https://doi.org/10.1016/j.solidstatesciences.2019.03.003.

[40] G. V. Umoh, J.E. Leal-Perez, S.F. Olive-Méndez, J. González-Hernández, F. Mercader-Trejo, R. Herrera-Basurto, O. Auciello, A. Hurtado-Macias, Complex dielectric function, Cole-Cole, and optical properties evaluation in $BiMnO_3$ thin-films by Valence Electron Energy Loss Spectrometry (VEELS) analysis, Ceram. Int. 48 (2022) 22182–22187. https://doi.org/10.1016/j.ceramint.2022.04.212.

[41] H.-B. Zhang, M. Alexe, H.-B. Zhang, M. Alexe, Optoelectronic Functionality of $BiFeO_3$–$SrTiO_3$ Interface, Adv. Electron. Mater. 8 (2022) 2100665. https://doi.org/10.1002/AELM.202100665.

[42] W. Wang, L. Zhang, R. Jing, Q. Hu, D.O. Alikin, V. Ya. Shur, X. Wei, G. Liu, Y. Yan, L. Jin, Enhancement of energy storage performance in lead-free barium titanate-based relaxor ferroelectrics through a synergistic two-step strategy design, Chem. Eng. J. 434 (2022) 134678. https://doi.org/10.1016/J.CEJ.2022.134678.

[43] J. Chakrabartty, C. Harnagea, M. Celikin, F. Rosei, R. Nechache, Improved photovoltaic performance from inorganic perovskite oxide thin films with mixed crystal phases, Nat. Photonics 2018 125. 12 (2018) 271–276.

https://doi.org/10.1038/s41566-018-0137-0.

[44] K. Khan, A.K. Tareen, M. Aslam, R. Wang, Y. Zhang, A. Mahmood, Z. Ouyang, H. Zhang, Z. Guo, Recent developments in emerging two-dimensional materials and their applications, J. Mater. Chem. C. 8 (2020) 387–440. https://doi.org/10.1039/C9TC04187G.

[45] A. Biswas, H. Jeen, G. Singh-Bhalla, P.R. Mickel, K. Voigt, C. Morien, S. Tongay, A.F. Hebard, Growth and characterization of multiferroic $BiMnO_3$ thin films, in: J. Appl. Phys., 2011. https://doi.org/10.1063/1.3561860.

[46] H. Wang, L. Li, J. Huang, X. Gao, X. Sun, D. Zemlyanov, H. Wang, Two-Phase Roomerature Multiferroic Nanocomposite with $BiMnO_3$-Tilted Nanopillars in the Bi_2W1- $xMnxO_6$ Matrix, ACS Appl. Mater. Interfaces. 11 (2019) 26261–26267. https://doi.org/10.1021/ACSAMI.9B06851/ASSET/IMAGES/LARGE/AM-2019-068515_0005.JPEG.

[47] Z.H. Chi, H. Yang, S.M. Feng, F.Y. Li, R.C. Yu, C.Q. Jin, Room-temperature ferroelectric polarization in multiferroic $BiMnO_3$, J. Magn. Magn. Mater. 310 (2007) 358–360. https://doi.org/10.1016/j.jmmm.2006.10.335.

[48] A.S. Eggeman, A. Sundaresan, C.N.R. Rao, P.A. Midgley, The structure of two new non-centrosymmetric phases of oxygen deficient bismuth manganite, J. Mater. Chem. 21 (2011) 15417–15421. https://doi.org/10.1039/c1jm12840j.

[49] Z. Ghorannevis, E. Akbarnejad, M. Ghoranneviss, Effects of various deposition times and RF powers on CdTe thin film growth using magnetron sputtering, J. Theor. Appl. Phys. 10 (2016) 225–231. https://doi.org/10.1007/s40094-016-0219-7.

[50] T. Zhu, D. Luo, A. Wu, T. Tan, H. Guo, P. Xiong, Z. Lin, S. Huang, Q. Chu, Z. Yang, F. Pan, M. Lu, K. Zhang, Y. He, Applying the plasma physical sputtering

process to SRF cavity treatment: Simulation and Experiment Study, Appl. Surf. Sci. 574 (2022) 151575. https://doi.org/10.1016/j.apsusc.2021.151575.

[51] O.K. Simya, T. Vijayaraghavan, B. Subramanian, A.M. Ashok, Effect of RF sputter power on deposition of CZTX (X[dbnd]S, Se) active layer without selenization/sulfurization, for solar cell applications, J. Alloys Compd. 898 (2022) 162838. https://doi.org/10.1016/j.jallcom.2021.162838.

[52] M. Alhabradi, S. Nundy, A. Ghosh, A.A. Tahir, Vertically Aligned CdO-Decked α-Fe_2O_3 Nanorod Arrays by a Radio Frequency Sputtering Method for Enhanced Photocatalytic Applications, ACS Omega. 7 (2022) 28396–28407. https://doi.org/10.1021/acsomega.2c02996.

[53] A. Baptista, F.J.G. Silva, J. Porteiro, J.L. Míguez, G. Pinto, L. Fernandes, On the Physical Vapour Deposition (PVD): Evolution of Magnetron Sputtering Processes for Industrial Applications, in: Procedia Manuf., Elsevier, 2018: pp. 746–757. https://doi.org/10.1016/j.promfg.2018.10.125.

[54] J. Hora, C. Hall, D. Evans, E. Charrault, Inorganic Thin Film Deposition and Application on Organic Polymer Substrates, Adv. Eng. Mater. 20 (2018). https://doi.org/10.1002/adem.201700868.

[55] A. Iglesias-Juez, G.L. Chiarello, G.S. Patience, M.O. Guerrero-Pérez, Experimental methods in chemical engineering: X-ray absorption spectroscopy—XAS, XANES, EXAFS, Can. J. Chem. Eng. 100 (2022) 3–22. https://doi.org/10.1002/CJCE.24291.

[56] S.B.A. Abbas, K.H. Harbbi, Elimination of the broadening in X-ray diffraction lines profile for nanoparticles by using the analysis of diffraction lines method, AIP Conf. Proc. 2386 (2022) 080033. https://doi.org/10.1063/5.0067983.

[57] P.-A.J. Blanche, Bragg's Law, in: F. Guid. to Hologr., 2014.

https://doi.org/10.1117/3.1002325.ch13.

[58] A. Kouchi, M. Tsuge, T. Hama, Y. Oba, S. Okuzumi, S. Sirono, M. Momose, N. Nakatani, K. Furuya, T. Shimonishi, T. Yamazaki, H. Hidaka, Y. Kimura, K. Murata, K. Fujita, S. Nakatsubo, S. Tachibana, N. Watanabe, Transmission Electron Microscopy Study of the Morphology of Ices Composed of H2O, CO2, and CO on Refractory Grains, Astrophys. J. 918 (2021) 45. https://doi.org/10.3847/1538-4357/AC0AE6.

[59] (17) (PDF) SYNTHESIS OF SILVER NANOPARTICLES USING SILK FIBROIN : CHARACTERIZATION AND POTENTIAL ANTIBACTERIAL PROPERTIES, (n.d.). https://www.researchgate.net/publication/341277064_SYNTHESIS_OF_SILVER_NANOPARTICLES_USING_SILK_FIBROIN_CHARACTERIZATION_AND_POTENTIAL_ANTIBACTERIAL_PROPERTIES/Figures?lo=1 (accessed October 13, 2022).

[60] B. Marczewska, K. Marczewski, First glass electrode and its creators F. haber and Z. klemensiewicz - on 100th anniversary, Zeitschrift Fur Phys. Chemie. 224 (2010) 795–799. https://doi.org/10.1524/zpch.2010.5505.

[61] Introduction to SQUID magetometry, (n.d.). http://www.geocities.ws/pranab_muduli/squid.html (accessed October 3, 2022).

[62] U. Santhi, W.K. Ngui, M. Samykano, K. Sudhakar, K. Kadirgama, B. Sangmesh, M.A.R. Kumar, Cobalt nanowires: Advancing into future nanomaterial, in: AIP Conf. Proc., 2019. https://doi.org/10.1063/1.5085949.

[63] H. Zhu, T. Miyashita, M. Mitsuishi, Energy storage behaviors in ferroelectric capacitors fabricated with sub-50 nm poly(vinylidene fluoride) Langmuir–Blodgett nanofilms, Polym. J. 51 (2019) 795–801.

https://doi.org/10.1038/s41428-019-0194-3.

[64] C. Jin, X. Li, W. Han, Q. Liu, S. Hu, Y. Ji, Z. Xu, S. Hu, M. Ye, M. Gu, Y. Zhu, L. Chen, Ferroelectricity and Ferromagnetism Achieved via Adjusting Dimensionality in $BiFeO_3$/$BiMnO_3$ Superlattices, ACS Appl. Mater. Interfaces. 13 (2021) 41315–41322. https://doi.org/10.1021/ACSAMI.1C11120/ASSET/IMAGES/MEDIUM/AM1C11120_M002.GIF.

[65] G. Aviv, SQUIDs-Superconducting Quantum Interference Devices, 84105 (2008).

[66] Q. Kan, W. Yan, G. Kang, Q. Sun, Oliver-Pharr indentation method in determining elastic moduli of shape memory alloys-A phase transformable material, J. Mech. Phys. Solids. 61 (2013) 2015–2033. https://doi.org/10.1016/j.jmps.2013.05.007.

[67] D.R. Katti, K.S. Katti, S. Molla, S. Kar, Biomechanics of cells as potential biomarkers for diseases: A new tool in mechanobiology, in: Encycl. Biomed. Eng., Elsevier, 2019: pp. 1–21. https://doi.org/10.1016/B978-0-12-801238-3.99938-0.

[68] C. Freyman, B. Zhao, Y.W. Chung, Suppression of moisture sensitivity of friction in carbon-based coatings, Superlubricity. (2007) 295–310. https://doi.org/10.1016/B978-044452772-1/50049-4.

[69] Handbook of Mechanics of Materials, Handb. Mech. Mater. (2020). https://doi.org/10.1007/978-981-10-6855-3.

[70] L. Li, J. Wang, X. Pei, W. Chu, A. Cai, A modified elastic contact stiffness model considering the deformation of bulk substrate, J. Mech. Sci. Technol. 2020 342. 34 (2020) 777–790. https://doi.org/10.1007/S12206-020-0126-3.

[71] R.E. Smallman, A.H.W. Ngan, Characterization and Analysis, in: Mod. Phys. Metall., Elsevier, 2014: pp. 159–250. https://doi.org/10.1016/b978-0-08-098204-5.00005-5.

[72] R. Garza-Hernández, S. Lugo-Loredo, F.S. Aguirre-Tostado, The role of copper during the growth of stoichiometric Cu2ZnSnS4 by successive ionic layer adsorption and reaction method, Ceram. Int. 46 (2020) 5185–5192. https://doi.org/10.1016/J.CERAMINT.2019.10.265.

[73] D. Briggs, Handbook of X-ray Photoelectron Spectroscopy C. D. Wanger, W. M. Riggs, L. E. Davis, J. F. Moulder and G. E.Muilenberg Perkin-Elmer Corp., Physical Electronics Division, Eden Prairie, Minnesota, USA, 1979. 190 pp. $195, Surf. Interface Anal. 3 (1981) v–v. https://doi.org/10.1002/SIA.740030412.

[74] M. Stöger-Pollach, A. Laister, P. Schattschneider, Treating retardation effects in valence EELS spectra for Kramers-Kronig analysis, Ultramicroscopy. 108 (2008) 439–444. https://doi.org/10.1016/j.ultramic.2007.07.003.

[75] M. Stöger-Pollach, Optical properties and bandgaps from low loss EELS: Pitfalls and solutions, Micron. 39 (2008) 1092–1110. https://doi.org/10.1016/J.MICRON.2008.01.023.

[76] D. Su, B. Yang, N. Jiang, M. Sawicki, C. Broadbridge, M. Couillard, J.W. Reiner, F.J. Walker, C.H. Ahn, Y. Zhu, Valence electron energy-loss spectroscopy of ultrathin $SrTiO_3$ films grown on silicon (100) single crystal, Appl. Phys. Lett. 96 (2010) 4127. https://doi.org/10.1063/1.3364144.

[77] Annon, Digital Micrograph EELS Analysis User's Guide, U.S.A., 2003.

[78] R.F. Egerton, Electron Energy-Loss Spectroscopy in the Electron Microscope, 1996. https://doi.org/10.1007/978-1-4757-5099-7.

[79] H. Raether, Excitation of Plasmons and Interband Transitions by Electrons,

Springer-Verlag Berlin Heidelberg New York, 1980. https://doi.org/10.1007/bfb0045951.

[80] A.S. Wright, Fresnel's laws, ceteris paribus, Stud. Hist. Philos. Sci. Part A. 64 (2017) 38–52. https://doi.org/10.1016/j.shpsa.2017.07.008.

[81] S.F. Chérif, A. Chérif, W. Dridi, M.F. Zid, Ac conductivity, electric modulus analysis, dielectric behavior and Bond Valence Sum analysis of $Na_3Nb_4As_3O_{19}$ compound, Arab. J. Chem. 13 (2020) 5627–5638. https://doi.org/10.1016/j.arabjc.2020.04.003.

[82] M. Stöger-Pollach, H. Franco, P. Schattschneider, S. Lazar, B. Schaffer, W. Grogger, H.W. Zandbergen, Čerenkov losses: A limit for bandgap determination and Kramers-Kronig analysis, Micron. 37 (2006) 396–402. https://doi.org/10.1016/j.micron.2006.01.001.

[83] L. Qiao, S. Zhang, H.Y. Xiao, D.J. Singh, K.H.L. Zhang, Z.J. Liu, X.T. Zu, S. Li, Orbital controlled band gap engineering of tetragonal $BiFeO_3$ for optoelectronic applications, J. Mater. Chem. C. 6 (2018) 1239–1247. https://doi.org/10.1039/C7TC04160H.

[84] S. Brinckmann, R. Schwaiger, Towards enhanced nanoindentation by image recognition, J. Mater. Res. 36 (2021) 2266–2276. https://doi.org/10.1557/s43578-021-00173-x.

[85] J. Latalski, M. Kowalczuk, J. Warminski, Nonlinear electro-elastic dynamics of a hub–cantilever bimorph rotor structure, Int. J. Mech. Sci. 222 (2022) 107195. https://doi.org/10.1016/j.ijmecsci.2022.107195.

[86] D. Zhou, M. Kamlah, D. Munz, Effects of bias electric fields on the non-linear ferroelastic behavior of soft lead zirconate titanate piezoceramics, J. Am. Ceram. Soc. 88 (2005) 867–874. https://doi.org/10.1111/J.1551-2916.2005.00139.X.

[87] W. Kraus, G. Nolze, POWDER CELL - A program for the representation and manipulation of crystal structures and calculation of the resulting X-ray powder patterns, J. Appl. Crystallogr. 29 (1996) 301–303. https://doi.org/10.1107/S0021889895014920.

[88] H.-J. Bunge, View on ScienceDirect Texture Analysis in Materials Science 1st Edition, Butterworth-Heinemann. 1 (1982) 614.

[89] J.D. Hunter, Matplotlib: A 2D graphics environment, Comput. Sci. Eng. 9 (2007) 90–95. https://doi.org/10.1109/MCSE.2007.55.

[90] (14) (PDF) Guide to NumPy, (n.d.). https://www.researchgate.net/publication/213877900_Guide_to_NumPy (accessed October 7, 2022).

[91] P. Virtanen, R. Gommers, T.E. Oliphant, M. Haberland, T. Reddy, D. Cournapeau, E. Burovski, P. Peterson, W. Weckesser, J. Bright, S.J. van der Walt, M. Brett, J. Wilson, K.J. Millman, N. Mayorov, A.R.J. Nelson, E. Jones, R. Kern, E. Larson, C.J. Carey, İ. Polat, Y. Feng, E.W. Moore, J. VanderPlas, D. Laxalde, J. Perktold, R. Cimrman, I. Henriksen, E.A. Quintero, C.R. Harris, A.M. Archibald, A.H. Ribeiro, F. Pedregosa, P. van Mulbregt, A. Vijaykumar, A. Pietro Bardelli, A. Rothberg, A. Hilboll, A. Kloeckner, A. Scopatz, A. Lee, A. Rokem, C.N. Woods, C. Fulton, C. Masson, C. Häggström, C. Fitzgerald, D.A. Nicholson, D.R. Hagen, D. V. Pasechnik, E. Olivetti, E. Martin, E. Wieser, F. Silva, F. Lenders, F. Wilhelm, G. Young, G.A. Price, G.L. Ingold, G.E. Allen, G.R. Lee, H. Audren, I. Probst, J.P. Dietrich, J. Silterra, J.T. Webber, J. Slavič, J. Nothman, J. Buchner, J. Kulick, J.L. Schönberger, J.V. de Miranda Cardoso, J. Reimer, J. Harrington, J.L.C. Rodríguez, J. Nunez-Iglesias, J. Kuczynski, K. Tritz, M. Thoma, M. Newville, M. Kümmerer, M. Bolingbroke, M. Tartre, M.

Pak, N.J. Smith, N. Nowaczyk, N. Shebanov, O. Pavlyk, P.A. Brodtkorb, P. Lee, R.T. McGibbon, R. Feldbauer, S. Lewis, S. Tygier, S. Sievert, S. Vigna, S. Peterson, S. More, T. Pudlik, T. Oshima, T.J. Pingel, T.P. Robitaille, T. Spura, T.R. Jones, T. Cera, T. Leslie, T. Zito, T. Krauss, U. Upadhyay, Y.O. Halchenko, Y. Vázquez-Baeza, SciPy 1.0: fundamental algorithms for scientific computing in Python, Nat. Methods 2020 173. 17 (2020) 261–272. https://doi.org/10.1038/s41592-019-0686-2.

[92] J. Narvaez-Monroy, E. Villalobos-Portillo, L. Fuentes-Cobas, L. Fuentes-Montero, Polycrystal x-ray diffraction modelling: grazing incidence versus Bragg-Brentano, (2021) 12047. https://doi.org/10.1088/1742-6596/1723/1/012047.

[93] T. Atou, H. Chiba, K. Ohoyama, Y. Yamaguchi, Y. Syono, Structure determination of ferromagnetic perovskite $BiMnO_3$, J. Solid State Chem. 145 (1999) 639–642. https://doi.org/10.1006/jssc.1999.8267.

[94] H.J. Sokol, A.M. Ebrahim, S. Caratzoulas, A.I. Frenkel, J.A. Valla, In Situ XAFS, XRD, and DFT Characterization of the Sulfur Adsorption Sites on Cu and Ce Exchanged y Zeolites, J. Phys. Chem. C. 126 (2022) 1496–1512. https://doi.org/10.1021/acs.jpcc.1c09128.

[95] A. Khalid, M. Ali, G.M. Mustafa, S. Atiq, S.M. Ramay, A. Mahmood, S. Naseem, Structural and dielectric properties of sol–gel synthesized (Mn, Cu) co-doped BiFeO3 ceramics, J. Sol-Gel Sci. Technol. 80 (2016) 814–820. https://doi.org/10.1007/s10971-016-4142-9.

[96] A.S. Priya, D. Geetha, I.B. Shameem Banu, Structural, Dielectric, and Impedance Analysis of (Dy, Cu) Co-doped $BiFeO_3$, Brazilian J. Phys. 2021 515. 51 (2021) 1438–1447. https://doi.org/10.1007/S13538-021-00961-0.

[97] D.L. Hou, X.J. Ye, H.J. Meng, H.J. Zhou, X.L. Li, C.M. Zhen, G.D. Tang, Magnetic properties of n -type Cu-doped ZnO thin films, Appl. Phys. Lett. 90 (2007). https://doi.org/10.1063/1.2719034.

[98] M. Sahni, S. Mukhopadhyay, R.M. Mehra, S. Chauhan, P. Chandra Sati, M. Kumar, M. Singh, N. Kumar, Effect of Yb/Co co-dopants on surface chemical bonding states of $BiFeO_3$ nanoparticles with promising photocatalytic performance in dye degradation, J. Phys. Chem. Solids. 152 (2021) 109926. https://doi.org/10.1016/j.jpcs.2020.109926.

[99] P. Priyadharsini, A. Pradeep, B. Sathyamoorthy, G. Chandrasekaran, Enhanced multiferroic properties in la and Ce co-doped $BiFeO_3$ nanoparticles, J. Phys. Chem. Solids. 75 (2014) 797–802. https://doi.org/10.1016/j.jpcs.2014.03.001.

[100] S. Rani, S. Sanghi, A. Agarwal, R. Kumar, O. Singh, Crystal structure, magnetic and dielectric properties of Er-doped $BiFeO_3$ ceramics, Appl. Phys. A 2022 1287. 128 (2022) 1–17. https://doi.org/10.1007/S00339-022-05711-W.

[101] W.S. Mohamed, A. Nucara, G. Calestani, F. Mezzadri, E. Gilioli, F. Capitani, P. Postorino, P. Calvani, Optical study of the vibrational and dielectric properties of $BiMnO_3$, Phys. Rev. B - Condens. Matter Mater. Phys. 92 (2015). https://doi.org/10.1103/PhysRevB.92.054306.

[102] P. Toulemonde, C. Darie, C. Goujon, M. Legendre, T. Mendonca, M. Alvarez-Murga, V. Simonet, P. Bordet, P. Bouvier, J. Kreisel, M. Mezouar, Single crystal growth of $BiMnO_3$ under high pressure-high temperature, High Press. Res. 29 (2009) 600–604. https://doi.org/10.1080/08957950903467050.

[103] V. Goian, S. Kamba, M. Savinov, D. Nuzhnyy, F. Borodavka, P. Vaněk, A.A. Belik, Absence of ferroelectricity in $BiMnO_3$ ceramics, J. Appl. Phys. 112 (2012). https://doi.org/10.1063/1.4757944.

[104] L. Elcoro, B. Bradlyn, Z. Wang, M.G. Vergniory, J. Cano, C. Felser, B. Andrei Bernevig, D. Orobengoa, G. De La Flor, M.I. Aroyo, Double crystallographic groups and their representations on the Bilbao Crystallographic Server, J. Appl. Crystallogr. 50 (2017) 1457–1477. https://doi.org/10.1107/S1600576717011712.

[105] M.I. Aroyo, A. Kirov, C. Capillas, J.M. Perez-Mato, H. Wondratschek, Foundations of Crystallography Bilbao Crystallographic Server. II. Representations of crystallographic point groups and space groups, Acta Cryst. 62 (2006) 115–128. https://doi.org/10.1107/S0108767305040286.

[106] Y.-J. Kim, H.-S. Park, C.-H. Yang, Raman imaging of ferroelastically configureurable Jahn–Teller domains in $LaMnO_3$, Npj Quantum Mater. 6 (2021). https://doi.org/10.1038/s41535-021-00361-2.

[107] P. Toulemonde, P. Bordet, P. Bouvier, J. Kreisel, Single-crystalline $BiMnO_3$ studied by temperature-dependent x-ray diffraction and Raman spectroscopy, Phys. Rev. B - Condens. Matter Mater. Phys. 89 (2014). https://doi.org/10.1103/PHYSREVB.89.224107.

[108] R. Haumont, J. Kreisel, P. Bouvier, F. Hippert, Phonon anomalies and the ferroelectric phase transition in multiferroic $BiFeO_3$, Phys. Rev. B - Condens. Matter Mater. Phys. 73 (2006). https://doi.org/10.1103/PHYSREVB.73.132101.

[109] X.Y. Yu, Y. Wang, J.J. Peng, B.L. Wang, K.L. Wei, J.M. Liu, Q.Y. He, The enhanced thermoelectric properties of $BiMnO_3$ ceramics by Sr-doped, Mater. Res. Express. 5 (2018). https://doi.org/10.1088/2053-1591/aabb0b.

[110] M.G. Helander, M.T. Greiner, Z.B. Wang, Z.H. Lu, Note: Binding energy scale calibration of electron spectrometers for photoelectron spectroscopy using a single sample, Rev. Sci. Instrum. 82 (2011). https://doi.org/10.1063/1.3642659.

[111] V.S. Dharmadhikari, S.R. Sainkar, S. Badrinarayan, A. Goswami,

Characterisation of thin films of bismuth oxide by X-ray photoelectron spectroscopy, J. Electron Spectros. Relat. Phenomena. 25 (1982) 181–189. https://doi.org/10.1016/0368-2048(82)85016-0.

[112] M.W. Chu, M. Ganne, M.T. Caldes, L. Brohan, X-ray photoelectron spectroscopy and high resolution electron microscopy studies of Aurivillius compounds: $Bi_{4-x}La_xTi_3O_{12}$(x=0, 0.5, 0.75, 1.0, 1.5, and 2.0), J. Appl. Phys. 91 (2002) 3178–3187. https://doi.org/10.1063/1.1426251.

[113] K. Uchida, A. Ayame, Dynamic XPS measurements on bismuth molybdate surfaces, Surf. Sci. 357–358 (1996) 170–175. https://doi.org/10.1016/0039-6028(96)00083-0.

[114] L.Q. Wu, Y.C. Li, S.Q. Li, Z.Z. Li, G.D. Tang, W.H. Qi, L.C. Xue, X.S. Ge, L.L. Ding, Method for estimating ionicities of oxides using O1s photoelectron spectra, AIP Adv. 5 (2015). https://doi.org/10.1063/1.4931996.

[115] S.C. Roy, G.L. Sharma, M.C. Bhatnagar, Large blue shift in the optical band-gap of sol-gel derived $Ba_{0.5}Sr_{0.5}TiO_3$ thin films, Solid State Commun. 141 (2007) 243–247. https://doi.org/10.1016/j.ssc.2006.11.007.

[116] P.R. Jubu, F.K. Yam, V.M. Igba, K.P. Beh, Tauc-plot scale and extrapolation effect on bandgap estimation from UV–vis–NIR data – A case study of β-Ga_2O_3, J. Solid State Chem. 290 (2020). https://doi.org/10.1016/j.jssc.2020.121576.

[117] B. Revathi, L. Balakrishnan, S. Pichaimuthu, A. Nirmala Grace, N. Krishna Chandar, Photocatalytic degradation of rhodamine B using $BiMnO_3$ nanoparticles under UV and visible light irradiation, J. Mater. Sci. Mater. Electron. 31 (2020) 22487–22497. https://doi.org/10.1007/S10854-020-04750-4/FIGURES/8.

[118] V.S. Kavitha, R. Reshmi Krishnan, R. Sreeja Sreedharan, K. Suresh, C.K. Jayasankar, V.P. Mahadevan Pillai, Tb^{3+}-doped WO_3 thin films: A potential

candidate in white light emitting devices, J. Alloys Compd. 788 (2019) 429–445. https://doi.org/10.1016/j.jallcom.2019.02.222.

[119] A. Leonarska, M. Kądziołka-Gaweł, A.Z. Szeremeta, R. Bujakiewicz-Korońska, A. Kalvane, A. Molak, Electric relaxation and Mn^{3+}/Mn^{4+} charge transfer in Fe-doped Bi12MnO20–BiMn2O5 structural self-composite, J. Mater. Sci. 52 (2017) 2222–2231. https://doi.org/10.1007/s10853-016-0515-2.

[120] A. Sharan, I. An, C. Chen, R.W. Collins, J. Lettieri, Y. Jia, D.G. Schlom, V. Gopalan, Large optical nonlinearities in BiMnO 3 thin films, (2003). https://doi.org/10.1063/1.1632544.

[121] N. Bhardwaj, A. Gaur, K. Yadav, Optical and dielectric properties of $BiMn_{1-x}AE_xO_3$ (AE=Cr, Fe, Co, and Zn; X=0, 0.1) nanoparticles synthesized by sol-gel technique, AIP Conf. Proc. 1675 (2015) 1–5. https://doi.org/10.1063/1.4929286.

[122] B. Rafferty, L. Brown, Direct and indirect transitions in the region of the band gap using electron-energy-loss spectroscopy, Phys. Rev. B - Condens. Matter Mater. Phys. 58 (1998) 10326–10337. https://doi.org/10.1103/PhysRevB.58.10326.

[123] M.C. Cheynet, S. Pokrant, F.D. Tichelaar, J.L. Rouvìre, Crystal structure and band gap determination of Hf O2 thin films, J. Appl. Phys. 101 (2007) 054101. https://doi.org/10.1063/1.2697551.

[124] C.S. Granerød, S.R. Bilden, T. Aarholt, Y.F. Yao, C.C. Yang, D.C. Look, L. Vines, K.M. Johansen, Ø. Prytz, Direct observation of conduction band plasmons and the related Burstein-Moss shift in highly doped semiconductors: A STEM-EELS study of Ga-doped ZnO, Phys. Rev. B. 98 (2018) 115301. https://doi.org/10.1103/PhysRevB.98.115301.

[125] Y. Sun, F. Guo, J. Chen, S. Zhao, Improved ferroelectric and photovoltaic

properties of $BiMnO_3$ modified lead-free $K_{0.5}Na_{0.5}NbO_3$ solid-solution films, Appl. Phys. Lett. 111 (2017) 253901. https://doi.org/10.1063/1.5006643.

[126] F. Tian, Y. Ohki, Electric modulus powerful tool for analyzing dielectric behavior, IEEE Trans. Dielectr. Electr. Insul. 21 (2014) 929–931. https://doi.org/10.1109/TDEI.2014.6832233.

[127] K.J. Annand, I. Maclaren, M. Gass, Utilising DualEELS to probe the nanoscale mechanisms of the corrosion of Zircaloy-4 in 350°C pressurised water, J. Nucl. Mater. 465 (2015) 390–399. https://doi.org/10.1016/j.jnucmat.2015.06.022.

[128] M.A. Fakhri, Y. Al-Douri, U. Hashim, E.T. Salim, Optical investigations of photonics lithium niobate, Sol. Energy. 120 (2015) 381–388. https://doi.org/10.1016/j.solener.2015.07.044.

[129] D. Fritsch, Electronic and optical properties of sodium niobate: A density functional theory study, Adv. Mater. Sci. Eng. 2018 (2018). https://doi.org/10.1155/2018/6416057.

[130] G. Zumofen, N.M. Mojarad, V. Sandoghdar, M. Agio, Perfect reflection of light by an oscillating dipole, Phys. Rev. Lett. 101 (2008). https://doi.org/10.1103/PhysRevLett.101.180404.

[131] G. Herrera-Pérez, C. Ornelas-Gutiérrez, A. Reyes-Montero, F. Paraguay-Delgado, A. Reyes-Rojas, L. Fuentes- Cobas, Complex dielectric function and opto-electronic characterization using VEELS for the lead-free BCZT electro-ceramic perovskite, Micron. 149 (2021) 103124. https://doi.org/10.1016/j.micron.2021.103124.

[132] L. Pintilie, K. Boldyreva, M. Alexe, D. Hesse, Coexistence of ferroelectricity and antiferroelectricity in epitaxial PbZrO3 films with different orientations, J. Appl. Phys. 103 (2008). https://doi.org/10.1063/1.2831023.

[133] R. Ali Saha, A. Halder, D. Fu, M. Itoh, T. Saha-Dasgupta, S. Ray, The Critical Role of Stereochemically Active Lone Pair in Introducing High Temperature Ferroelectricity, Inorg. Chem. 60 (2021) 4068–4075. https://doi.org/10.1021/acs.inorgchem.1c00117.

[134] A. Moreira dos Santos, A.K. Cheetham, T. Atou, Y. Syono, Y. Yamaguchi, K. Ohoyama, H. Chiba, C.N.R. Rao, Orbital ordering as the determinant for ferromagnetism in biferroic $BiMnO_3$, Phys. Rev. B - Condens. Matter Mater. Phys. 66 (2002) 644251–644254. https://doi.org/10.1103/PhysRevB.66.064425.

[135] Z. Gong, W. Zhao, K. Guan, P. Rao, Q. Zeng, J. Liu, Z. Feng, Influence of grain boundary and grain size on the mechanical properties of polycrystalline ceramics: Grain-scale simulations, J. Am. Ceram. Soc. 103 (2020) 5900–5913. https://doi.org/10.1111/jace.17286.

[136] G. Campillo, J. Osorio, O. Arnache, A. Gil, J.J. Beltrán, L. Dorkis, Grain Size Reduction Effect on Structural and Magnetic Properties in $La_{1-x}Sr_xMnO_3$ (x = 0.3 y 0.4) by Mechanical Ball Milling, in: J. Phys. Conf. Ser., 2019. https://doi.org/10.1088/1742-6596/1247/1/012015.

[137] M. Naghizadeh, H. Mirzadeh, Effects of Grain Size on Mechanical Properties and Work-Hardening Behavior of AISI 304 Austenitic Stainless Steel, Steel Res. Int. 90 (2019). https://doi.org/10.1002/srin.201900153.

[138] G. Huo, Q. Su, H. Li, Z. Li, Y. Chang, Effect of oxygen non-stoichiometry on magnetic and electrical transport properties of $La_{0.67}Sr_{0.33}MnO_3$, Curr. Appl. Phys. 20 (2020) 739–745. https://doi.org/10.1016/J.CAP.2020.03.013.

[139] F. Zhuo, U.R. Eckstein, N.H. Khansur, C. Dietz, D. Urushihara, T. Asaka, K. ichi Kakimoto, K.G. Webber, X. Fang, J. Rödel, Temperature-induced changes of the electrical and mechanical properties of aerosol-deposited $BaTiO_3$ thick films for

energy storage applications, J. Am. Ceram. Soc. 105 (2022) 4108–4121. https://doi.org/10.1111/JACE.18377.

[140] T. Scholz, G.A. Schneider, J. Muñoz-Saldaña, M. V. Swain, Fracture toughness from submicron derived indentation cracks, Appl. Phys. Lett. 84 (2004) 3055. https://doi.org/10.1063/1.1711164.

[141] H. Zhang, F. De Luca, H. Wang, K. Mingard, M. Gee, Deformation mechanism of WC single crystals under nanoindentation: Effects of surface defects and orientation on pop-in and hysteresis, Int. J. Refract. Met. Hard Mater. 106 (2022) 105850. https://doi.org/10.1016/j.ijrmhm.2022.105850.

[142] K.L. Johnson, Contact Mechanics, (1989) 1–20. https://doi.org/10.1201/b17588-12.

[143] M. V. Swain, J.T. Hagan, Indentation plasticity and the ensuing fracture of glass, J. Phys. D. Appl. Phys. 9 (1976) 2201–2214. https://doi.org/10.1088/0022-3727/9/15/011.

[144] C. Domínguez-Ríos, A. Hurtado-Macias, R. Torres-Sánchez, M.A. Ramos, J. González-Hernández, Measurement of mechanical properties of an electroless Ni-B coating using nanoindentation, Ind. Eng. Chem. Res. 51 (2012) 7762–7768. https://doi.org/10.1021/IE201760G.

[145] H. Li, J. Chen, Determination of elastic moduli of elastic–plastic microspherical materials using nanoindentation simulation without mechanical polishing, Beilstein J. Nanotechnol. 1217. 12 (2021) 213–221. https://doi.org/10.3762/BJNANO.12.17.

[146] A.Z. Juri, A.K. Basak, L. Yin, In-situ SEM cyclic nanoindentation of pre-sintered and sintered zirconia materials, J. Mech. Behav. Biomed. Mater. 126 (2022) 105068. https://doi.org/10.1016/J.JMBBM.2021.105068.

[147] K.K. Jha, N. Suksawang, D. Lahiri, A. Agarwal, Evaluating initial unloading stiffness from elastic work-of-indentation measured in a nanoindentation experiment, J. Mater. Res. 28 (2013) 789–797. https://doi.org/10.1557/JMR.2013.3.

[148] A.B. Schäufele, K.H. Härdtl, Ferroelastic Properties of Lead Zirconate Titanate Ceramics, J. Am. Ceram. Soc. 79 (1996) 2637–2640. https://doi.org/10.1111/J.1151-2916.1996.TB09027.X.

[149] S.C. Hwang, C.S. Lynch, R.M. McMeeking, Ferroelectric/ferroelastic interactions and a polarization switching model, Acta Metall. Mater. 43 (1995) 2073–2084. https://doi.org/10.1016/0956-7151(94)00379-V.

[150] O. Le Bacq, A. Pasturel, R. Chattot, B. Previdello, J. Nelayah, T. Asset, L. Dubau, F. Maillard, Effect of Atomic Vacancies on the Structure and the Electrocatalytic Activity of Pt-rich/C Nanoparticles: A Combined Experimental and Density Functional Theory Study, ChemCatChem. 9 (2017) 2324–2338. https://doi.org/10.1002/CCTC.201601672.

[151] A. Seifitokaldani, O. Savadogo, M. Perrier, Density Functional Theory (DFT) Computation of the Oxygen Reduction Reaction (ORR) on Titanium Nitride (TiN) Surface, Electrochim. Acta. 141 (2014) 25–32. https://doi.org/10.1016/J.ELECTACTA.2014.07.027.

[152] K. Mathew, V.S.C. Kolluru, S. Mula, S.N. Steinmann, R.G. Hennig, Implicit self-consistent electrolyte model in plane-wave density-functional theory, J. Chem. Phys. 151 (2019) 234101. https://doi.org/10.1063/1.5132354.

[153] T. Björkman, CIF2Cell: Generating geometries for electronic structure programs, Comput. Phys. Commun. 182 (2011) 1183–1186. https://doi.org/10.1016/J.CPC.2011.01.013.

[154] P.E. Blöchl, Projector augmented-wave method, Phys. Rev. B. 50 (1994) 17953. https://doi.org/10.1103/PhysRevB.50.17953.

[155] M.G. Medvedev, I.S. Bushmarinov, J. Sun, J.P. Perdew, K.A. Lyssenko, Density functional theory is straying from the path toward the exact functional, Science (80-.). 355 (2017). https://doi.org/10.1126/SCIENCE.AAH5975/SUPPL_FILE/MEDVEDEV.SM.PDF.

[156] I. V. Solovyev, P.H. Dederichs, V.I. Anisimov, Corrected atomic limit in the local-density approximation and the electronic structure of *d* impurities in Rb, Phys. Rev. B. 50 (1994) 16861. https://doi.org/10.1103/PhysRevB.50.16861.

[157] C. Zhong, J. Fang, Q. Jiang, Magnetodielectric effects in the ferroelectric ferromagnetBiMnO3, J. Phys. Condens. Matter. 16 (2004) 9059. https://doi.org/10.1088/0953-8984/16/49/021.